

**A NOVEL MULTI-MODAL, WEARABLE SENSING SYSTEM TO
AUTOMATICALLY QUANTIFY CHANGES IN EXTRAVASCULAR
FLUID LEVELS**

A Dissertation
Presented to
The Academic Faculty

by

Samer Mabrouk

In Partial Fulfillment
of the Requirements for the Degree
Doctor of Philosophy
in
Electrical and Computer Engineering

Georgia Institute of Technology
December 2020

COPYRIGHT © 2020 BY SAMER MABROUK

A NOVEL MULTI-MODAL, WEARABLE SENSING SYSTEM TO AUTOMATICALLY QUANTIFY CHANGES IN EXTRAVASCULAR FLUID LEVELS

Approved by:

Dr. Omer Inan, Advisor
School of Electrical and Computer
Engineering
Georgia Institute of Technology

Dr. Jacob Abernathy
School of Computer Science
Georgia Institute of Technology

Dr. David Anderson
School of Electrical and Computer
Engineering
Georgia Institute of Technology

Dr. Mozziyar Etemadi
School of Bioomedical Engineering
Northwestern University

Dr. Pamela Bhatti
School of Electrical and Computer
Engineering
Georgia Institute of Technology

Date Approved: November 2nd, 2020

ACKNOWLEDGEMENTS

This wasn't easy, but the people who believed in and supported me made it easy! First, I want to start with thanking my inspirer and advisor, Prof. Omer Inan. This work would have not been possible without your guidance, support and supervision. I met professor Inan at my last semester at Georgia Tech as an undergraduate, few months before starting my fulltime job as a software developing engineer at Dell. I was impressed by his research vision and knew that one day I would want to be advised by him. Few months later, I reconnected with him and he shared me a project with high potential for commercialization, to which I was already sold. After one year at Dell, I joined professor Inan's research lab and for the next four years, he has been nothing but a true leader. He has given me immense support to pursue my research interests as well as motivating me in times when nothing seemed to go right. He has definitely led by example, showing great work ethic that I can only wish to attain. I want to thank him for being a friend, mentor and above all a great leader.

I would like to also thank Prof. Pamela Bhatti, Prof. David Anderson, Prof. Mozziyar Etemadi and Prof. Jacob Abernathy for taking time to serve on my committee and provide insightful comments and suggestions regarding my work. I would like to also thank Dr. Kevin Maher who has been an absolute pleasure to work for the past few years as a clinical partner on researching technologies for automating IV infiltration detection.

I am incredibly fortunate to have worked with smart, driven and cooperative teammates during my studies, including: Oludotun Ode, Md Mobashir Hasan Shandi, Beren Semiz, Hyeon Ki Jeong, Hewon Jung, Venu Ganti, Jacob Kimball, Brandi Nevius,

Asim Gazi, Adith Srivatsa, Arjun Sonti, Andrew Carek, Nil Gurel, Caitlin Teague and Nick Bolus. Especially, Dr. Sinan Hersek who welcomed me to the lab and has been a great teammate from the first day helping me with my research. Also, Dr. Daniel Whittingslow whose clinical input on my research has helped taking it to the next level. Arjun Sonti and Adith Srivatsa have been super-star undergraduate researchers who have assisted me a lot in research.

I want to also express my deepest gratitude to my mom, Eman Elbahnasy. Growing up she sacrificed her personal and financial well-being to give me the best education possible. Raising me up on her own, she has always supported me and pushed me to pursue higher education. Also, my little siblings: Sarah, Abdelkarim and Abdelrahma Raafat; thank you for all your support and love.

Last but not least, I want to thank my wife, Ayah Mostafa for her continuous support throughout my PhD. Our marriage was commenced the day after taking my PhD qualification exam and since then she has become my support for the better part of my PhD. Thank you for listening to me talk about bioimpedance every other day while not understanding what it means but still nodding your head. Your OCD has definitely helped moving my presentations and papers to the next level.

TABLE OF CONTENTS

ACKNOWLEDGEMENTS	vi
LIST OF TABLES	xi
LIST OF FIGURES	xii
SUMMARY	xvii
CHAPTER 1. Introduction	1
1.1 Motivation	1
1.2 Electrical Bioimpedance Analysis	2
1.2.1 Fundamentals of Bioimpedance Analysis	2
1.2.2 Tissue Impedance Circuit Model	3
1.3 Major Contributions of this Work	5
1.4 Dissertation Organization	6
CHAPTER 2. Miniaturized Bioimpedance Acquisition System Design	8
2.1 Instrumentation and Methods to Measure Bioimpedance	8
2.2 System Level Design	10
2.2.1 Bioimpedance Circuitry	11
2.3 Bioimpedance Acquisition System Design Utilizing the AD5933	13
2.3.1 Custom Designed External AFE for the AD5933	15
2.4 Bioimpedance Acquisition System Design Using the AD5940	16
2.4.1 AD5940 Theory of Operation	17
2.4.2 Custom Designed External AFE for the AD5940	18
2.4.3 AD5940 System Calibration	19
2.5 Firmware and Software Architecture	19
2.6 Novel Physiology Driven Calibration Technique	20
2.6.1 Linear Regression Bases Multi-Point Calibration	21
2.6.2 Optimizing the Impedances Used for Calibration	23
2.7 Bioimpedance Acquisition System Characterization	24
2.7.1 AD5933 Based System Characterization	24
2.7.2 AD5940 Based System Characterization	27
2.7.3 AD5940 vs AD5933 Based Design	28
2.8 Conclusion	29
CHAPTER 3. System Validation in the Context of Robust Tracking of Edema Volume in the Ankle Joint	30
3.1 Introduction	30
3.2 Edema Quantification Methods	33
3.2.1 Edema Quantification Protocol	36
3.3 Edema Quantification Protocol Results	37
3.3.1 Intra-subject Variability	38
3.3.2 Inter-Subject Variability	39

3.4	Cadaver Study	40
3.4.1	Cadaver Study Results	41
3.5	Conclusion	43
 CHAPTER 4. Translation of Edema Quantification Methods to a Wearable Setting		
4.1	Introduction	44
4.2	Signal Analysis	45
4.2.1	The Reactance of the Tissue	46
4.3	Simulation Model	47
4.3.1	Fricke-Morse Model Estimation	48
4.3.2	The Ratio of $X5\text{ kHz}$ to $X100\text{ kHz}$	50
4.3.3	Simulation Model Results	51
4.4	Blood Flow vs Edema vs Muscle Tear	52
4.5	Algorithm	53
4.6	Data Collection Protocol for Method's Evaluation	56
4.7	Statistical Analysis	58
4.8	Results	59
4.8.1	Ratio of the Ranges of Reactance Per Step ($h\alpha$)	59
4.8.2	Beta Walking Results	61
4.8.3	Zero Crossings Data Analysis	62
4.9	Conclusion	63
 CHAPTER 5. Methods and Algorithms for IV Infiltration Detection		
5.1	Introduction	65
5.2	Porcine Model Study	67
5.2.1	Protocol	67
5.2.2	Results	68
5.3	Human Subject Study at Children's Healthcare of Atlanta	71
5.3.1	Study Protocol	71
5.3.2	Baseline reset algorithm	72
5.3.3	Results	73
5.4	Conclusion	75
 CHAPTER 6. Dynamic Surface Electrical Impedance Tomography for Uniform Static Fluid Quantification		
6.1	Introduction	76
6.2	Hardware Design	78
6.2.1	EIT System Calibration	80
6.3	Electrical Impedance Tomography Reconstruction Algorithm	80
6.4	Experimental Design and Results	85
6.4.1	Phantom Model Experiments and Results	85
6.4.2	Animal Tissue Experiment and Results	88
6.5	Implication on IV Infiltration Detection	92
6.6	Conclusion	92
 CHAPTER 7. Conclusion and Future work		
		94

7.1	Conclusion	94
7.2	Future Work	96
7.2.1	Hardware Directions	96
7.2.2	Clinical Directions	97

LIST OF TABLES

TABLE 1. COMPARISON BETWEEN DIFFERENT INTEGRATED CIRCUITS CAPABLE OF PERFORMING BIA.	12
TABLE 2. AD5933 SYSTEM PROPERTIES.....	25
TABLE 3. AD5933-BASED DESIGNS COMPARISON WITH SIMILAR DESIGNS FROM THE LITERATURE THAT UTILIZE DIFFERENT CALIBRATION TECHNIQUES AND AFE DESIGNS.	26
TABLE 4. AD5940 SYSTEM PROPERTIES.....	27
TABLE 5. ESTIMATED FRICKE-MORSE CIRCUIT COMPONENT VALUES OF 14 ANKLES WITH NO RECENT RECORD OF INJURY.	49

LIST OF FIGURES

FIGURE 1. BIOIMPEDANCE ACQUISITION SYSTEM INTERFACE. (LEFT) THE LESS COMPLEX 2-ELECTRODE CONFIGURATION MEASURES THE COMBINED IMPEDANCE OF THE TISSUE AND THE SKIN-ELECTRODE INTERFACE. (RIGHT) 4-ELECTRODE CONFIGURATION ISOLATES THE TISSUE IMPEDANCE MAKING IT MORE ACCURATE BUT ALSO MORE COMPLEX THAN THE 2-ELECTRODE CONFIGURATION.	9
FIGURE 2. BIOIMPEDANCE ACQUISITION SYSTEM. (LEFT) THE FINAL MINIATURIZED SYSTEM PRESENTED IN THIS WORK CONSISTS OF A CUSTOM 3D PRINTED BOX THAT HOUSES THE CUSTOM BUILT 4-LAYER PCB, WITH A 12-PIN AMPLIFIER CONNECTOR THAT INTERFACES TO THE ELECTRODE SNAPS, (RIGHT) TEMPERATURE AND INERTIAL MEASUREMENT SENSORS PLACED ON THE TISSUE OF INTEREST.	10
FIGURE 3. BLOCK DIAGRAM OF THE BIOIMPEDANCE ACQUISITION SYSTEM UTILIZING THE AD5933 IMPEDANCE ANALYZER TO MEASURE THE TISSUE’S BIOIMPEDANCE. (RIGHT) AD5933 BIA SYSTEM BLOCK DIAGRAM.....	13
FIGURE 4. MINIATURIZED DESIGN FOR THE AD5933 AFE TO ENABLE 4-ELECTRODE BIOIMPEDANCE MEASUREMENTS. THE AFE CONSISTS OF A VOLTAGE CONTROLLED CURRENT SOURCE THAT PROVIDES THE CONSTANT CURRENT TO EXCITE THE TISSUE, TWO HIGH PASS FILTERS TO REMOVE AMBIENT NOISES AND AN INSTRUMENTATION AMPLIFIER TO MEASURE THE VOLTAGE DIFFERENCE DUE TO THE EXCITATION CURRENT.....	16
FIGURE 5. BLOCK DIAGRAM OF BIOIMPEDANCE ACQUISITION SYSTEM UTILIZING AD5940. THE IC USES A NOVEL APPROACH TO MEASURE BIOIMPEDANCE THAT ALLOWS HAVING AN INFINITE DYNAMIC RANGE AND HIGH SKIN-ELECTRODE INTERFACE IMPEDANCE BUT REQUIRES TAKING TWO MEASUREMENTS: THE CURRENT FLOWING THROUGH THE TISSUE AND THE VOLTAGE DUE TO THIS CURRENT.....	17
FIGURE 6. NOVEL PHYSIOLOGY DRIVE CALIBRATION TECHNIQUE USED TO REDUCE MEASUREMENT ERROR BY UTILIZING LEAST SQUARES ¹ ERROR REDUCTION ABILITIES. THE 2R1C SPACE OF R_e , R_i AND C IS UTILIZED TO OPTIMIZE THE CALIBRATION IMPEDANCES. SPECIFICALLY, EIGHT 2R1C IMPEDANCES THAT SPAN THE 3D SPACE UP TO THE SYSTEM’S DYNAMIC RANGE, ENCOMPASSING THE IMPEDANCE OF VARIOUS BODY PARTS ARE USED TO CALIBRATE THE SYSTEM USING LINEAR REGRESSION.....	21

FIGURE 7. THE FIVE DIFFERENT POSTURE USED IN THE EXPERIMENT. (b) AND (c) SHOW THE CHANGE IN IMPEDANCE NORMALIZED TO THE RESTING POSITION ALONG WITH A SMALL SKETCH SHOWING THE EDEMA MOVING THROUGH THE DIFFERENT CURRENT BANDS FOR (b) A HEALTHY CONTROL SUBJECT AND (c) AN INJURED SUBJECT.....	35
FIGURE 8. A SCATTER PLOT SHOWS THE INTRA-SUBJECT VARIABILITY OF THE TWO METHODS DISCUSSED IN THIS PAPER FOR ALL CONTROL SUBJECTS OVER THE LENGTH OF THE STUDY. NOTE THAT Ej FOR THE RIGHT IS THE NEGATIVE OF Ej FOR THE LEFT.....	38
FIGURE 9. BOX PLOT SHOWS THE INTER-SUBJECT VARIABILITY AND THE SEPARATION FOR THE TWO METHODS DISCUSSED OVER THE LENGTH OF THE STUDY.	40
FIGURE 10. CADAVER LEG WITH BIOIMPEDANCE ACQUISITION SYSTEM ELECTRODES PLACED DISTALLY AND PROXIMALLY TO THE ANKLE JOINT, AND SALINE BEING INJECTED TO THE JOINT.	41
FIGURE 11. CADAVER MODEL STUDY RESULTS SHOWING A REDUCTION IN THE RATIO OF THE CHANGE IN HIGH FREQUENCY RESISTANCE TO LOW FREQUENCY RESISTANCE DUE TO THE ANKLE ROTATION WITH INCREASING THE JOINT'S STATIC FLUID CONTENT.	42
FIGURE 12. THE ANATOMY OF THE ANKLE JOINT SHOWING LACK OF FATTY TISSUE OR STATIC FLUID. (b) A SAMPLE BLOOD VESSEL AND MUSCLE FIBER WHICH ARE THE PRIMARY PATH FOR THE CURRENT APPLIED TO MEASURE THE BIOIMPEDANCE. (c) A MUSCLE FIBER TEAR, SHOWING THE MIGRATION OF INTRACELLULAR FLUIDS TO THE EXTRACELLULAR SPACE SURROUNDING. (d) AN INCREASE IN THE RED BLOOD CELL COUNT AND GLUCOSE DUE TO SUSTAINED MUSCLE ACTIVITY. (e) AN INCREASE IN EDEMA DUE TO MUSCLE INFLAMMATION.	47
FIGURE 13. AN EXAMPLE OF LOCALIZED BIOIMPEDANCE SPECTROSCOPY DATA AND ITS ASSOCIATED FRICK-MORSE ESTIMATED PARAMETERS WHEN USING NON-LINEAR LEAST SQUARES ESTIMATION TO FIND THE OPTIMAL $2R1C$ VALUES THAT FIT THE MEASURED DATA.	49
FIGURE 14. SIMULATION MODEL RESULTS FOR THE EFFECT OF CHANGES IN BLOOD FLOW, EDEMA, COLLAGE FIBER TEAR AND COLLAGE FIBER TEAR ACCOMPANIED WITH EDEMA ON THE RATIO OF THE CHANGE IN LOW FREQUENCY REACTANCE TO HIGH FREQUENCY REACTANCE.....	51
FIGURE 15. DATA ANALYSIS WORKFLOW FOR DETERMINING PRESENCE OF EDEMA AND DISRUPTION TO STRUCTURAL INTEGRITY OF THE ANKLE. (a) THE DATA ACQUISITION SYSTEM PLACED ON THE SUBJECT'S LEG WITH THE NECESSARY CURRENT AND VOLTAGE ELECTRODES PLACED DISTALLY AND PROXIMALLY TO THE ANKLE JOINT AND THE IMU PLACED ON THE FOOT. (b)	

SAMPLE DATA OF A REPRESENTATIVE INJURED SUBJECT’S X-AXIS ANGULAR VELOCITY, Z-AXIS ACCELERATION, AND REACTANCE MEASURED AT 5 KHz AND 100 KHz. (c) A MAGNIFIED VIEW OF THE SAMPLE DATA SHOWING HOW THE DATA WINDOWS ARE CREATED AND USED IN SPLITTING TO SPLIT THE REACTANCE DATA INTO VECTORS PER STEP. (d) THE REACTANCE VECTORS PER STEP ARE USED IN THE MODEL TO DETECT EDEMA AND COLLAGEN FIBER TEAR IN THE ANKLE JOINT.	55
FIGURE 16 . RECORDING SETUP AND 8-HOUR RECORDING PROTOCOL TIMELINE. (A) THE WEARABLE DATA ACQUISITION IS PLACED ON THE SUBJECT’S LEG. (B) THE OVERALL RECORDING PROTOCOL TOOK 8 HOURS WITH THE 5-MINUTE POSITIONAL PROTOCOL AS DEPICTED IN (c) BEING PERFORMED EVERY HOUR.....	57
FIGURE 17. METHOD FOR COMPARING THE FULL WALKING SESSION TO 5-MINUTE PROTOCOL. (A) THE RANGE OF CHANGE IN THE REACTANCE MEASURED AT 5 KHz AND 100 KHz DURING A CONTINUOUS WALKING SESSION IS USED TO CALCULATE B. (B) THE RANGE OF THE CHANGE IN THE REACTANCE MEASURED AT 5 KHz AND 100 KHz PER STEP IS USED TO CALCULATE ha . (C) THE MEAN ha OF THE LAST 10 STEPS IS CORRELATED TO THE RATIO OF THE RANGE OF CHANGE IN THE REACTANCE MEASURED AT 5 KHz AND 100 KHz USING PEARSON’S CORRELATION.	58
FIGURE 18. (A) PLOT SHOWING ha VS STEPS FOR ALL SUBJECTS AND (B) A SCATTER PLOT OF THE MEAN OF ha FOR THE LAST TEN STEPS FOR THE HEALTHY AND INJURED GROUPS SHOWING A STATISTICALLY SIGNIFICANT P-VALUE. (C) PLOT OF THE MEAN ha AT THE LAST TEN STEPS IN A CONTINUOUS WALKING SESSION, CORRELATED THE OUTPUT OF THE 5-MINUTE PROTOCOL DONE AFTER WITH A PEARSON CORRELATION COEFFICIENT OF 0.8.	60
FIGURE 19. (A)PLOT SHOWING B VS STEPS FOR ALL SUBJECTS AND (B) A SCATTER PLOT OF THE B AT THE LAST STEP OF A CONTINUOUS WALKING SESSION SHOWING A STATISTICALLY SIGNIFICANT P-VALUE.	61
FIGURE 20. IV CATHETER PLACED SUBCUTANEOUSLY WITH THE CURRENT AND VOLTAGE ELECTRODES PLACED PROXIMALLY AND DISTALLY TO THE IV SITE.	68
FIGURE 21. LOCALIZED BIOIMPEDANCE MEASUREMENT OF THE IV SITE DURING (TOP) NORMAL DRUG DELIVERY TO THE BLOOD STREAM AND (BOTTOM) TO THE SURROUNDING TISSUE SIMULATING AN INFILTRATION.	69
FIGURE 22. LOCALIZED BIOIMPEDANCE MEASUREMENT AT 5 AND 100 KHz OF AN IV SITE WHILE INFUSING 2, 7, 17, AND 27 ML OF FLUID.	70
FIGURE 23. BLOCK DIAGRAM OF SIGNAL PROCESSING APPROACH TO REMOVING POSTURAL SHIFT RELATED ARTIFACTS FROM IMPEDANCE MEASUREMENTS THAT WILL ULTIMATELY PROVIDE DETECTION OF IV INFILTRATION	72

FIGURE 24. Z-AXIS ACCELERATION DATA FROM THE IV SITE OF A SUBJECT RECEIVING IV TREATMENT AND (b) THE RESPECTIVE RAW 50 KHz RESISTANCE MEASURED (BLUE) SHOWING CORRELATION BETWEEN BOTH SIGNALS, AND THE CORRECTED SIGNAL IN GREEN. (c) THE COMPILED MEAN AND STANDARD DEVIATION OF THE RAW 50 KHz RESISTANCE FROM ALL SUBJECTS SHOWN IN BLUE AND THE CORRECTED SIGNAL IN GREEN SHOWING A REDUCTION IN THE VARIATION IN THE SIGNAL OVER TIME.	73
FIGURE 25. SURFACE ELECTRICAL IMPEDANCE TOMOGRAPHY TO GENERATE THE CONDUCTIVITY MAP OF THE IV SITE SHOWING THE LOCATION OF IMPEDANCE CHANGES WHICH CAN BE UTILIZED TO ALERT THE MEDICAL STAFF IF THE LOCATION CORRELATES WITH THE IV CATHETER LOCATION.....	76
FIGURE 26. ELECTRICAL IMPEDANCE TOMOGRAPHY SYSTEM (LEFT) BLOCK DIAGRAM UTILIZING THE AD5940 ELECTRO-CHEMICAL AFE TO MEASURE THE SEGMENTAL BIOIMPEDANCE AND FOUR ADG729 ANALOG MULTIPLEXERS TO SPECIFY THE EXCITATION AND MEASUREMENT ELECTRODES.	79
FIGURE 27. DYNAMIC ELECTRICAL IMPEDANCE TOMOGRAPHY RECONSTRUCTION ALGORITHM. NEIGHBORING METHOD IS USED, WHERE TWO ADJACENT ELECTRODES ARE USED TO EXCITE THE TISSUE, AND THE VOLTAGE IS MEASURED BETWEEN THE REMAINING ADJACENT VOLTAGE ELECTRODES FOR A TOTAL OF 40 MEASUREMENTS FOR AN EIGHT-ELECTRODE SYSTEM. FOR EACH MEASUREMENT, A MASK IS CREATED FOR ITS RESPECTIVE EQUIPOTENTIAL PROJECTION. ALL 40 MASKS ARE USED TO CREATE THE PROJECTION MATRIX WHICH CAN BE THEN USED BY SIMPLY MULTIPLYING IT WITH THE NORMALIZED IMPEDANCE MEASUREMENTS VECTOR, REDUCING THE COMPUTATIONAL POWER NEEDED FOR RECONSTRUCTION TO A SINGLE MATRIX MULTIPLICATION. THE RESULT OF THE MULTIPLICATION IS THE RECONSTRUCTED IMAGE SHOWING A SCAN OF THE UNDERLYING TISSUE IMPEDANCE DISTRIBUTION.....	83
FIGURE 28. PHANTOM MODEL EXPERIMENT RESULTS. (a) THE EIGHT MEASUREMENT ELECTRODES ARE PLACED AROUND A HOLLOW CYLINDER FILLED WITH SALTWATER. A NON-CONDUCTIVE PLASTIC CIRCULAR OBJECT IS MOVED DIAGONALLY TO INDUCE CHANGES IN THE PATH OF THE IMPEDANCE MEASUREMENTS CLOSE TO IT. RESULTS FROM USING (b) SINGLE LINE, (c) TRIANGLE AND (d) AREA BETWEEN CONTOUR LINES AS PROJECTIONS WERE USED FOR COMPARISON. USING CONTOUR LINES PROVIDED THE BEST RESULTS ESPECIALLY WHEN THE OBJECT IS PLACED CLOSE TO THE CENTER. THIS IS DUE TO ITS SIMILARITY TO THE ACTUAL EQUIPOTENTIAL PATHS.....	87

FIGURE 29. ANIMAL TISSUE EXPERIMENT. EIGHT ELECTRODES WERE PLACED ON A CHICKEN BREAST IN A CIRCULAR FASHION
SIMILAR TO OUR ELECTRODE PACKAGE. THE IMPEDANCE MEASUREMENT Z_{ACROSS} IS SHOWN USING THE DOTTED LINE.

FIGURE 30 PRESENT THE EXPERIMENTS AND RESULTS. 88

FIGURE 30. ANIMAL TISSUE EXPERIMENTS AND RESULTS. (A) THE EFFECT OF INCREASE IN THE INTERNAL TEMPERATURE OF THE
CHICKEN BREAST ON THE IMPEDANCE ACROSS THE TISSUE AND THE RECONSTRUCTED IMAGE. (B) THE EFFECT OF INJECTING
1.5 ML OF SALINE AT DIFFERENT SIDES OF THE CHICKEN BREAST ON THE IMPEDANCE MEASURED ACROSS THE TISSUE AND
THE RECONSTRUCTED. NOTE THE SUBSTANTIAL DIFFERENCE IN THE DROP OF THE IMPEDANCE MEASURED ACROSS WHEN
THE SALINE IS INJECTED CLOSE TO THE ELECTRODES (I AND III) VERSUS WHEN FURTHER FROM IT (II, IV AND V) SHOWING
THE EFFECT OF ELECTRODE PLACEMENT ON SENSITIVITY TO CHANGES STATIC FLUID VOLUME. 91

SUMMARY

The buildup of static edematous fluids (swelling) in the tissue is indicative of a serious medical condition that can lead to long-term tissue damage, reduction in mobility and in some cases loss of limb. This swelling can be due to internal factors such as an immunoresponse to injuries or infections, or external factors such as a leakage of infused intravenous medication to the surrounding tissue (i.e., IV infiltration or extravasation). Detecting and tracking changes in a tissue's extracellular fluid content is crucial in diagnosing the severity of the injury and/or infection, and thereby preventing irreversible tissue damage. However, current methods for quantifying fluid levels in the extravascular space are either (1) manual and subjective, relying heavily on the medical staff's expertise, or (2) costly and timely, such as X-rays or magnetic resonance imaging (MRI).

In this dissertation, I present non-invasive wearable technologies that utilize localized bioimpedance contextualized by the tissue's kinematics to robustly quantify changes in the biological tissue's extracellular fluid content. Towards this goal, several robust and miniaturized systems are designed and implemented by researching different integrated circuits, analog front ends, and novel physiology-driven calibration techniques that together increase the system's accuracy and reduce its size and power consumption. Next, novel methods and algorithms are developed to allow for unobtrusive real-time detection of changes in extracellular fluid content. The systems, methods and algorithms were validated in human subjects studies, animal models and cadaver models for ankle edema tracking, and in human subjects studies and animal tissue for intravenous infiltration detection.

CHAPTER 1. INTRODUCTION

1.1 Motivation

Tissue swelling or edema is caused by the buildup of excess static extracellular fluid in the tissue and commonly results from injury or inflammation. Tracking tissue swelling, especially in the lower limbs, is essential for the evaluation and detection of various disorders such as congestive heart failure, cirrhosis, kidney diseases, and arthritis [1, 2]. It is also beneficial for assessing the rehabilitation process of recently injured joints and muscles, enabling physicians to make informed decisions about the course of treatment required and the readiness for activity [3].

Tissue swelling and edema are common phenomena that, if accurately tracked and interpreted, could be used as a *digital* biomarker which is an objective and quantifiable physiological metric measured using a digital device, and used to explain and predict health related outcomes [4, 5]. In the recent literature, localized bioimpedance analysis (BIA) has been investigated as a possible modality to quantify tissue edema, due to its sensitivity to changes in the tissue fluid content [6]. This was facilitated by the recent advances in analog circuit technologies simplifying the measurement hardware development. Historically, BIA has been primarily used for static impedance based measures of body composition (e.g., body fat percentage), and for dynamic impedance based measures of blood and / or air flow (impedance cardiography (ICG), impedance plethysmography, and impedance pneumography) [6-8]. Both approaches are generally performed in a controlled setting with minimal movement of the body to ensure signal integrity due to the size of bioimpedance acquisition systems, and BIA's sensitivity to movement and positional changes.

1.2 Electrical Bioimpedance Analysis

BIA is a noninvasive approach used in research and clinical practice for body composition analysis and disease prognosis [9-16]. The impedance of a body tissue is affected by changes in the intra-cellular and extra-cellular fluidic volume as well as the cell membrane width. The numerous ways and methods to perform BIA enabled its usage in different applications such as body composition, muscle and joint injury tracking, cardiac output tracking, breast cancer detection, and many more [17-22]. The first use of BIA dates back to 1871 by Thomasset [23] as a means to evaluate the total body water volume, a critical parameter in body composition analysis. However, BIA has been limited to clinical and lab settings due to the complexity of the hardware and power consumption, until recently due to advancements in analog circuitry and electrode technology that allowed having commercially available BIA devices outside the lab / clinic. Localized BIA has gained a lot of attention recently due to its ability in tracking and evaluating musculoskeletal injuries [24-26]. Research done by Hersek, et al. showed the ability of bioimpedance in tracking knee injuries longitudinally in non-clinical setting [25].

1.2.1 Fundamentals of Bioimpedance Analysis

Bioimpedance is the measure of the tissue's ability to impede electricity [12]. It is measured by injecting an alternating current at frequency f through the tissue while measuring the potential difference across it. Using Ohm's law, the magnitude and the phase of the impedance is measured as follows: Let I be the current injected into the tissue at frequency f and phase ϕ_I where $I = |I|e^{(2\pi ft + \phi_I)}$. Let V be the potential difference caused

by the current injected into the tissue at frequency f and phase ϕ_V where $V = |V|e^{(2\pi ft + \phi_V)}$. The bioimpedance of the tissue will then be:

$$Z = \frac{V}{I} = \frac{|V|}{|I|} e^{\phi_V - \phi_I} \quad (1)$$

The bioimpedance consists of a real (i.e. resistance) and an imaginary (i.e. reactance) component that can be calculated using:

$$\text{Resistance, } R = Z \cos(\phi_V - \phi_I) \quad (2)$$

and

$$\text{Reactance, } X = jZ \sin(\phi_V - \phi_I) \quad (3)$$

where

$$Z = R + jX \quad (4)$$

The real component (R) of the impedance is influenced by the total body water of the measured tissue and the imaginary component (X) (i.e. reactance) is associated with the cell density due to capacitance of the cell membrane [12-15].

1.2.2 Tissue Impedance Circuit Model

In the literature there are many circuit models to simulate the impedance of the tissue [27]. In this dissertation, I will be using the Fricke-Morse (2R1C) bioimpedance circuit model due to its simplicity and accuracy [28]. The model consists of a resistor (R_e) resembling the tissue's extracellular resistance in parallel to a capacitor (C_x) and resistor

(R_i) in series. The two in series components R_i and C_x resemble the cell membrane capacitance and intracellular resistance of the cells in the path of the current.

1.2.2.1 Single Frequency Bioimpedance Analysis

Single frequency BIA (SFBIA) is the measure of bioimpedance at 50 kHz electrical current [9, 11, 12, 14, 15, 29, 30]. It is the commonly used variant of BIA in literature for body composition analysis and ICG. For body composition analysis, static bioimpedance measurements at 50 kHz are used to obtain the relationship between the impedance of the body and the total body weight to estimate the body's muscle and fat content percentages. In contrast, ICG examines the dynamic changes in bioimpedance (changes over milliseconds) of the thorax from which numerous cardio-dynamic parameters can be processed [6]. ICG is a simple way to measure stroke volume as the instantaneous changes in the thorax's impedance can be directly related to the volumetric changes in the liquid passing through.

1.2.2.2 Multifrequency Bioimpedance Analysis

Multifrequency BIA (MFBIA) is the measure of bioimpedance at two or more different frequencies [9, 11-15, 29]. Currents injected at different frequencies into the body have different cell penetration abilities [31]. Skin effect theory states that high frequency currents have the ability to penetrate cell membranes, hence providing more information about intracellular fluids [27]. Low frequency currents, on the other hand, cannot penetrate cell membranes; they take a longer path through the extracellular fluids (i.e. interstitial fluids and blood), providing more information about the extracellular fluid density in the tissue. Much research has been done to identify the frequency range for low frequency

bioimpedance measurements and high frequency bioimpedance measurements. In general, low frequency bioimpedance measurements are performed at frequencies lower than 20 kHz and high frequency bioimpedance measurements at frequencies higher than 50 kHz [32]. MFBIA has been argued to be a better way to evaluate body composition due to its ability in measuring both intracellular fluids (ICF) and extracellular fluids (ECF).

1.2.2.3 Bioimpedance Spectroscopy

Bioimpedance spectroscopy (BIS) is the measure of bioimpedance over a wide spectrum of frequencies, usually between 1 kHz and 100 kHz [33]. The impedance measured at those frequencies is used to estimate the Fricke-Morse circuit components from which a more sophisticated model can be used to quantify the ECF and ICF of a biological tissue more accurately. The Fricke-Morse circuit parameter estimation procedure requires bioimpedance measurements at multiple frequencies to perform the complex non-linear least squares operation to estimate the extracellular resistance, intracellular resistance and capacitance. Traditionally, BIS has been performed using benchtop equipment capable of measuring bioimpedance at multiple frequencies and computing the Fricke-Morse parameters. It has also been limited to applications that use static changes in the impedance such as body composition analysis as measuring multiple frequencies requires longer times, therefore reducing the overall sampling rate of the system making it undesirable for applications dependent on dynamic changes such as ICG.

1.3 Major Contributions of this Work

In this dissertation, various methods are researched and developed to overcome some of the limitations of using bioimpedance in uncontrolled settings. Specifically, the major contributions of this work to the scientific community can be summarized as follows:

- 1) Designed, optimized, and validated a wearable system and associated calibration techniques for enabling robust multi-frequency bioimpedance measurement in the context of movement.
- 2) Demonstrated the ability to quantify edema with greater accuracy than state-of-the-art approaches with a novel movement and posture contextualized multi-frequency bioimpedance measurement technique.
- 3) Designed, implemented, and verified a simple and accurate electrical impedance tomography reconstruction algorithm requiring minimal computation to generate the conductivity distribution of biological tissue towards automatic detection of intravenous infiltration.

1.4 Dissertation Organization

The rest of this dissertation is organized as follows: First, miniaturized bioimpedance acquisition systems are developed to overcome the challenge of using bulky measurement equipment facilitating data collection in a wearable setting. Specifically, Chapter 2 starts with a brief summary of bioimpedance acquisition system topologies, and two custom built miniaturized bioimpedance acquisition systems are presented. Then, the calibration and validation of both systems by novel physiology driven techniques is discussed, and the resultant accuracy and resolution are provided. Then, using the systems presented in Chapter 2, novel methods are devised to quantify ECF content in (1) tissues with repetitive

cyclical movement such as the ankle joint and (2) tissues with random unpredictable postural shifts. In Chapter 3, the effect of joint rotation on low and high frequency bioimpedance with varying static fluid content is studied in human subjects and cadaver models. Using this knowledge, a novel and simple algorithm is developed to quantify joint edema by comparing the changes in low and high frequency measurements due to the joint rotation. In Chapter 4, with the knowledge attained from Chapter 3, the ankle joint's bioimpedance and kinematics are paired to quantify the joint edema and structural integrity during ambulation in an uncontrolled setting. Next, in Chapter 5, bioimpedance data of the tissue is again paired with the tissue kinematics, but to reduce the effect of postural shift on the tissue's longitudinal change in bioimpedance in the context of intravenous infiltration detection. In Chapter 6, to overcome traditional bioimpedance's non uniform static fluid detection resolution, a wearable system capable of scanning the tissue's conductivity distribution is presented. Finally, Chapter 7 discusses conclusions and impact, and provides directions for future work.

CHAPTER 2. MINIATURIZED BIOIMPEDANCE ACQUISITION SYSTEM DESIGN

In this chapter, a brief background about various bioimpedance acquisition instrumentation and methods is first presented. Then, two miniaturized bioimpedance acquisition systems that utilize different measurement techniques along with a novel calibration technique that reduces the measurements error are presented. Both systems and the calibration technique are validated and tested with bench-top methods for their accuracy, resolution, drift and power consumption to understand their usability in a wearable form factor.

2.1 Instrumentation and Methods to Measure Bioimpedance

Bioimpedance acquisition systems usually consist of three main building blocks: a current source, voltmeter and signal processor. First, the current source injects a small, safe constant stimulus alternating current at a specific frequency into the body to excite the tissue volume under investigation. Then, the potential drop across this tissue volume due to the excitation current is measured using an amplifier, and its output is then processed along with the current source's reference signal to calculate the impedance of the tissue using Ohm's law. This is performed by demodulating both signals to generate the real and imaginary components of the measured voltage representing the complex impedance of the tissue. Traditionally, the signal demodulation was performed using an analog circuit demodulator that consumes substantial power, but more recently there has been a shift towards using digital processing to preserve energy especially for battery powered

applications [27, 34-37]. Together the demodulated real and imaginary outputs of the signal processor are calibrated by measuring a known single resistor where the gain factor and phase shift of the acquisition system are calculated. Both the gain factor and phase shift values are then utilized to map the demodulated output of the signal processor to the measured bioimpedance.

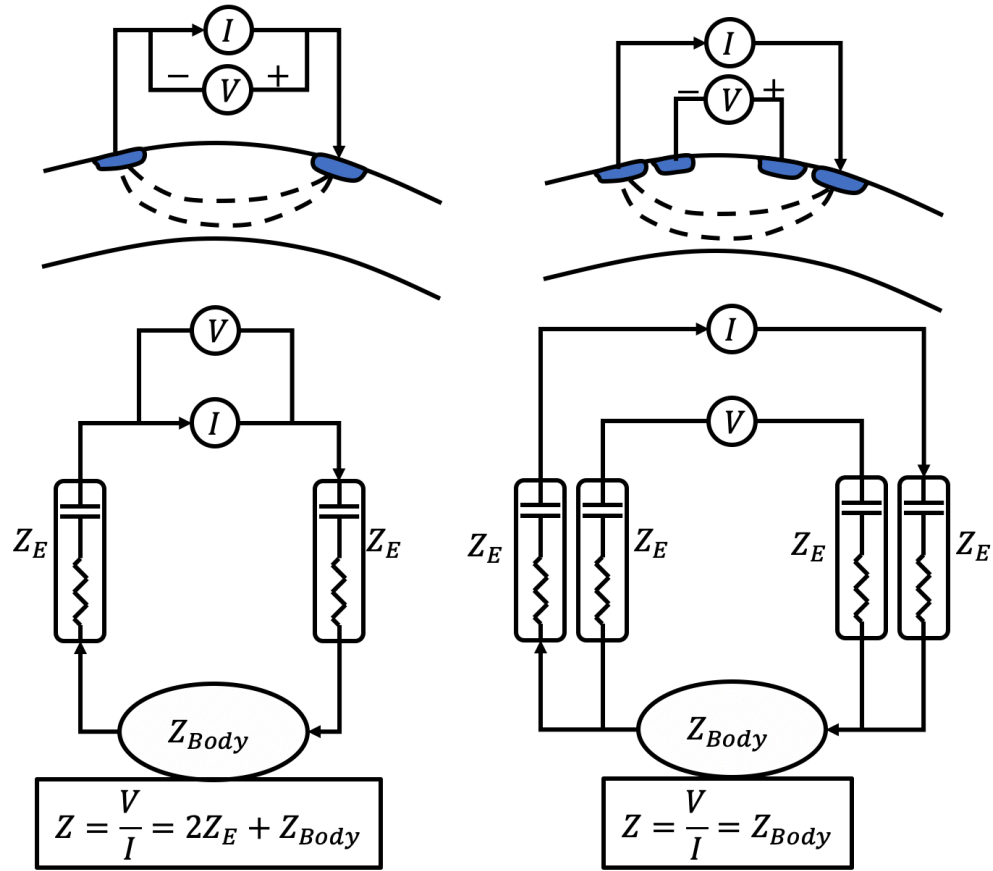


Figure 1. Bioimpedance Acquisition System Interface. (left) The less complex 2-electrode configuration measures the combined impedance of the tissue and the skin-electrode interface. (right) 4-electrode configuration isolates the tissue impedance making it more accurate but also more complex than the 2-electrode configuration.

The interface between the system and the body is generally through 2 or 4 wet adhesive-backed silver/silver-chloride (Ag/AgCl) electrodes or dry polymer electrodes [27]. In the 2-electrode configuration the voltage drop is measured across both the skin

electrode interface impedance and the tissue volume combined as shown in Figure 1 (left). This makes it undesirable for applications that track longitudinal minute changes in the tissue's bioimpedance due to the relatively large variability in the skin-electrode impedance over time. A more accurate method uses 4-electrodes which eliminates the skin-electrode interface impedance but adds complexity to the system interface, where the current is injected through the distal electrodes and the voltage is measured by the proximal electrodes as shown in Figure 1 (right). This allows the system to isolate the impedance of the tissue under investigation from the skin-electrode interface impedance, but also requires more electrodes and circuitry.

2.2 System Level Design

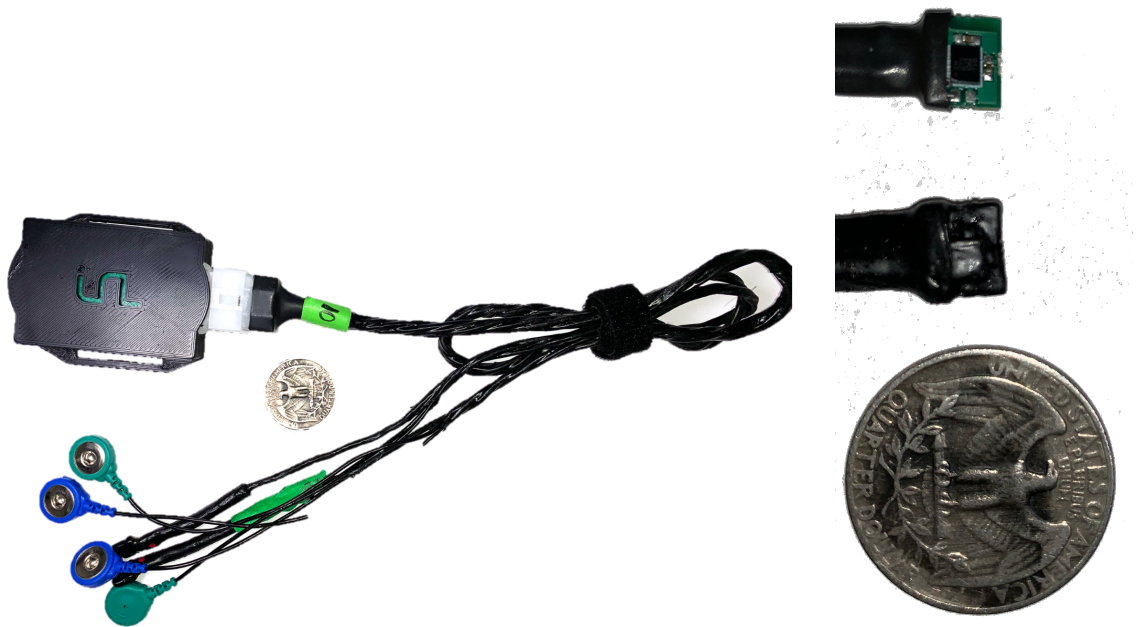


Figure 2. Bioimpedance Acquisition System. (left) The final miniaturized system presented in this work consists of a custom 3D printed box that houses the custom built 4-layer PCB,

with a 12-pin amplifier connector that interfaces to the electrode snaps, (right) temperature and inertial measurement sensors placed on the tissue of interest.

To quantify tissue edema in a wearable setting, a miniaturized, accurate and robust custom multi-modal system is developed with the primary purpose of measuring: (1) bioimpedance, (2) inertial measurements and (3) temperature of the tissue of interest and log them onto a secure digital (SD) card for offline analysis. For usability purposes, the system has to be small, easy to use, battery powered, and able to collect data for more than 48 hours. For practicality purposes, the system is split into two main components: the main box and the peripheral sensory cable assembly to allow placing the sensors in various areas of the body easily. First, the main box shown in Figure 2 consists of a 500 mAh Lithium-ion battery to power the printed circuit board containing (1) two voltage regulators (analog and digital), (2) a battery charger, (3) a microcontroller (SAMD21, Atmel, San Jose, CA), (4) an SD card shield and (5) bioimpedance sensor circuitry as shown in Figure 3. Outside the box, there is a robust 12-pin amplifier connector, power switch and three LEDs to notify the user of a system error, low battery and the battery charging status. Second, the cable assembly consists of four ECG/EKG electrode snaps and two small printed circuit boards each with the inertial measurement units (IMU) (LSM6DS3, STMicroElectronics, Geneva, Switzerland) and temperature sensors (TMP112, TI, Dallas, TX) to be placed on the tissue of interest.

2.2.1 Bioimpedance Circuitry

Until recently, all three building blocks of bioimpedance acquisition systems were developed using analog circuitry which increased the system's size, complexity and power consumption. However, significant advances in analog integrated circuits have made it

possible to embed these blocks onto an integrated circuit (IC). In this work, we have studied and compared multiple ICs that are capable of or have the potential for performing 4-electrode BIA. Table 1 shows a brief comparison between four ICs available on the market.

Table 1. Comparison between different integrated circuits capable of performing BIA.

IC	Max-300001	AFE4300	AD5933	AD5940
Size	4mmx4mm	12mmx12mm	5.4mmx4.5mm	4.2mmx3.6mm
Main Purpose	ECG and BioZ (only Real component in Z)	Weight Scale Body Mass Index	Impedance Spectroscopy	Electrochemical Frontend
Error in Impedance Measurement	-3% to +3%	Up to 2.43%	Up to 0.5%	Up to 0.5%
Frequency Options	Limited	Limited	High Resolution (1k to 100kHz)	High Resolution (500 to 250kHz)
External Circuitry	Minimal	Minimal	Requires AFE	Minimal

First, the MAX30001 (Maxim Integrated, San Jose, CA) measures the real component of the complex impedance only and for limited frequencies. This disallows performing Fricke-Morse parameter estimation as complex non-linear least squares estimation requires both the complex and real parts of the impedance at multiple frequencies. Furthermore, the mean error for this IC is relatively high. Second, the TI-AFE5400 (Texas Instruments, Dallas, TX) is designed for full body composition analysis and has a large mean measurement error for small impedance measurements. That shortcoming makes the TI-AFE5400 suboptimal for localized BIA. Third, Analog Devices'

AD5933 is a suitable IC for our application due to its accuracy, programming flexibility and low power consumption. This IC is capable of measuring bioimpedance for frequencies ranging between 1 kHz to 100 kHz with a resolution of 1 Hz. It is also capable of providing the real and imaginary components of the measured impedance with an accuracy of 0.5%. The main downside to use of the AD5933 is that it is designed to perform two electrode impedance measurements, therefore it requires an external analog front end (AFE) to allow 4-electrode impedance measurements. Lastly, the AD5940 is the successor of the AD5933, designed to perform accurate bioimpedance measurements, but requires longer measurement time as discussed later in Section 2.6.3. In Sections 2.3 and 2.4, two bioimpedance systems that utilize the AD5933 and AD5940 are presented.

2.3 Bioimpedance Acquisition System Design Utilizing the AD5933

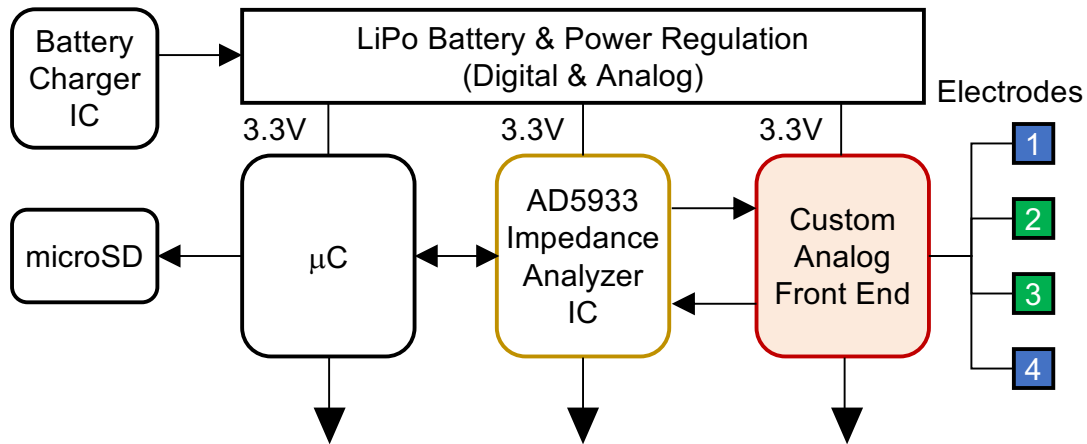


Figure 3. Block diagram of the bioimpedance acquisition system utilizing the AD5933 impedance analyzer to measure the tissue's bioimpedance. (right) AD5933 BIA system block diagram.

The AD5933's theory of operation is as follows: an unknown impedance is connected between the V_{out} and V_{in} pins. A constant voltage output from V_{out} is applied to

one of the unknown impedance's terminals and the other terminal at V_{in} is connected to a trans-impedance amplifier (TIA). The TIA converts the input current flowing through the impedance to a voltage that is measured using an analog to digital converter (ADC) at 800K samples per second. Finally, the digitized signal is then fed into the arithmetic core which performs the operation in (5).

$$X(f) = \sum_0^{1024} (x(n)(\cos(n) - j\sin(n))) \quad (5)$$

The result of the operation in the arithmetic core ($X(f)$) is the power of the signal at frequency f , where $x(n)$ is the ADC output and the sin and cosine signals are provided by the DDS core. The output ($X(f)$) requires a simple calibration to correlate the measured real and imaginary components to the impedances' real and imaginary components. This calibration process is described as follows in the datasheet:

1. Measure a known resistive load (i.e. 100 Ω)
2. Retrieve the 16-bit real and imaginary values from registers 0x94 to 0x97
3. Using the following equations to calculate the gain factor and phase shift as follow:

Let re be the real 16-bit value from registers 0x94 and 0x95 and im be the imaginary 16-bit value from registers 0x96 and 0x97. Where

$$\text{Impedance} = 100 \Omega \quad (6)$$

$$\text{Magnitude} = \sqrt{re^2 + im^2} \quad (7)$$

$$\text{Gain Factor} = \frac{1}{\text{Magnitude} * \text{Impedance}} \quad (8)$$

$$\text{Phase Shift, } \phi = \tan^{-1} \left(\frac{\text{im}}{\text{re}} \right) \quad (9)$$

2.3.1 Custom Designed External AFE for the AD5933

To enable the AD5933 to perform 4-electrode bioimpedance measurements, we designed an AFE with power consumption and accuracy in mind. In the literature, there are numerous AFE designs for repurposing the AD5933 that generally consist of a voltage-to-current converter, an instrumentation amplifier (IA), and a second voltage to current converter. The first voltage-to-current converter block ensures safety by limiting the current applied to the body to less than the 280 μA_{rms} threshold set by the IEC-60601 standard [38]. The potential drop across the impedance from the excitation current is measured using the IA whose output signal is passed to an inverting voltage-to-current converter to generate the signal the AD5933 is expecting for normal operation.

In July 2019, Analog Devices released their AD5933 successor: the AD5940, a capable but complex IC designed to perform a variety of electro-chemical measurements. Equipped with very accurate and modular bioimpedance acquisition building blocks, it became a very attractive solution for a new bioimpedance acquisition system.

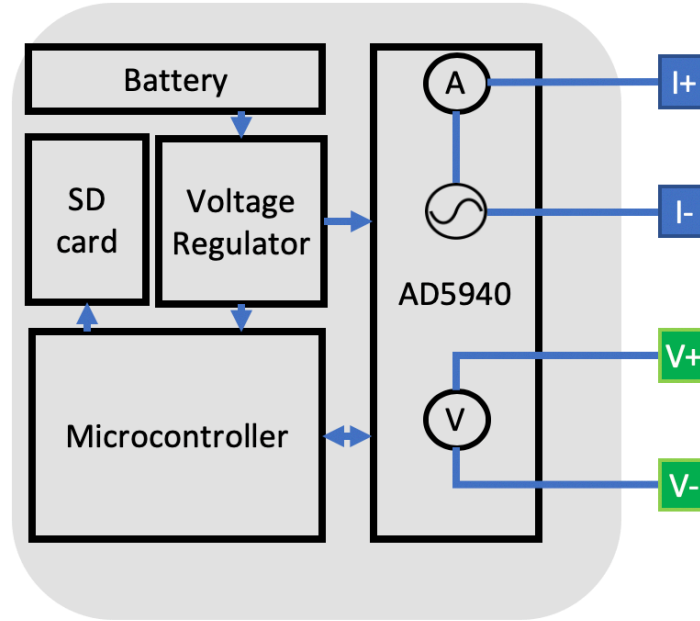


Figure 5. Block Diagram of Bioimpedance Acquisition System Utilizing AD5940. The IC uses a novel approach to measure bioimpedance that allows having an infinite dynamic range and high skin-electrode interface impedance but requires taking two measurements: the current flowing through the tissue and the voltage due to this current.

2.4.1 AD5940 Theory of Operation

One of the biggest challenges with traditional bioimpedance acquisition systems is the limited dynamic range. When using a constant current source to excite the tissue through distal electrodes, the sum of the two skin-electrode interface and the tissue impedances has to be less than the current source's output impedance threshold. Furthermore, since the system needs to be wearable, using a Li-Po battery restricts the

operational voltage range to 3.3 V limiting the range of impedances it can drive. This in turn restricts the usage of the system to gel-electrodes as they guarantee a relatively low skin-electrode interface impedance, and to certain low impedance body parts. However, the AD5940 allows a novel but complicated way to overcome this limitation, by using a constant voltage source to excite the tissue rather than a constant current. By doing so, increasing the skin-electrode interface and tissue impedance would only decrease the current flowing through the tissue allowing a *theoretically* infinite dynamic range but adding a new complication. Having a varying current flowing through the tissue at the distal electrode means that measuring the voltage through the proximal electrodes only is not sufficient to calculate the tissue's bioimpedance as the current flowing is not constant. Hence, the AD5940 operates by having a current meter in series with the voltage source to measure the current flowing through the tissue at the distal electrodes and a voltmeter to measure the corresponding voltage at the proximal electrodes as shown in Figure 5. This is done by multiplexing the terminals of the IC's internal ADC to a transimpedance amplifier located at the voltage electrode terminal to measure the current flowing through the tissue, then multiplexing the ADC's terminals to the proximal voltage electrodes to measure the voltage difference due to that current.

2.4.2 Custom Designed External AFE for the AD5940

For this system, the circuit design is substantially simpler as the AD5940 does not require an AFE to perform 4-electrode bioimpedance measurements. Instead, it only requires having a current limiting resistor at the terminals connected to the voltage source to ensure that the maximum possible current applied to the body tissue is less than the safety threshold defined by IEC-60601. Therefore, two 1 k Ω resistors and DC blocking

capacitors are added to the terminals of the voltage source. Otherwise, the remainder of the embedded systems are the same as the previous version system using the AD5933.

2.4.3 AD5940 System Calibration

Similar to the AD5933, the AD5940 is calibrated using a single known resistor by calculating the gain factor and phase shift as presented in Section 2.3.1. Specifically, the AD5940 generate two arbitrary 18 bit real and imaginary number for the current and voltage measurements that need calibrating to map these values to the measured impedance. A known single on-board resistor is connected between the R_{cal} pins on the IC where a calibration scheme similar to the one presented in Section 2.3.1 is utilized.

2.5 Firmware and Software Architecture

Since both systems will be used in multiple studies with different sampling rates, bioimpedance measurement frequencies and measurement sensors, a very modular firmware and software front-end are created. An interrupt-based firmware is developed using Atmel Studio Framework (Atmel, San Jose, CA) where each of the IMU, temperature and bioimpedance sensors state-machines are updated in a timer-based interrupt function every 1 ms. Data from all three sensors are saved onto three separate double-buffers to ensure a consistent sampling rate and no dropped packages. Specifically, while the data from the three sensors are saved to one half of the buffer, the other half is written to the SD card. Once half of the buffer is full, the data is then saved to the second half and this half is written to the SD card and so on. The size of the buffer, sampling rate of the sensors and the writing speed to the SD card are all optimized to ensure no data is lost while having the fastest sampling rate possible within the microcontroller's abilities.

To ensure a streamlined operation for both systems, a JavaScript Object Notation (JSON) dictionary is utilized by writing to the SD card at startup specifics about the firmware such as the version and sensors available. Moreover, for every sensor, specifications relevant to each sensor such as the data packet size and content are also written to the JSON dictionary. After data collection, the data from the SD card is read using Python and the JSON dictionary is used to parse the data accordingly.

2.6 Novel Physiology Driven Calibration Technique

The AD5933's datasheet calibration method requires an inverse relationship between the impedance measured and the current input to the IC at V_{in} (i.e. as the impedance increases, the current at V_{in} decreases). In the presented design, the output of the IA is fed into the input of the IC through a resistor, leading to a direct relationship between the impedance measured and the input current. To mitigate this, researchers have used an inverting current-to-voltage converter at the output of the IA to ensure the IC's normal operation and allow for the datasheet's calibration method [39-42].

However, in the design used here, the datasheet's calibration technique was adapted to the circuit design to avoid increasing the size of the AFE. The modified calibration technique is shown in (10):

$$\text{Gain Factor} = \frac{1}{\text{Magnitude} * \text{Impedance}} \rightarrow \frac{\text{Impedance}}{\text{Magnitude}} \quad (10)$$

This modification made it possible to calibrate the presented design and obtain results comparable to the results in the literature (Error~2%) but with using a smaller AFE [39-42].

2.6.1 Linear Regression Bases Multi-Point Calibration

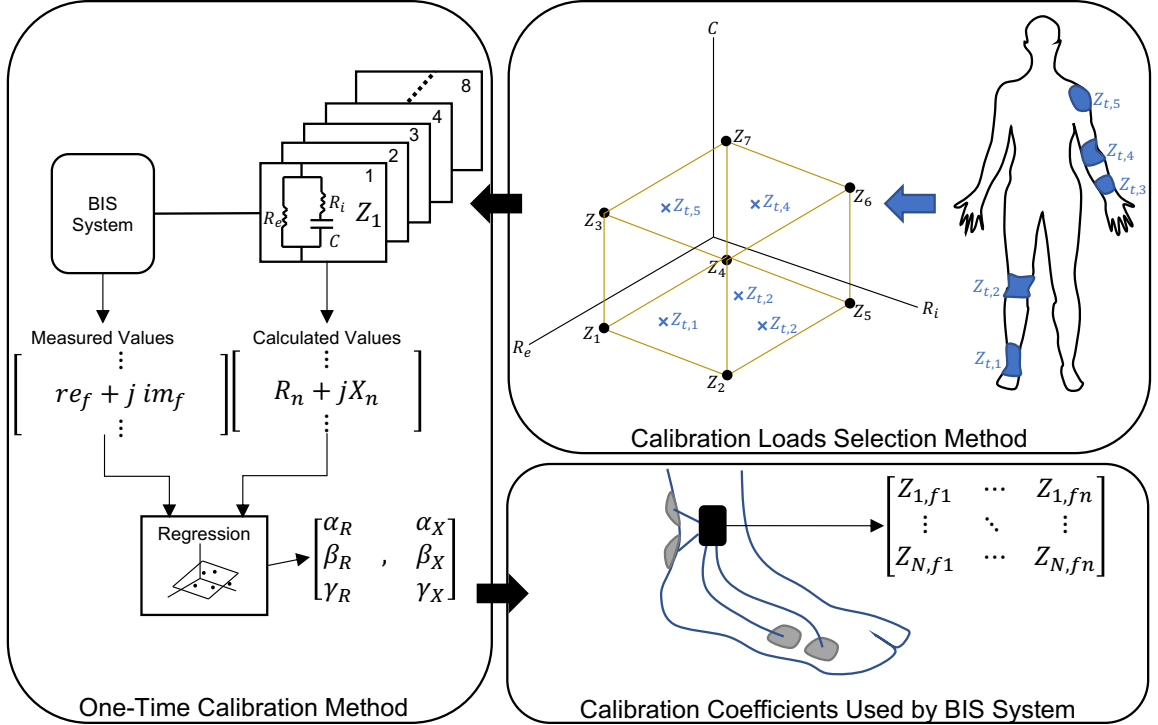


Figure 6. Novel physiology drive calibration technique used to reduce measurement error by utilizing least squares' error reduction abilities. The 2R1C space of R_e , R_i and C is utilized to optimize the calibration impedances. Specifically, eight 2R1C impedances that span the 3D space up to the system's dynamic range, encompassing the impedance of various body parts are used to calibrate the system using linear regression.

To further reduce the measurement error, a physiology driven regression-based approach that can be used with both systems is implemented. The method utilizes least squares' error reduction ability by finding the optimal calibration coefficients. Figure 6 shows an overview of the calibration technique which uses eight 2R1C impedances that

span the R_e , R_i and C_x space of physiologically meaningful impedances. This calibration methodology uses multiple impedance loads coupled with a multivariate linear regression algorithm to allow for the outputted 16-bit raw values generated by the IC to be mapped to accurate real and imaginary impedance values. Additionally, rather than using a simple resistive load, the standard 2R1C model for biological tissue is utilized to allow for this mapping operation to be accurate across the full range of measured frequencies [27, 30, 31]. Specifically, this method can be described as follows: Let Q be a $N \times 3$ matrix combining the 16-bit real, re_f , and imaginary, im_f , values from the AD5933 for N -loads measured at frequency f .

$$Q_f = \begin{bmatrix} re_f[1] & im_f[1] & 1 \\ \vdots & \vdots & \vdots \\ re_f[N] & im_f[N] & 1 \end{bmatrix} \quad (11)$$

Where $Z_{Re,f}$ and $Z_{Im,f}$ are the real and imaginary components of the impedance measured at frequency f mapped from re_f and im_f using the coefficients in $C_{Re,f}$ and $C_{Im,f}$, respectively, as in (12) and (14).

$$Z_{Re,f} = Q_f \cdot C_{Re,f} \quad (12)$$

where

$$Z_{Re,f} = \begin{bmatrix} Z_{Re,f}[1] \\ \vdots \\ Z_{Re,f}[N] \end{bmatrix}, C_{Re,f} = \begin{bmatrix} \alpha_{Re,f} \\ \beta_{Re,f} \\ \gamma_{Re,f} \end{bmatrix} \quad (13)$$

$$Z_{Im,f} = Q_f \cdot C_{Im,f} \quad (14)$$

where

$$Z_{Im,f} = \begin{bmatrix} Z_{Im,f}[1] \\ \vdots \\ Z_{Im,f}[N] \end{bmatrix}, C_{Im,f} = \begin{bmatrix} \alpha_{Im,f} \\ \beta_{Im,f} \\ \gamma_{Im,f} \end{bmatrix} \quad (15)$$

2.6.2 Optimizing the Impedances Used for Calibration

First, we confined the space of impedance measurements spanned by these three values – 2R1C, i.e., two resistors and one capacitor $[R_e, R_i, C_x]$ – to a range that is physiologically meaningful. Specifically, values from the existing literature are combined with measured values using commercially available gold standard bioimpedance hardware (SF87, Impedimed, Australia) to form the space of calibration values required. Furthermore, the number of impedances required to optimize accuracy in impedance measurements with this calibration is investigated, and found that $N=8$, with the particular 2R1C impedance values matching the vertices of the three-dimensional physiologically meaningful impedance space for joint edema provided the lowest error.

Investigating the optimal combination of calibration impedances, (1) the span of the combination of calibration impedances in 2R1C space and (2) the number, N , of calibration impedances used in the combination are varied. Specifically, three different combinations that had the following spans: $[R_e]$, $[R_e, R_i]$ and $[R_e, R_i, C_x]$ are tested. For each of these combinations, the number of calibration impedances in this span is varied. It was found that increasing the number of impedances only reduced the random error in measurements. However, the measurement error of an unknown impedance heavily

depends on the distance in the 3D space between the measured impedance and the span of the calibration impedances. Hence, the system is calibrated with impedances that span the linear space up until our dynamic range encompassing the physiologically meaningful impedances as in Figure 6, ensuring accurate measurements for impedance values falling within this space.

2.7 Bioimpedance Acquisition System Characterization

To validate the calibration method, five test 2R1C loads that simulate the bioimpedance of the limbs of interest (e.g., knee, ankle, shoulder, wrist and elbow) are assembled using discrete resistors and capacitors measured separately by Agilent's 34410A Digital Multimeter. The values retrieved from Agilent's DMM are used in Python to simulate the 2R1C impedance at the frequency range between 5 kHz and 100 kHz with 371 Hz resolution similar to the frequencies measured by both systems. From the simulation, real and imaginary values of the 2R1C impedances at the different frequency points are calculated and will be used to evaluate the error in measurements from the device presented. For both systems, their accuracy, resolution and drift, being key parameters for sensor characterization, are tested and quantified.

2.7.1 AD5933 Based System Characterization

Starting with the AD5933-based system, the five 2R1C characterization impedances are measured over the frequency range and calibrated with the presented calibration model to test the system accuracy. The mean error across in real and imaginary components of the characterization impedances over all the frequencies measured is calculated to be $0.4\ \Omega$ and $0.54\ \Omega$ respectively. Next, the system's measurement resolution

is tested by measuring a resistor network compromised of five $0.1\ \Omega$ resistors with 1% tolerance in series to the characteristic 2R1C loads, then removing one resistor at a time. From this test, resistance changes of $0.2\ \Omega$ at any frequency for any of the 2R1C characterization loads are detectable above the noise floor of the system. Finally, for drift, one of the five characterization 2R1C impedances is measured for three days continuously and monitored changes in the impedance spectrum. There was no drift in the bioimpedance measurements throughout the experiment, except for a slight variability of $0.0125\ \Omega$ in resistance at 5 kHz and $0.1\ \Omega$ in resistance at 100 kHz due to a temperature variation of 5°C . Table 3 shows a comparison of our current design to other AD5933-based designs in literature.

Table 2. AD5933 System Properties

Parameter	Value
Power Consumption-Data collection	24 mA
Power Consumption-Sleep Mode	1.5 mA
Sampling Rate	3 BIS/min
Battery life	111 hours
Size	5.2x3.8x1.8 cm
Weight	32 g
Frequency Range	5kHz – 100kHz
Frequency Resolution	256 Hz
Dynamic Range	200 Ω
I_{body}	280 μA_{rms}
Mean Error in R	0.4 Ω
Mean Error in X	0.54 Ω
Resolution	0.2 Ω

Table 3. AD5933-Based Designs Comparison with similar designs from the literature that utilize different calibration techniques and AFE designs.

Number of test impedances	5 (only resistive)	1 (2R1C)	2 (1R and 1L)	2 (RC Networks)	Complex impedances	Complex impedances	1 (RC network)	5 (2R1C impedances characteristic of joints)
Impedance Range	1.6 k Ω	10 k Ω	9 Ω - 18M Ω	10 Ω -1k Ω	5k Ω - 25k Ω	1 Ω -1k Ω	10 Ω - 1k Ω	0 Ω -200 Ω
Reported Error	1% (Not clear if real or imaginary)	1.3% argument and 2.5% modulus	\pm 2%	2.5% modulus and 4.5% argument	4% Magnitude and 2 degrees in phase	3%	Modulus error 0.5% to 2.5%, Phase error 2% to 4.5%	Absolute Mean error Real 0.4 Ω (0.34%) Imaginary 0.54 Ω (1.36%)
Measurement Frequencies	5kHz-100kHz	5kHz-100kHz	1kHz-100kHz	100Hz-200kHz	10Hz to 100kHz	1-350 kHz	100Hz-200kHz	5kHz to 100kHz
Power Consumption	-	-	-	34mA-Data Acquisition 0.2mA-Sleep Mode	-	-	34mA-Data Acquisition- 0.2mA-Sleep Mode	24mA in Data Acquisition- 1.5mA in Sleep mode
Number of active components	-	> 8	3	4	5	-	4	2
Hardware Topology	4-electrode VCCS + IA + V to I	4-electrode VCCS + IA + V to I	4-electrode IA + V to I	4-electrode VCCS + 2*Buffer + IA	2-electrode with constant voltage applied	4-electrode IEC 60601 compliant used in [42]	4-electrode VCCS + 2*Buffer + IA	4-electrode (IEC-60601 compliant) VCCS+IA
Calibration Method	Datasheet method	Datasheet method	Datasheet method	Datasheet method	Datasheet method	Datasheet method	Datasheet method	Linear regression
Paper	Seoane et al[42]	Margo et al [41]	Breniuc et al[40]	Bogóñez-Franco et al[39]	Tnulasi et al[43]	Hafid et al[44]	Bogóñez-Franco et al[45]	Mabrouk et al [46]

2.7.2 AD5940 Based System Characterization

Using the calibration technique presented in Section 2.6 and the characterization methodology in Section 2.7 with the AD5940 we are able to reduce the mean error in resistance and reactance from 2.2 and 1.5 Ω respectively when following the datasheet's calibration technique to 0.5 and 0.53 Ω respectively. Furthermore, the system's bioimpedance measurement resolution is tested by estimating the SNR when measuring the same impedance for a period of 3 days. From this test, the calculated mean variation in the signal is less than 0.04 Ω at all frequencies which imputes a resolution of 0.04 Ω . Regarding power consumption, the system is able to collect data continuously for 14 hours on a full charge and 176 hours when performing one spectroscopy per minute. Table 4 outlines the relevant system characteristics.

Table 4. AD5940 System Properties

Parameter	Value
Power Consumption-Data collection	20 mA
Power Consumption-Sleep Mode	1.5 mA
Sampling Rate	1 BIS/min
Battery life	176 hours
Size	5.2x3.8x1.8 cm
Weight	32 g
Frequency Range	5kHz – 100kHz
Frequency Resolution	256 Hz
Dynamic Range	Infinite
I_{body}	Maximum 280 μA_{rms}
Mean Error in R	0.57 Ω
Mean Error in X	0.53 Ω
Resolution	0.04 Ω

2.7.3 *AD5940 vs AD5933 Based Design*

Although both systems have very similar measurement accuracy and resolution, the AD5940 excels in having a better power consumption and more importantly a theoretically infinite dynamic range which is very useful in body areas with high bone density such as the fingers and hands. It also allows using different electrode shapes and sizes, enabling more innovation in the system packaging making it more attractive for wearable applications. Furthermore, the AD5940 is more customizable than the AD5933, especially when deciding the bioimpedance measurement frequencies. Specifically, the AD5933 is programmed on sweep basis by first defining the start frequency, number of frequencies and increment, then initiating the sweep. Once the AD5933 starts measuring, it is polled for an update on the measurement status till it's done, then a command is sent to start the next frequency measurement and so on till the sweep is complete. This is challenging in applications that require measuring distinct frequencies (i.e. not distributed equally) and when repeating the sweep, the IC resets requiring a long settling time making it unattractive for applications that study the dynamic changes in impedance at multiple frequencies. However, the AD5940 provides programming flexibility where it can measure any frequency at any time, but it comes at a cost. Since it is very modular, processing the commands to place all the different system components in the correct setting takes time. Specifically, the time it takes to perform one measurement by the AD5933 at any frequency

is 2 ms while the AD5940 is 8 ms, and since it requires measuring both the voltage and the current, this time is double to 16 ms per frequency.

2.8 Conclusion

This chapter described various design methodologies for a wearable bioimpedance acquisition system utilizing different ICs with the potential to perform accurate longitudinal tracking of localized bioimpedance. Both systems presented were calibrated using a novel physiology driven calibration technique optimized to increase the system accuracy and resolution. This calibration technique reduced the bioimpedance measurement error by up to 200% compared to traditional methods, showing the methods applicability with different design methodologies. For one of the systems, this calibration technique allowed reducing the hardware complexity hence reducing power consumption and increasing SNR. This chapter also presents a physiology driven validation technique for bioimpedance acquisition system that uses 2R1C impedance of various body parts to test the system's accuracy, resolution and drift being key parameters in longitudinal tracking of a tissue's bioimpedance. Finally, a comprehensive comparison between the two systems utilizing different measurement techniques is presented emphasizing on the applications each system would perform better with. The systems presented will help overcome the first hurdle for using bioimpedance in a wearable setting by providing a miniaturized battery power solution that can be used with dry electrodes for longitudinal tracking.

CHAPTER 3. SYSTEM VALIDATION IN THE CONTEXT OF ROBUST TRACKING OF EDEMA VOLUME IN THE ANKLE JOINT

In this chapter an extensive validation of the miniaturized bioimpedance acquisition system in the context of robust quantification of ankle edema is presented. Specifically, novel methods and algorithms are developed for robust and unobtrusive tracking of changes in edematous fluid volume in the ankle joint that remove the limitation from prior work in the literature. The system, methods and algorithms will be validated in human subject and cadaver model studies.

3.1 Introduction

The ankle is one of the most frequently injured joints on the body and accounts for 10-30% of all sports injuries [47-49]. Ankle injuries require months and sometimes years to fully recover, and the risk of re-sprains range from 3 to 34% [48, 50, 51]. An estimated 628,026 ankle sprains occurred annually between 2002 and 2006 in the United States, 225,114 of which were lateral ankle sprains. Accordingly, the overall estimated incidence rate for ankle sprains is 3.29 per 1000 person-years [52] resulting in an annual aggregate health-care cost of \$2 billion [53].

A lateral sprain to the ankle joint typically results from excessive inversion and plantar flexion, and is classified as grade 1-3 based on the severity of the injury: specifically, the presence / absence of ligament tearing and any joint instability resulting from the injury yields a grade of 1 (mild), 2 (moderate), or 3 (severe) to characterize the

sprain [54]. For all grades of sprains, pain and swelling are common. Key objectives of the rehabilitation process are to regain range of motion, alleviate pain and swelling, and strengthen the smaller muscles stabilizing the foot. The ability to conduct a full athletic practice without ensuing pain or swelling is typically used as a criterion for determining readiness for the athlete to resume normal competition [54].

While evaluating the level of swelling (edema) in the joint is indeed an important part of characterizing the grade of injury and state of rehabilitation following a sprain, such evaluations can only be performed by a clinician, physical therapist, or athletic trainer during physical examination, and are qualitative and subjective. Examination methods based on diagnostic imaging provide quantitative metrics of joint health [55, 56], but are less commonly used during rehabilitation since they are expensive and time consuming. Beyond the clinic / training room, such as in the home, the only technologies available for quantifying the state of ankle health are based on inertial measurements to assess range of movement [57].

BIA is a non-invasive method for assessing the composition of biological tissue based on the injection of a small electrical current at a single frequency and the measurement of the resultant voltage drop across the sample [27]—the ratio of the measured voltage to the injected current then yields the BIA for that tissue sample (e.g. increased edema decreases the tissue impedance since fluid is less electrically resistive than muscle, fat, or bone [30]). BIA has been demonstrated in recent studies as a possible means of quantifying edema resulting from acute injuries [24, 58]. Previous work done by Hersek et al showed that BIA for an acutely injured knee joint was significantly lower than the

contralateral side for a cohort of student-athletes, and that with surgical repair and rehabilitation the difference between the two sides subsided [59].

Specifically, SFBIA is a type of bioimpedance measure of tissue that uses only a 50 kHz current frequency which is considered the cutoff frequency of biological tissue, or the frequency at which the current is passing through both the extracellular and intracellular paths [15]. In the literature, SFBIA has been used for evaluating the health of muscles and joints using two methods: comparing the acutely injured muscle / joint to the contralateral healthy muscle / joint, or by monitoring an injured joint longitudinally over the course of rehabilitation [24, 26]. In the context of joint injury, SFBIA can potentially quantify edema, but there are several limitations, including: (1) the inability to classify the source of bioimpedance changes (i.e. edema versus structural damage versus blood flow), (2) a need for normalization of the bioimpedance for proper interpretation, and (3) variability in the electrode placement and tissue placement can greatly alter the signal. To implement SFBIA on an injured patient, the signal from the injured joint of interest is normalized against the contralateral joint or against its baseline signal prior to injury. Either way, this normalization requires an increased number of sensors or an increased period of time wearing them which limits the portability and ease of use of the system. Additionally, SFBIA is highly sensitive to electrode placement and the position of the tissue, which limits the recordings to laboratory or clinical settings while the patient is immobile. Ideally, with a novel, more portable implementation of BIA, a patient with an injured joint could monitor their rehabilitation over time and the system could provide an early warning sign before reinjury occurs.

3.2 Edema Quantification Methods

To overcome some of the limitations of SFBIA, a BIA method for quantifying joint edema based on positional changes of the ankle joint is developed. This technique compares the effects that changes in ankle position have on the range of the resistance measured at 5 kHz against the range of the resistance measured at 100 kHz. Extracellular fluid associated with ankle edema is delocalized and therefore free to move around in the joint space as a subject changes the position of his/her ankle. For example, as the person rotates his/her ankle, the edema moves around inside the joint space due to gravity and forces exerted by the structures inside and around the ankle. Electrodes positioned proximally and distally to the joint for BIS measurement allow current to be injected into the ankle, where different frequency components of this current travel at different depths within the tissue. Skin effect theory states that low frequency current flows deeper into the tissue, since it cannot penetrate cell membranes and must travel along extracellular paths (i.e. interstitial fluid and blood). In contrast, higher frequency current can penetrate cells, so it travels along a more superficial, shorter path between the electrodes. [27, 30, 31].

This differential measurement technique utilized the frequency-dependency of the penetration depth of current within the ankle: by moving the ankle through multiple positions during the BIS measurement, the edematous fluid is deliberately moved to different depths within the ankle. Low frequency currents that penetrate deeply within the tissue are dependent on the extracellular fluid for passage. A change in the volume of extracellular fluid deeper into the tissue, close to the current's path, would have a significant impact on bioimpedance measurement at low frequency. For high frequency currents that penetrate the cell membranes, they are more dependent on intracellular fluids

for passage. Thus, a change in the volume of extracellular fluid close to its path would have less of an impact on the bioimpedance measurement at a high frequency. For a healthy joint, as a person moves his/her ankle there is a similar change in bioimpedance measured at high and low frequencies because, in comparison to an injured joint, there is a relatively small volume of extracellular fluid that is displaced with ankle movement. Essentially, this method compares the *range of change* in bioimpedance at low frequency associated with ankle position change to the *range of change* in bioimpedance at high frequency associated with these changes. Specifically, the ratio of the changes in bioimpedance at 100 kHz to the changes in bioimpedance 5 kHz is computed to normalize the change to a score, h_α , that can be relatable to all subjects:

$$h_\alpha = \frac{\Delta R_{100\text{kHz}}}{\Delta R_{5\text{kHz}}} \quad (16)$$

where

$$\Delta R_f = \max(R_f) - \min(R_f) \quad (17)$$

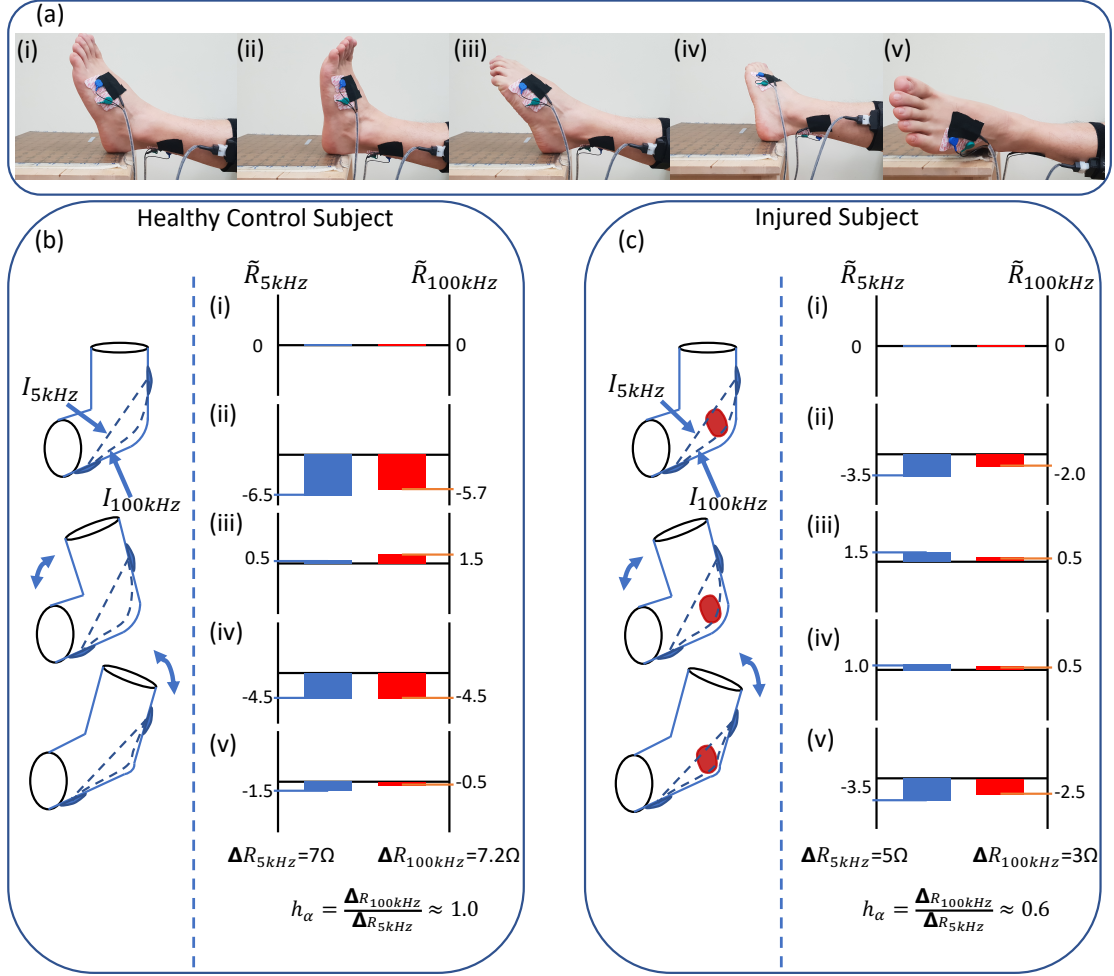


Figure 7. The five different posture used in the experiment. (b) and (c) show the change in impedance normalized to the resting position along with a small sketch showing the edema moving through the different current bands for (b) a healthy control subject and (c) an injured subject.

To better understand h_α , Figures 7(b) and 7(c) show the change in resistance measured at 5 kHz and 100 kHz normalized to the resting position (i.e. the change in impedance from resting position) for a healthy control subject and an injured subject respectively. For the control subject, we saw a similar range of change in resistance measured at 5 kHz and 100 kHz over the five different ankle positions. The h_α score for the control subject's ankle was very close to 1.0 due to the lack of extracellular edema in

the ankle joint. For the injured subject, we see a similar trend for the resistance measured at 5 kHz and at 100 kHz, but the magnitude of the change in resistance is higher for the resistance measurement at 5 kHz. The h_α for injured ankle was 0.6 due to the existence of extracellular edema in the ankle joint which causes a bigger range of change in the resistance measured at low frequencies than at higher frequencies. Note that for the healthy subject's data presented in Figure 7(b) the highest and lowest impedances are at positions (III) and (II), respectively, compared to positions (III) and (V) for the injured subject's data presented in Figure 7(c). This was a common trend in the data from the human study for the healthy and the injured cases, but not conclusive to choose these specific positions for analysis. The change in impedance at different positions suggests that the compression and relaxation of the muscles and tendons in the ankle joint have an effect on the bioimpedance measured [60, 61] but this change is very similar at low and high frequencies for healthy ankle joints. Hence this method compares the *range of change* (ΔR_f) in the ankle impedance at 5kHz and 100kHz caused by changing the ankle position in four axes independent of the position.

3.2.1 Edema Quantification Protocol

To validate the presented method, a study was performed on eight subjects, five male subjects and three female subjects between the age of 18 and 30 years old, with no recent ankle injuries and five subjects, four male subjects and one female subject between the age 18 and 30 years old with recently incurred (within two days) acute lateral ankle sprains. The study was approved by the Georgia Institute of Technology Institutional Review Board (IRB). For each subject, data were collected with the BIS system presented in Chapter 2 for 10 minutes at 5 different ankle positions composing the entire range of

motion of the ankle in four axes (resting position, dorsiflexion, plantarflexion, eversion and inversion) for 2 minutes each as shown in Figure 7(a). The subjects were asked to sit upright with their legs resting horizontally at 90 degrees to their torso, to avoid a change in impedance due to blood pooling. The protocol was performed on the eight control subjects with no recent ankle injuries five times for each ankle over a period of 21 days. For the injured subjects, only a single recording was obtained immediately following the injury.

3.3 Edema Quantification Protocol Results

In this chapter, the emphasis is on comparing the inter-subject and intra-subject variability for the two edema assessment methods mentioned in this paper – specifically, the method of Hersek et al. in which the injured side is compared against the contralateral side (E_j), and the novel differential measurement technique presented here (h_α) [26]:

$$E_j = \Delta R_{L-R,5\text{kHz}} \quad (18)$$

Moreover, the capability of the new methods to differentiate healthy controls from injured joints is checked by comparing their variance. The data collected were processed offline using Python. A 5-point FIR filter was applied to the resistance measured at 5 kHz and 100 kHz where h_α and E_j are calculated for all subjects. E_j is calculated by taking the difference in the resistance measured at 5 kHz between the left and right or right and left ankles while the subject is at resting position.

3.3.1 Intra-subject Variability

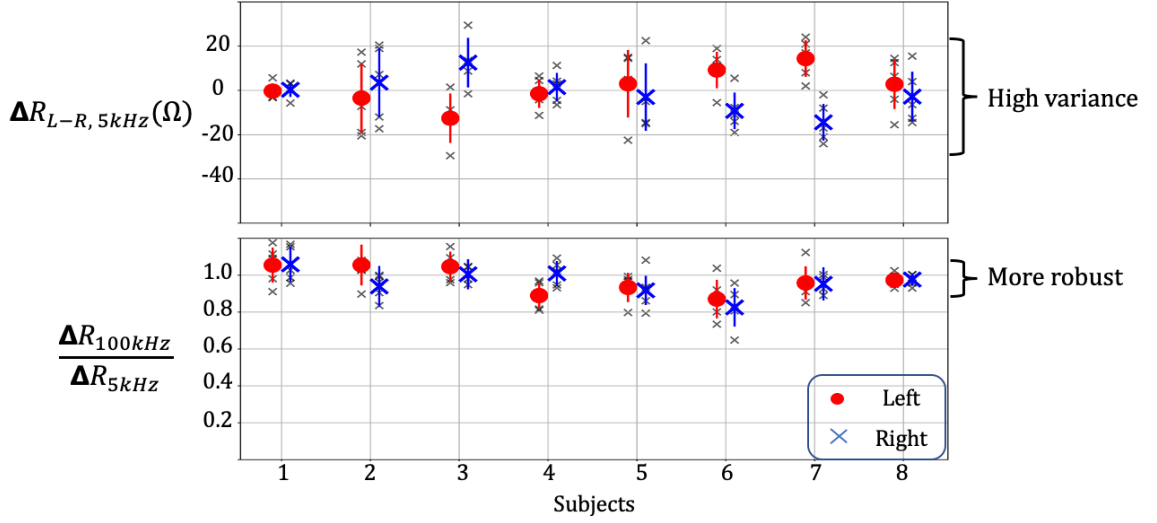


Figure 8. A Scatter plot shows the intra-subject variability of the two methods discussed in this paper for all control subjects over the length of the study. Note that E_j for the Right is the negative of E_j for the Left.

To quantify the ability of the different methods for tracking edema longitudinally, we focused on investigating intra-subject variability. Intra-subject variability is critical in determining longitudinal variation in the signal caused by day-to-day tasks performed by the subject, and thereby tracking edema longitudinally. Specifically, we compiled data from all control subject and plotted it in Figure 8 showing the variation in h_α and E_j over the duration of the study. For E_j and h_α we calculated the variance and standard deviation using Python. We calculated the variance of E_j and h_α for a randomly selected subject to be 68 and 0.008, respectively, and the standard deviation was 8 and 0.1 respectively. Moreover, since E_j was calculated while both ankles were in the resting position, we decided to inspect the effect of changing the ankle position on E_j by calculating the average change in resistance due to the subject changing their ankle position. This came out to be

10.5 Ω which is higher than the standard deviation for E_j demonstrating the ineffectiveness of E_j in tracking ankle joint edema if both ankles are not in the same position. Reflecting on those numbers, we observe a very small intra-subject variability for h_α compared to E_j . We also observe an h_α score that is close to 1.0 for both ankles, supporting our hypothesis about h_α for ankles with no recent record of injury.

3.3.2 *Inter-Subject Variability*

To assess the capability of the methods to detect edema in the ankle joint, we investigated their inter-subject variability for control and injured subjects. Inter-subject variability informs us about the method's accuracy in differentiating between the injured from the control subjects. The combined E_j and h_α from all subjects' data for the duration of the study is plotted in Figure 9. For control subjects, the variance for E_j and h_α is 237 and 0.01, respectively, and the standard deviation is 15 and 0.1 respectively. For injured subjects, the variance for E_j and h_α is 234 and 0.006, respectively, and the standard deviation is 16 and 0.08 respectively. The average of h_α for the control subjects was 0.955 compared to 0.5 for the injured subjects where the difference between those averages is 50 times larger than the variance of h_α . Also, note in Figure 9 the separation between the control and injured population for h_α and E_j where there is some overlap for E_j between the control and injured population compared to none for h_α .

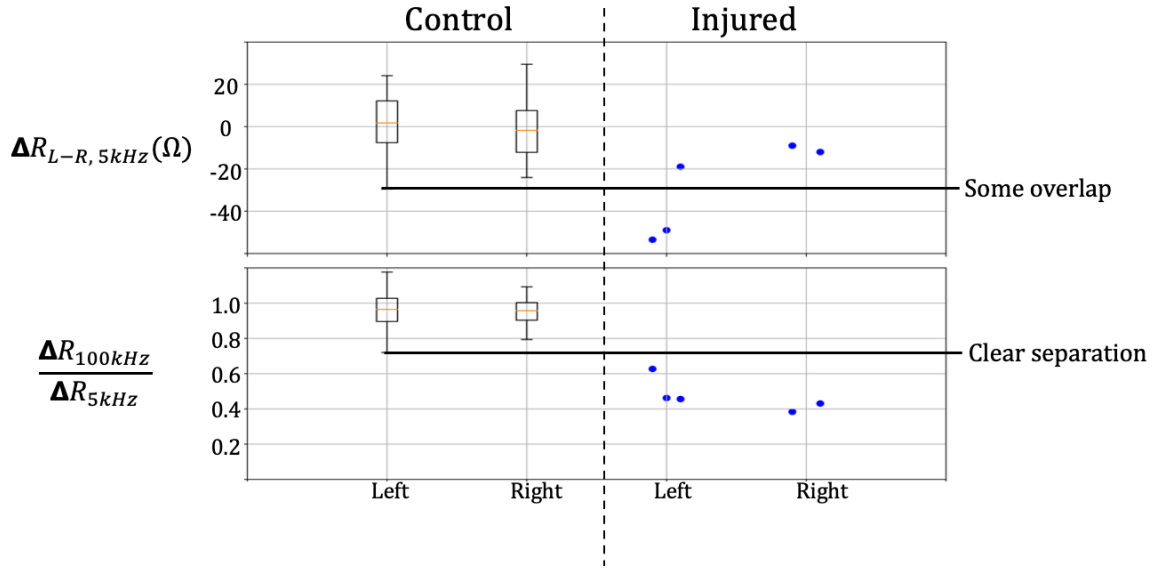


Figure 9. Box plot shows the inter-subject variability and the separation for the two methods discussed over the length of the study.

3.4 Cadaver Study

To further investigate the new method's capability to track changes in edema volume in the ankle joint, a study on four cadaver limbs was performed. After the limbs were fully thawed and pre-conditioned with 5 minutes of continuous motion through the full range of motion, the ankles were manually positioned into the same five postures in Figure 7(a) by a trained researcher. Figure 10 shows an example cadaver leg with the system placed and a syringe to inject saline into the ankle joint.

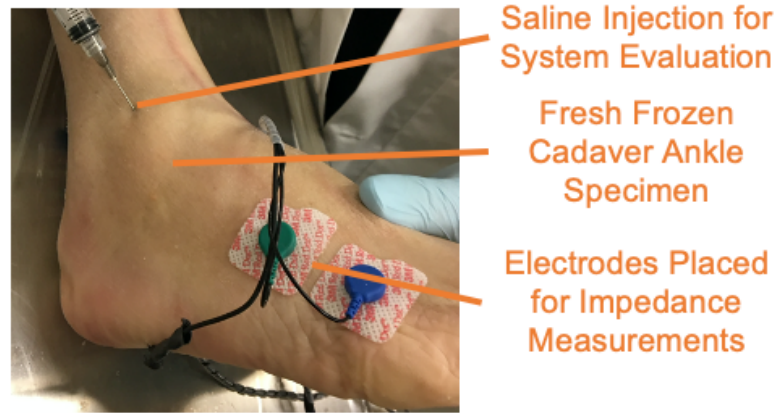


Figure 10. Cadaver leg with bioimpedance acquisition system electrodes placed distally and proximally to the ankle joint, and saline being injected to the joint.

The protocol in Figure 7(a) was repeated four times; each time 10mL of saline solution was injected into the lateral malleolus region. Data were collected from the cadaver model ankles at 0, 10, 20 and 30 mL of infused saline using the device presented. The volume of saline injected was chosen as mentioned for the following two reasons: (1) in literature, the volume of static liquid in a healthy ankle joint was found to be between 0.13 mL and 3.5 mL [62] and the volume of edema due to ankle sprain was found to be around 77mL [63, 64] and 82mL [65]. Hence, injecting saline solution into the ankle joint at 10 mL increments, shows great confidence in the resolution of the method proposed in this paper. (2) From our experiments, we were able to detect swelling visually at around 30 mL of saline infusion which increases the clinical significance of the device and method.

3.4.1 Cadaver Study Results

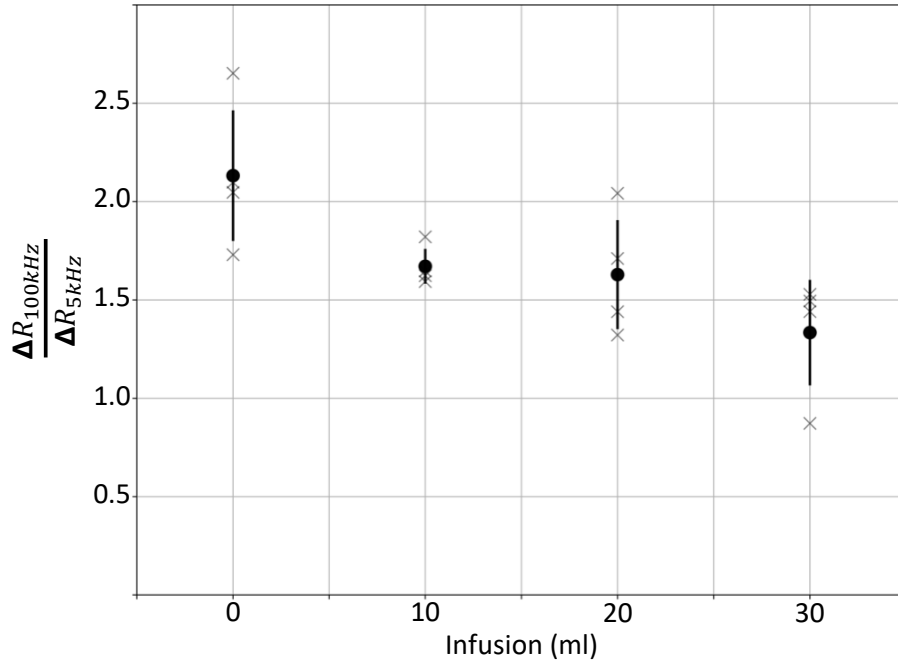


Figure 11. Cadaver model study results showing a reduction in the ratio of the change in high frequency resistance to low frequency resistance due to the ankle rotation with increasing the joint's static fluid content.

Due to the significant number of dead cells, and their inability to regenerate, utilizing the cadaver models resulted in a skew for baseline h_{α} . Figure 11 shows the reduction in the mean of h_{α} for the four cadaver models with increasing the saline injections simulating an increase in extracellular edema volume in the ankle joint. Statistical analysis is performed using repeated measures ANOVA with SPSS to check the method's ability in differentiating between the four different groups which would translate to the ability to detect changes in edema volume in the ankle joint. The data passed the sphericity test where the repeated measurement ANOVA p-value was 0.004. We also performed a Least Significant Difference (LSD) post hoc test and the pairwise comparison result showed an adjusted for multiple comparisons statistical significance between 0 and 20 mL saline infused of 0.004 possibly indicating a resolution of 20 mL. This supports the

proposed method's ability to not only detect extracellular edema in the ankle joint, but also track it, which is imperative for injury evaluation

3.5 Conclusion

In this chapter, a novel method to quantify and detect changes in ankle edema is presented. The method overcomes some of the limitations of the methods used in the literature by utilizing the effect of movement on the localized bioimpedance of the ankle joint instead of treating it as noise to the signal. The method also removes the need for normalizing the localized bioimpedance measurements to a healthy contralateral side or baseline measurement by comparing the effect of the joint movement on low and high frequency measurements. To validate this method, a study was performed on healthy control subjects with no recent record of injury and subjects with recent ankle injuries (within 2 days). The method's intra-subject and inter-subject variability was compared to traditional BIA based methods for edema detection, where it showed high accuracy in detecting and quantifying extracellular edema in the ankle joint with low day to day variability. This approach could allow patients to track their ankle swelling at home by performing a simple protocol, rather than having to perform multiple measurements of both ankle joints using two systems.

CHAPTER 4. TRANSLATION OF EDEMA QUANTIFICATION METHODS TO A WEARABLE SETTING

4.1 Introduction

In Chapter 3, methods to overcome some of the limitations of SFBIA are presented, where a BIA method for quantifying joint edema based on positional changes of the ankle joint is developed. This technique compares the effects that changes in ankle position have on the range of the resistance measured at 5 kHz against the range of the resistance measured at 100 kHz. Changes in ankle position alter the distribution of extracellular fluid within the joint cavity which affects extracellular resistance (R_e from the Fricke-Morse model) - the primary path for low-frequency currents. This method was validated in a human cadaver model (where it demonstrated 10-mL resolution) and on a cohort of human subjects. In Chapter 3, the 5kHz signal was compared against the 100 kHz signal, which made the need for a healthy contralateral comparison to normalize the findings unnecessary and reduced the dependency of signal quality on electrode placement. This mitigated several of the limitations of BIA technologies and presented a wearable form-factor for these sensors. However, that technique still required patients to perform a specific set of movements, could only detect ankle swelling (not structural defects), and could not be recorded during ambulation – all of which limit the capabilities of this system for providing the level of quantitative feedback necessary to best aid in a patient’s rehabilitation.

In this chapter, several key changes to our technology are made to address these limitations. Specifically, in this new implementation of the wearable BIA monitoring

system, hardware and firmware adjustments enable accurate measurement of the ankle joint's bioimpedance and position for robust tracking of changes in the joint's edema *during ambulation*. We also quantify the relationship between our bioimpedance measurements measured during human subjects' activities of daily living and the structure of the underlying collagen fibers using a software simulation model. By demonstrating such a relationship, this work suggests that wearable BIA measurements can provide quantitative, clinically relevant information related to a patient's injury recovery status. Such feedback will enable more personalized and optimized rehabilitative efforts, whether during initial / follow-up visits to the clinic or while the patient simply engages in their normal, everyday activities. This type of longitudinal, rapid feedback could alert a patient to when they are approaching a threshold of reinjury real-time during activity when they are most prone to injury, providing the opportunity to readjust their rehabilitative efforts and prevent repeat clinical visits.

4.2 Signal Analysis

The Fricke-Morse circuit model has three components— R_e , R_i , and C_x —which together describe the bioimpedance of tissue. Estimating these values requires impedance measurements at multiple frequencies and a non-linear least squares-based algorithm. Substantial measurement time and computational power are required – both of which are unfavorable for implementation of BIA in a wearable system designed to provide real-time feedback to the user. To circumvent the requirements presented in the Fricke-Morse model estimation, we devised a simple and robust method for assessing the underlying biological phenomenon within the ankle. The method presented in this chapter compares the changes

in the reactance at two distinct frequencies recorded while the subject performs a task that stresses the joint.

4.2.1 *The Reactance of the Tissue*

Researchers have studied the effect of muscular injuries on bioimpedance at the tissue and muscle fiber level. At the tissue level, Nescolarde et al. determined that longitudinal changes in reactance – measured at 50 kHz - is an optimal metric for representing muscle tissue status since it is associated with cell density and soft tissue integrity [3]. At the muscle fiber level, Sanchez et al. researched the effect of myotonic dystrophy on the Fricke-Morse circuit components using a mouse model [66, 67]. They attributed the changes in capacitance (C_x) to cell membrane integrity, and intracellular resistance (R_i) to cell inflammation. In the case of injured muscle fibers, they observed a decrease in R_e (~30%) and C_x (~40%) and an increase in R_i (~35%). On the cellular level, Dodde et al. analyzed the effects of applying pressure to porcine cells of the spleen on the Fricke-Morse circuit components [68]. They concluded that applying forces up to 50% of the cell membrane's strength led to a non-significant increase in R_e and R_i and decrease in C_x . However, beyond the cell membrane's strength (i.e. >50%) the cell ruptures, and there is a significant decrease in R_e and a significant increase R_i and C_x due to the migration of intracellular fluids to the extracellular space. Building upon this previous research, we have used the Fricke-Morse circuit model to *simulate the effects of edema, collagen fiber tears and blood flow on the reactance of the tissue*. The model uses resistive and capacitive values for the Fricke-Morse circuit components in the ankle joint's impedance space from the literature and Chapter 3 as a baseline [46, 69].

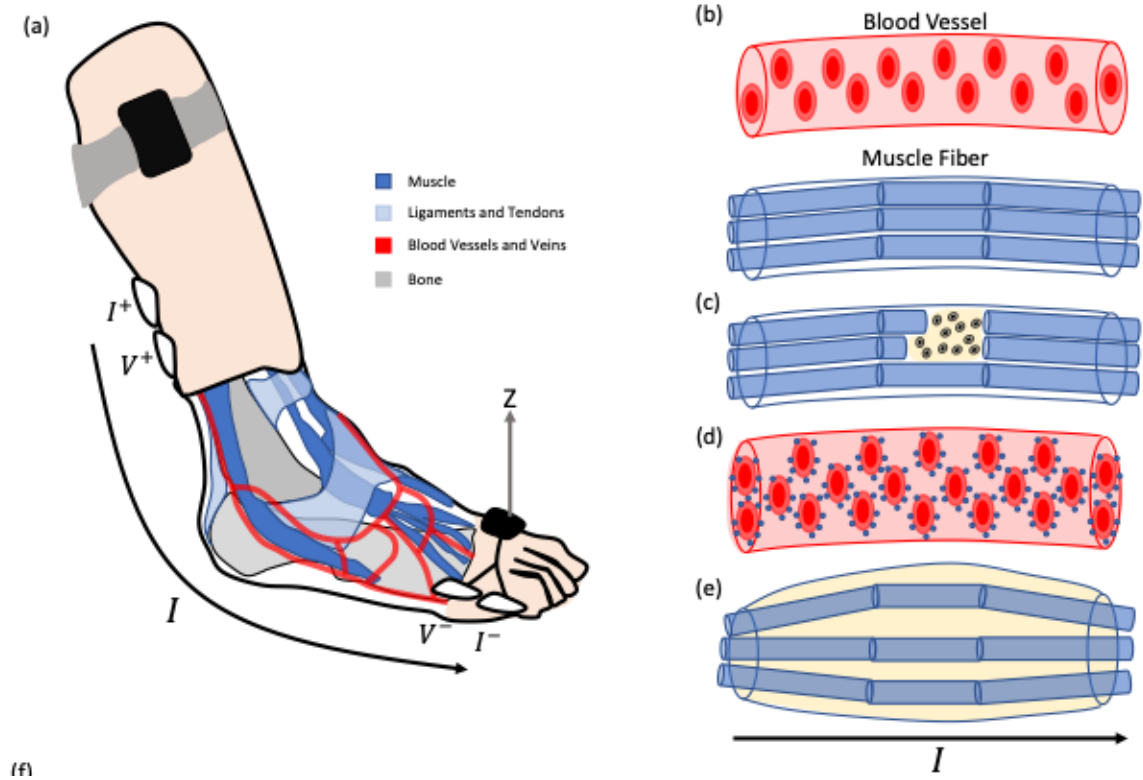


Figure 12. The anatomy of the ankle joint showing lack of fatty tissue or static fluid. (b) A sample blood vessel and muscle fiber which are the primary path for the current applied to measure the bioimpedance. (c) A muscle fiber tear, showing the migration of intracellular fluids to the extracellular space surrounding. (d) An increase in the red blood cell count and glucose due to sustained muscle activity. (e) An increase in edema due to muscle inflammation.

4.3 Simulation Model

To study the effect of edema, collagen fiber tear and blood flow on the localized reactance of the ankle at 5 kHz and 100 kHz, we devised a numerical analysis simulation model. The model utilizes the following equation to calculate the impedance of the Fricke-Morse model at a specific frequency (ω).

$$R + jX = \frac{R_e(R_i + \frac{1}{j\omega C_x})}{R_e + R_i + \frac{1}{j\omega C_x}} \quad (19)$$

The simulation model outputs the ratio of the changes in the reactance at 5 kHz and 100 kHz due to changes in the Fricke-Morse components from baseline. The baseline impedances used are the bioimpedance spectroscopy data collected from our previous study in Chapter 3.

4.3.1 Fricke-Morse Model Estimation

In this section the algorithm used to calculate the values of the Fricke-Morse components used as baseline in our simulation model is presented. From the study performed in Chapter 3, bioimpedance spectroscopy data were collected over the frequency range of 5 kHz to 100 kHz with a resolution of 371 Hz for a total of 256 bioimpedance measurements per sweep. Using Python, we created a function that calculates real component the Fricke-Morse impedance for specific R_e , R_i and C_x values at the same frequencies from our bioimpedance spectroscopy data using the equation in (19) [70]. Figure 13 shows an example bioimpedance spectroscopy of a healthy ankle joint and the estimated Fricke-Morse impedance using our algorithm. Table 5 shows the Fricke-Morse component values for 14 healthy ankles. The bioimpedance values presented are similar to the values reported by King et al. [69]

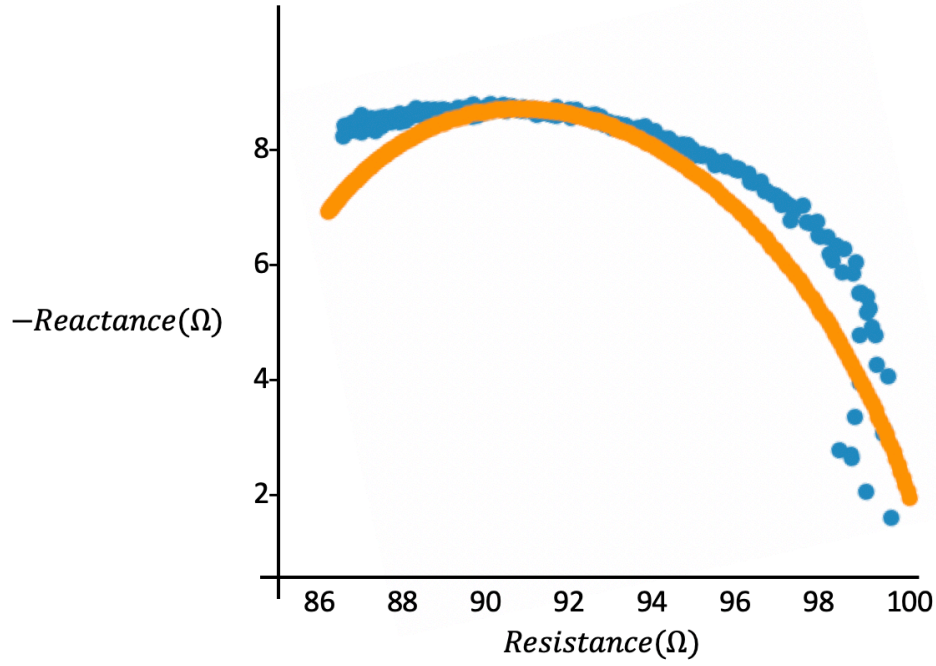


Figure 13. An example of localized bioimpedance spectroscopy data and its associated Frick-Morse estimated parameters when using non-linear least squares estimation to find the optimal 2R1C values that fit the measured data.

Table 5. Estimated Fricke-Morse circuit component values of 14 ankles with no recent record of injury.

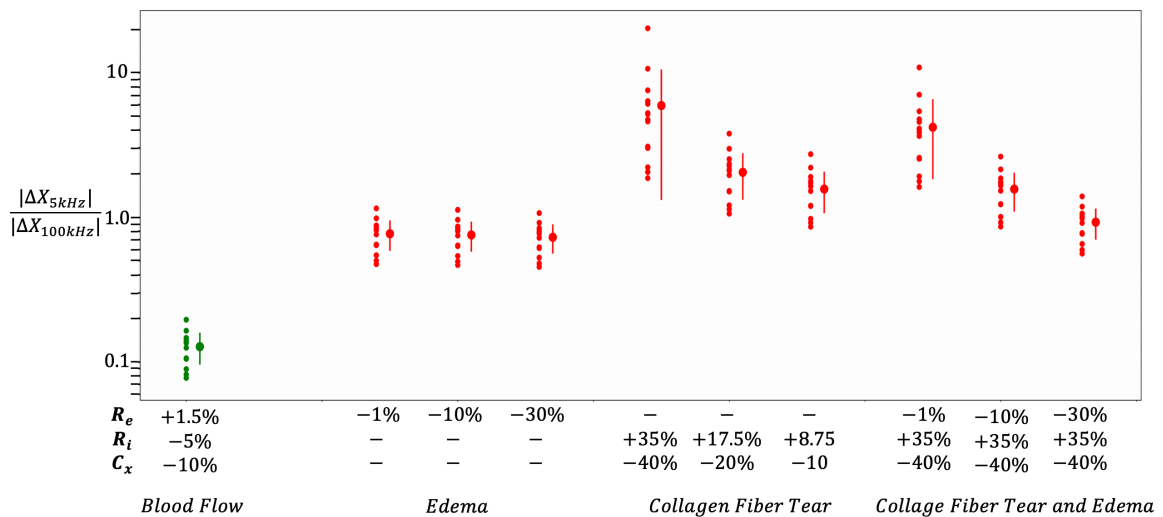
$R_e(\Omega)$	$R_i(\Omega)$	C_x (nF)
102	520	9.6
107	633	8
160	940	5.4
163	1178	3.3
115	543	9.2
108	770	5.2
113	877	5.4
152	676	7.7
127	746	6.5
100	869	5
128	1022	5.5
108	765	6
137	577	10
101	511	9.6

4.3.2 *The Ratio of $X_{5\text{ kHz}}$ to $X_{100\text{ kHz}}$*

Using that model, two frequencies of electrical current are used to measure BIA. As mentioned earlier, the low-frequency, 5 kHz current will primarily travel through the extracellular space since it is unable to pass through cellular membranes, and the high-frequency, 100 kHz current will take a more direct path using both intracellular and extracellular pathways. When these currents are applied to the ankle, they primarily flow through muscle fibers and blood vessels since the bones have low conductance and there is minimal fatty tissue and static extracellular fluid [63, 71]. Section 4.2.1 presented key parameters for modeling current flow. Using that research, we can simulate the effects of blood flow, edema, and collagen fiber tears on the reactance of the ankle joint. In a normal physiologic state during sustained activity, blood flow to the region increases to meet the increasing metabolic demand of the muscles (Figure 12d). When the ankle is sprained, collagen fibers may tear and edema increases (as depicted in Figure 12c and 12e, respectively).

In an uninjured state, when blood flow is augmented during sustained activity, the increased number of red blood cells increases the number of intracellular pathways for current to travel through, which then decreases R_i . This change also increases the extracellular resistance and decreases the tissue capacitance, as reported by Abdelbaset et al. [72]. In another study by Gheorge et al., they reported the effect of changes in blood viscosity on the Fricke-Morse to be around 1.5% in R_e , 5% in R_i and 10% in C_x [70].

In an injured state, tenocytes tear, and concomitant collagen fibers rupture, spilling intracellular contents into the extracellular space. This decreases R_e (since there is now more extracellular fluid) and increases R_i (since there are fewer pathways through intact cells). Sanchez et al. demonstrated that intact myocyte membranes maintain the system's capacitance, therefore torn muscle fibers will also lead to a drop in C_x [66]. With injury there will also be an increase in extracellular edema, which further decreases R_e since there is an increased volume of the conductive extracellular fluid. In their study, they reported a 30% decrease in R_e , 35% increase in R_i and a 40% decrease in C_x 24 hours after the injury.



In Figure 14, we present the results of our simulation of BIA in the ankle. When comparing the ratio of change in reactance at 5 kHz and at 100 kHz we found a significant difference between healthy and injured ankles as shown in Figure 14. This result is

consistent with our expectations based on the impact of the described pathophysiologic changes during activity and injury, and with the earlier findings of Freeborn et al. in their study on the effects of biceps muscle fatigue on bioimpedance spectroscopy [61, 73]. The findings of this simulation encourage further research and hardware development into the BIA phenomenon and its clinical uses.

4.4 Blood Flow vs Edema vs Muscle Tear

After the acute phase of an injury, the tissues enter a phase of rebuilding which includes a reduction in edema and increasing collagen fiber strength. The level of edema and strength of the reforming fiber are indicative of the progress of the rehabilitation and the probability of reinjury [74]. In Figure 14, the ratio of the change in the reactance at 5 kHz versus at 100 kHz successfully differentiates healthy from injured ankles, but differentiating swelling from collagen fiber strength is a different challenge. In Chapter 3, the effect that changes in ankle position have on low (5 kHz) and high-frequency (100 kHz) resistance measurements was studied. It was shown that these positional changes move the extracellular fluids around the joint altering the extracellular resistance (R_e) which in turn predominantly impacts the low-frequency resistance (extracellular fluid dependent) compared to the high-frequency resistance [46]. Although, in this chapter the changes in the reactance, instead of resistance, at low and high frequency is utilized for the analysis, the concept of extracellular fluids shifting in the tissue due to the pressure from the joint structure caused by its rotation.

In this chapter, the bioimpedance of the ankle joint while subjects are walking is measured using our wearable sensing hardware. Normally, the instantaneous changes

observed in the ankle's bioimpedance during a *subject's gait cycle* are possibly due to the tendons and ligaments, and varying blood flow in the current path. However, if there exists edematous extracellular fluid, the pressure from the joint structure would shift the fluid around it changing the extracellular resistance (R_e) in the current path. we hypothesize that in the presence of joint edema, there will be an increase in the instantaneous change per step in the low frequency reactance measurements compared to the lower frequency measurements as shown in Figure 14. Nevertheless, these positional changes should not compound throughout the duration of a walking session. Rather, we hypothesize that the baseline changes in bioimpedance from the beginning of a walking session are mainly due to micro-damage to any recently injured tendons, ligaments, and tissue coupled with low-level edema. To test these hypotheses, we developed two metrics for comparing the range of the reactance at 5 kHz to the range of the reactance at 100 kHz: (1) per step (\hat{h}_α), and (2) per walking session (>200 steps) (β).

4.5 Algorithm

To compute \hat{h}_α and β , it is necessary to split the reactance measured at the two frequencies based on each subjects' steps as shown in Figure 15. This windowing uses the inertial measurement unit (IMU) employed on our custom hardware. The IMU captures the angular velocity of the foot, which is used to determine if the subject is moving. This is performed by taking 3-second windows of the angular velocity and convolving those values on themselves to compute the energy of that window's angular velocity ($\omega[t]$) as shown in the following equation.

$$E_{\omega}[t] = \sum_{t=n}^{n+3} |\omega[t]|^2 \text{ (rad/s}^2\text{)} \quad (20)$$

That energy is compared against an experimentally determined threshold of 10,000. If the energy is higher than that threshold, the peaks of the Z-axis (lateral) acceleration signal from the IMU are used to identify the heel-strikes which mark the beginning of each step as shown in Figure 15c. Each peak needs to be at least 350 ms from the previous peak and beyond a certain threshold (1 g) to remove errors from irregularities in the signal. Since the bioimpedance is sampled at a lower frequency than the IMU, the start and end of each step's bioimpedance window is identified by finding the absolute minimum time difference between the time of the heel strike and the time of the bioimpedance measurements. These data are then used in the model presented in Figure 15c.

After splitting the reactance measured to per step arrays as shown in Figure 15d, the range and mean of each step's reactance is calculated. \hat{h}_{α} is calculated by taking the ratio of the range per step of the reactance at 5 kHz to the range per step of the reactance at 100 kHz. To calculate β at any step (s), the range of the mean of the reactance per step from the start of the walking session to step s is calculated. The ratio of this range at 5 kHz to 100 kHz is then taken to calculate β as shown in Figure 15d.

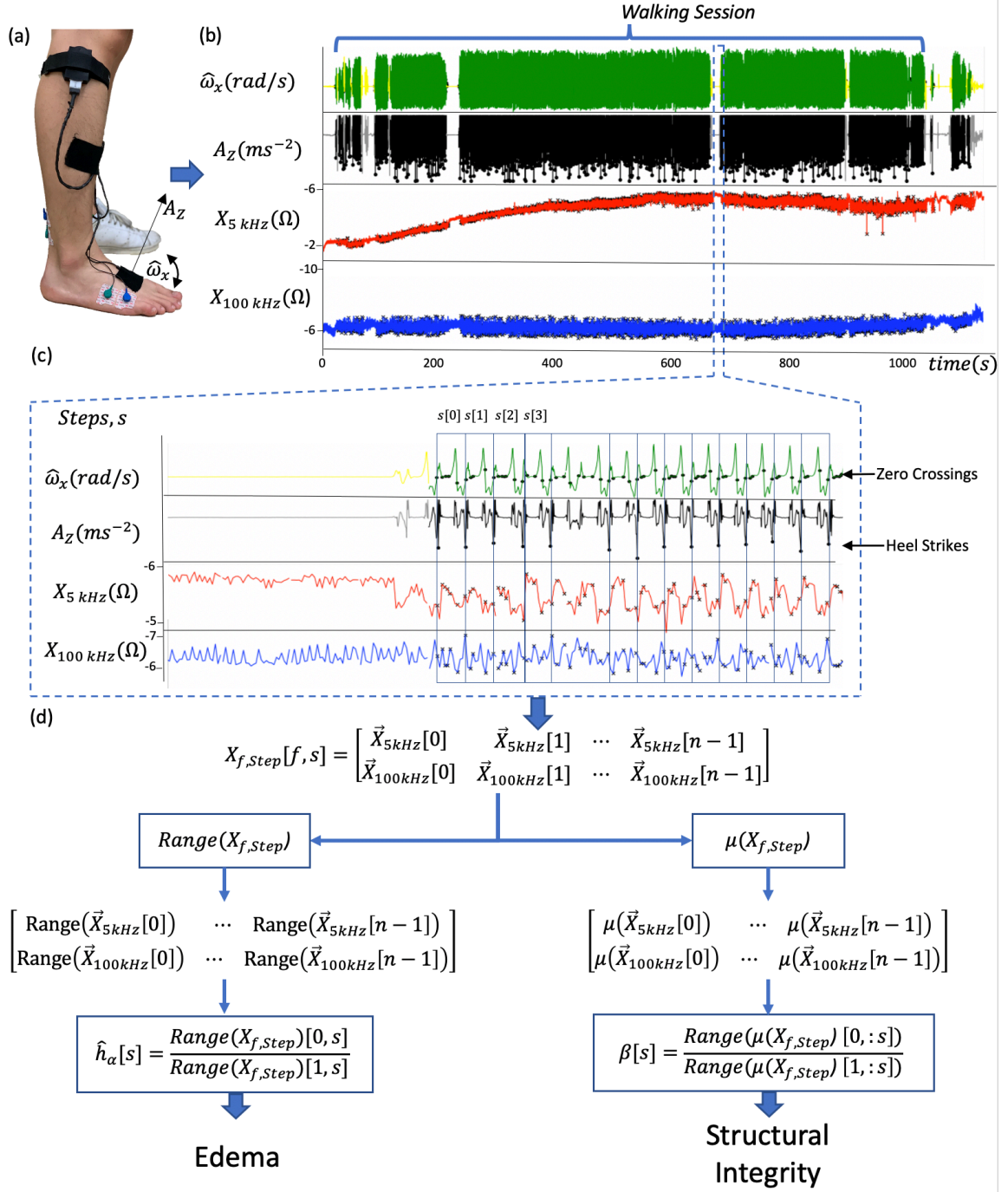


Figure 15. Data Analysis Workflow for Determining Presence of Edema and disruption to Structural Integrity of the Ankle. (a) The data acquisition system placed on the subject's leg with the necessary current and voltage electrodes placed distally and proximally to the ankle joint and the IMU placed on the foot. (b) Sample data of a representative injured subject's X-axis angular velocity, Z-axis acceleration, and reactance measured at 5 kHz and 100 kHz. (c) A magnified view of the sample data showing how the data windows are created and used in splitting to split the reactance data into vectors per step. (d) The

reactance vectors per step are used in the model to detect edema and collagen fiber tear in the ankle joint.

4.6 Data Collection Protocol for Method's Evaluation

To validate our hypothesis that \hat{h}_α can detect edema in the ankle, we recorded data from 15 subjects during ambulation and asked them to perform the BIA ankle positional protocol as described in Chapter 3 and depicted in Figure 16 once per hour. The data collection protocol was approved by the Georgia Institute of Technology Institutional Review Board, and all subjects provided written informed consent before participating in the study. This positional protocol was previously shown to correlate with edema in Chapter 3. In this study, we sought to determine if \hat{h}_α measured during walking also correlated with edema. We also sought to test if β (the difference in impedance after a continuous walking session) can differentiate between healthy and injured populations. Figure 16 depicts the overall testing protocol. The modified system is placed on the subject's ankle as shown in Figure 16a. Red dot gel electrodes (3M, Saint Paul, MN) are used for bioimpedance measurements. The electrode snaps and IMU are secured using Kinesio tape (Kinesio, Albuquerque, NM) to further secure them and dampen the forces from movement. With the recording setup in place, the subjects performed the 5-minute positional protocol shown in Figure 16c. The subjects then perform their normal daily activities while performing the 5-minute positional protocol every hour as depicted in Figure 16b.

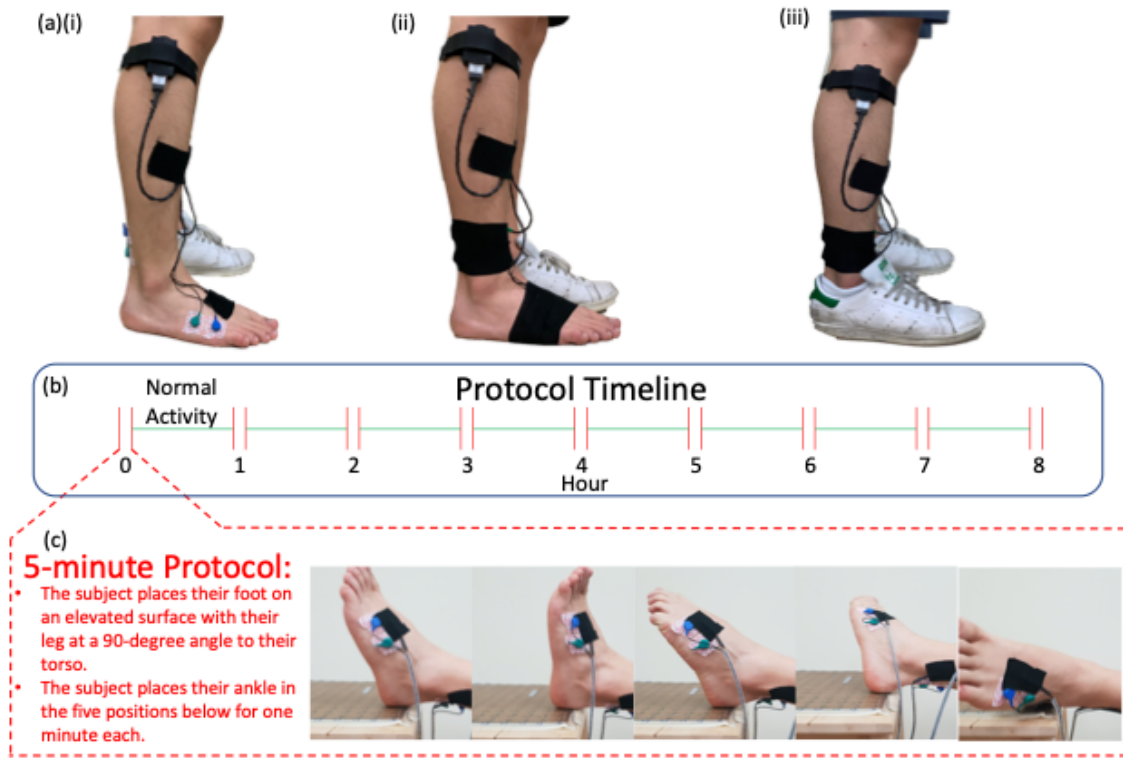


Figure 16 . Recording setup and 8-hour recording protocol timeline. (a) The wearable data acquisition is placed on the subject's leg. (b) The overall recording protocol took 8 hours with the 5-minute positional protocol as depicted in (c) being performed every hour.

The participants were recruited via word of mouth by either the engineering research staff or the Georgia Institute of Technology athletic trainer of the study team. The sensors were outfitted in the lab or the athletic center in the early morning to reduce any residual effect from prior movement on the data. The subjects were then instructed to go about their daily activities for eight hours. After the eight hours of data collection, the subjects returned to the lab or the athletic center for the device to be removed.

The study was performed on 15 subjects between the ages of 18 and 30. Of these subjects, 7 had an ankle injury in the two to four weeks prior to data collection. Data from the contralateral healthy ankle were also collected from 3 of the 7 injured subjects on a

separate day. On the remaining 8 healthy subjects, data were collected from their dominant ankle due to its higher chance of injury [49]. In total, 11 healthy ankles and 7 injured ankles were recorded. Four of the injured ankles were diagnosed by a medical professional and the rest were self-reported. The injuries were grades 1-2 lateral ankle sprains. The data were analyzed offline using Python.

4.7 Statistical Analysis

To test the ability of the methods presented to separate between healthy and injured groups, we first tested the data for normality using Wilk-Shapiro test. Since one of the data groups (healthy \hat{h}_α) failed the normality test, we used Wilcoxon rank-sum test where a p -value less than 0.05 is considered significant. For each score (\hat{h}_α and β), Cohen's (d) effect size between the healthy and injured group was also calculated where an effective size higher than 1.4 is considered large effect [75]. An example of the variables extracted from the model in Figure 15 is presented in Figure 17. We also used Pearson correlation tests to show the correlation of \hat{h}_α to the static protocol.

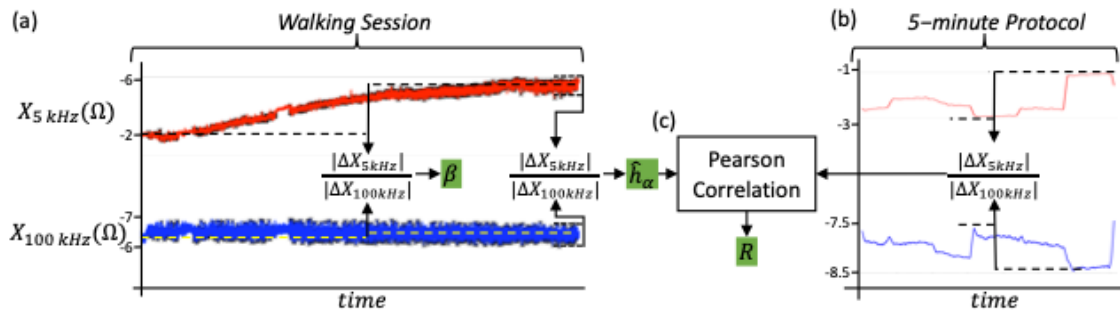


Figure 17. Method for Comparing the Full Walking Session to 5-Minute protocol. (a) The range of change in the reactance measured at 5 kHz and 100 kHz during a continuous walking session is used to calculate β . (b) The range of the change in the reactance measured at 5 kHz and 100 kHz per step is used to calculate \hat{h}_α . (c) The mean \hat{h}_α of the

last 10 steps is correlated to the ratio of the range of change in the reactance measured at 5 kHz and 100 kHz using Pearson's correlation.

4.8 Results

4.8.1 *Ratio of the Ranges of Reactance Per Step (\hat{h}_α)*

To test our hypothesis that \hat{h}_α is sensitive to detecting edema, we correlated the ratio of the range of the reactance at 5 kHz to the range at 100 kHz from Figure 16a against those values found during the 5-minute, static positional protocol from Figure 16b as shown in Figure 17c. To ensure that no residual edema or muscle tear from prior walking sessions skewed the result, data from the first substantial continuous walking session were used. In this context, a “substantial” session is considered one in which the subject walks for more than 200 steps with a maximum of pause of 1 minute between successive steps. For all 15 subjects, the mean of \hat{h}_α was calculated from the last 10 steps of the first walking session and tested for correlation with the 5-minute positional protocol performed immediately after that session for all 15 subjects as shown in Figure 17c. This comparison yielded a Pearson's correlation coefficient of 0.8 as shown in Figure 18.

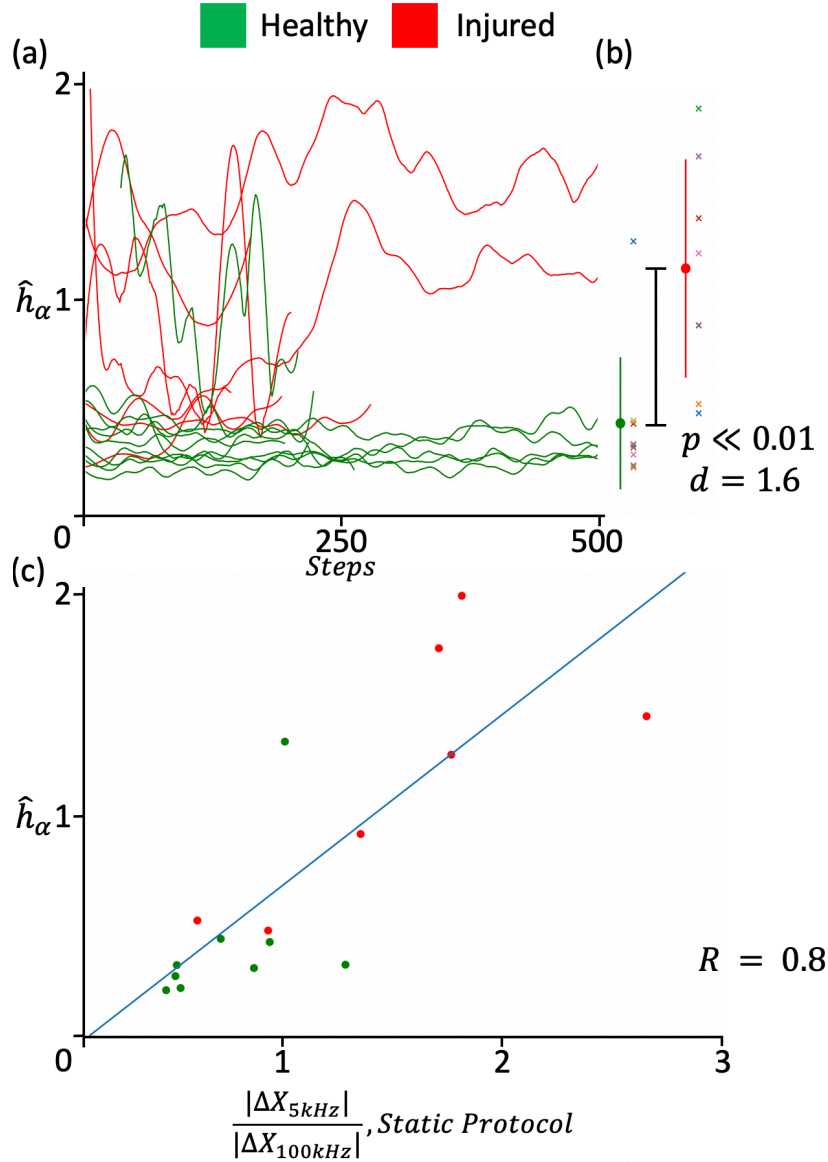


Figure 18. (a) Plot showing \hat{h}_α vs steps for all subjects and (b) a scatter plot of the mean of \hat{h}_α for the last ten steps for the healthy and injured groups showing a statistically significant p-value. (c) Plot of the mean \hat{h}_α at the last ten steps in a continuous walking session, correlated the output of the 5-minute protocol done after with a Pearson correlation coefficient of 0.8.

This supports our hypothesis that \hat{h}_α is sensitive to edema, since the positional protocol was previously shown to correlate with edema levels as shown in Chapter 3. The results of \hat{h}_α and the ratio of the range of X_{5kHz} to X_{100kHz} from the static protocol for the

injured and healthy group are presented in Figures 18 (a, b, c) and tested for statistical significance ($p = 0.0021$) and Cohen's effect size of 1.6. This indicates the method's ability to differentiate between healthy and injured ankles. There is also similarity between the injured and healthy population \hat{h}_α scores in Figure 18b and the results of the simulation model for changes in edema and blood flow from Figure 14.

4.8.2 Beta Walking Results

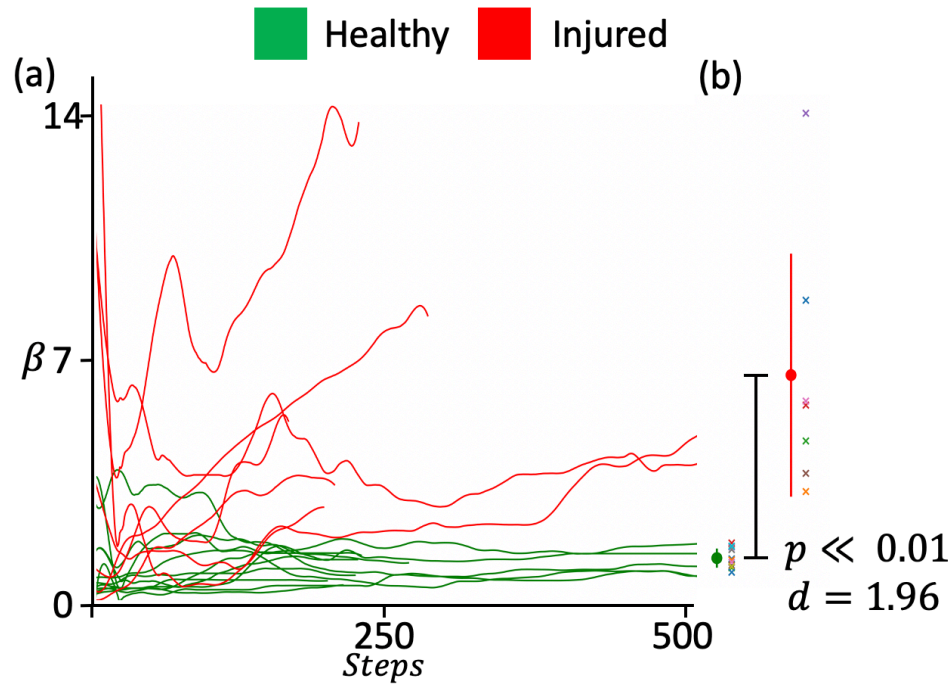


Figure 19. (a) Plot showing β vs steps for all subjects and (b) a scatter plot of the β at the last step of a continuous walking session showing a statistically significant p-value.

While the step-by-step analysis demonstrated that BIA at these two frequencies could detect edema, it provided little information about the integrity of the tissue. During a substantial period of walking, micro-tears are expected to occur in the ligaments, tendons, and connective tissue [76]. To better understand the impact that this degradation of tissue

integrity has on the reactance measured using BIA, we calculated the range of reactance recording during a continuous walking period as shown in Figure 17a. Significant differences in this range between the injured and healthy groups when taking the β from the last step of the continuous walking session was found ($p < 0.001$) and Cohen's d effect size of 1.96 as shown in Figure 19. To control for inter-subject inter-session variability (particularly in the number of steps per walking session), the β is also calculated at the 200th step of the first substantial walking session for all subjects and a significant difference between the injured and the healthy groups was found ($p < 0.01$). There is also similarity between the β scores for the healthy and injured population shown in Figure 19e and results of the simulation model for collagen fiber tear and blood flow from Figure 14.

4.8.3 Zero Crossings Data Analysis

During the typical gait cycle, the ankle's direction of rotation changes (thus, its angular velocity = 0) four times: (1) at a neutral position (i.e., with the foot and shank at or near 90° to each other) just prior to heel-strike, (2) in a slightly plantarflexed state once the foot is flat on the ground just after heel-strike, (3) in a dorsiflexed state just prior to heel-rise, and (4) in a plantarflexed state just prior to toe-off leading into swing phase. These same joint configurations are performed in the static positional protocol, providing points of comparison between the dynamic (walking) and static (positional) tasks [46]. The software model presented was tested using only the data closest to the zero crossings by choosing the bioimpedance measurements that had the absolute minimum time difference from the time of the zero-crossings. For the \hat{h}_α calculated using the zero crossings data, the Spearman's correlation coefficient with the ratio of the range of reactance at 5 kHz to the

range of reactance at 100 kHz from the 5-minute protocol is 0.63. The calculated p-value is $p < 0.01$ for the separation between the healthy and injury group. The difference in the correlation score using all bioimpedance measurements (as presented in Section 4.8.1) and the measurements closest to the zero crossings may be due to the relatively low sampling rate of the bioimpedance or due to a delayed response for the impedance from the changes in the ankle position caused by the loading of the joint at these positions. In some cases, the nearest bioimpedance measurement to the zero crossing was up to 50 ms away. For the β score using the data closest to the zero crossings, the p-value is < 0.01 .

Using only the data at the angular velocity's zero crossing would enable significant reduction in the bioimpedance samples needed and hence the power consumption, as the bioimpedance can be measured only at the zero-crossings using an interrupt-based approach. This would allow the software model to be fully implemented on an embedded processor in a wearable-form factor.

4.9 Conclusion

The work presented in this chapter provides a robust method for capturing and analyzing bioimpedance measurements from the ankle. Previous work in this field typically prescribed a set of controlled exercises to ensure accurate measurements. In this chapter, a solution is designed to adapt this technology into a wearable form factor that *leverages* the impact of ambulation on the signals rather than mitigating it. Additionally, this novel method of signal interpretation requires minimal algorithmic and computational complexity making it suitable for being embedded into a miniaturized, wearable system. The results of this algorithm are presented in Section 4.8 and demonstrate that this

technique is capable of real-time detection of edema and tissue integrity changes in the ankle during activities of daily living. This usability improvement and enhanced algorithm enables real-time joint health status updates for the wearer. These notifications, if properly utilized, could greatly aid in personalizing clinical rehabilitation efforts.

CHAPTER 5. METHODS AND ALGORITHMS FOR IV INFILTRATION DETECTION

5.1 Introduction

Intravenous (IV) treatment is the delivery of non-vesicant fluid or medication directly to the blood by placing a catheter into a peripheral vein for fluid infusion [77]. One possible complication of IV treatment is IV infiltration, or extravasation: the leakage of the infused fluid to the surrounding perivascular or subcutaneous tissue due to the dislodgment of the catheter from the vein as a result of patient movement, weakening of the venous walls or initial misplacement [78]. It is estimated that 85% of hospitalized patients in the US receive at least one IV treatment with a 50% chance of failure and a 23% chance of an infiltration, making it one of the highest occurring in-hospital medical emergencies[79]. IV infiltration is evaluated on a 1-4 scale based on the amount of static infused fluid (edema), and its effect on the tissue (skin temperature and stretch) [78, 80]. Depending on the severity, it can lead to local edema, discomfort, pain, ischemia, tissue necrosis, and in extreme cases can lead to scarring, disfigurement and loss of limb [81]. These extreme cases are more prevalent in pediatric patient populations: children may move the limb with the IV more than adults, may have weaker or thinner venous walls, and have a difficulty communicating pain to caregivers in time for the issue to be addressed [82].

IV infiltration events are medical emergencies: early detection minimizes the volume of fluid in the extravascular space and thereby precludes irreversible damage to the tissue. Currently, the standard of care in hospitals for detecting infiltration requires

caregivers to employ a “look, feel, and compare” protocol [83, 84]: every hour, caregivers manually check the IV site by visually examining and feeling it for any swelling, then comparing it to the contralateral side. This requires having access to the IV site and the contralateral side to compare against, which is not guaranteed in the operating room when patients are covered in drapes and may also be challenging when healthcare resources and time are already strained (e.g., during the current pandemic). Most importantly, the method is qualitative and subjective, relying on the caregiver’s expertise, and is done at most once per hour at best, which can be insufficient for a time sensitive emergency such as IV infiltration. Non-invasive technologies capable of continuously and accurately tracking extravascular fluid volume at the IV site can assist caregivers to detect infiltration events as early as possible. Existing technologies in the market to automate the detection of IV infiltration use optical sensing by emitting light onto the IV site and measuring the changes in the reflected light[85]. However, the technology is limited to detecting clear fluids and requires tethering the patient with an optical cable limiting their movement and taking valuable space on the IV pole.

Wearable detection of IV infiltration fundamentally hinges on non-invasively sensing the volume of fluid inside of the limb with sensors placed cutaneously. A promising technology for sensing fluid content in biological tissue volumes is BIA, a non-invasive measure of the tissue’s electrical conductivity. Bioimpedance has the potential for detecting IV infiltration due to its sensitivity to changes in the measured tissue composition, especially with the substantial difference in conductivity between fluids and body tissue [27]. Bioimpedance is measured by applying a safe, small, alternating current to the tissue through distally placed electrodes and measuring the voltage drop through

proximally placed electrodes. As the current travels through the tissue's extracellular and intracellular fluid space, an increase in the static fluid content in the current's path would provide more extracellular path, assisting the current's flow in the tissue therefore reducing the impedance. In the literature, BIA has been investigated as a method for the detection of IV infiltration in controlled settings on animal models and human subjects: such literature demonstrated that bioimpedance can accurately detect infiltrates with volume as low as 10 mL [86-88].

5.2 Porcine Model Study

5.2.1 Protocol

In collaboration with T3 labs, trained veterinarians sedated a pig and placed an IV catheter subcutaneously to simulate normal drug delivery to the blood stream and an infusion to show their effect on local bioimpedance measurements. Using the system presented in Chapter 2, electrodes were placed proximally and distally to the IV site as shown in Figure 20. This protocol was approved by the Institutional Animal Care and Use Committee at Georgia Tech and T3 Labs (Global Center for Medical Innovation [GCMI], Atlanta, GA). First, saline solution is administered to the blood stream simulating drug delivery in the absence of an infiltration by infusing 2, 5, 10 and 10 mL. Then, the IV catheter is manually dislodged, and the saline solution is infused to the surrounding tissue simulating an IV infiltration.

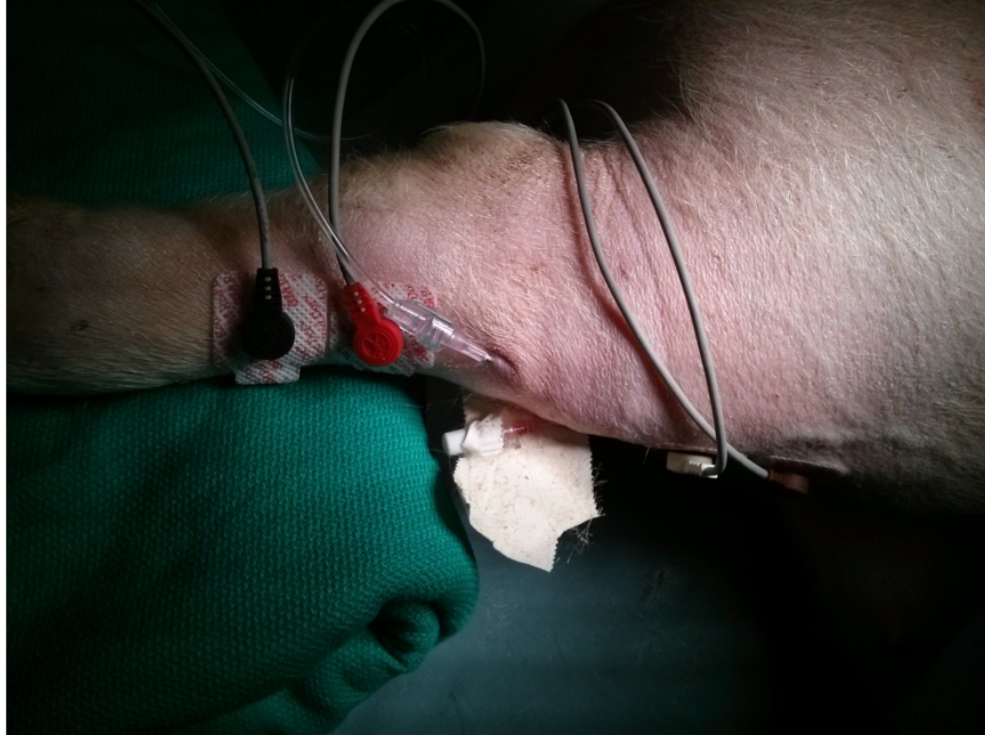


Figure 20. IV catheter placed subcutaneously with the current and voltage electrodes placed proximally and distally to the IV site.

5.2.2 Results

When administering saline solution to the blood stream, there is a minimal change in the measured bioimpedance of the IV site at all frequencies as shown in Figure 21 (top). However, when displacing the IV catheter simulating an infusion, the localized bioimpedance of IV site drops substantially. Since fluid is more conductive than biological tissue, static fluid provides a conductive path to the current, hence reducing the measured impedance of the tissue.

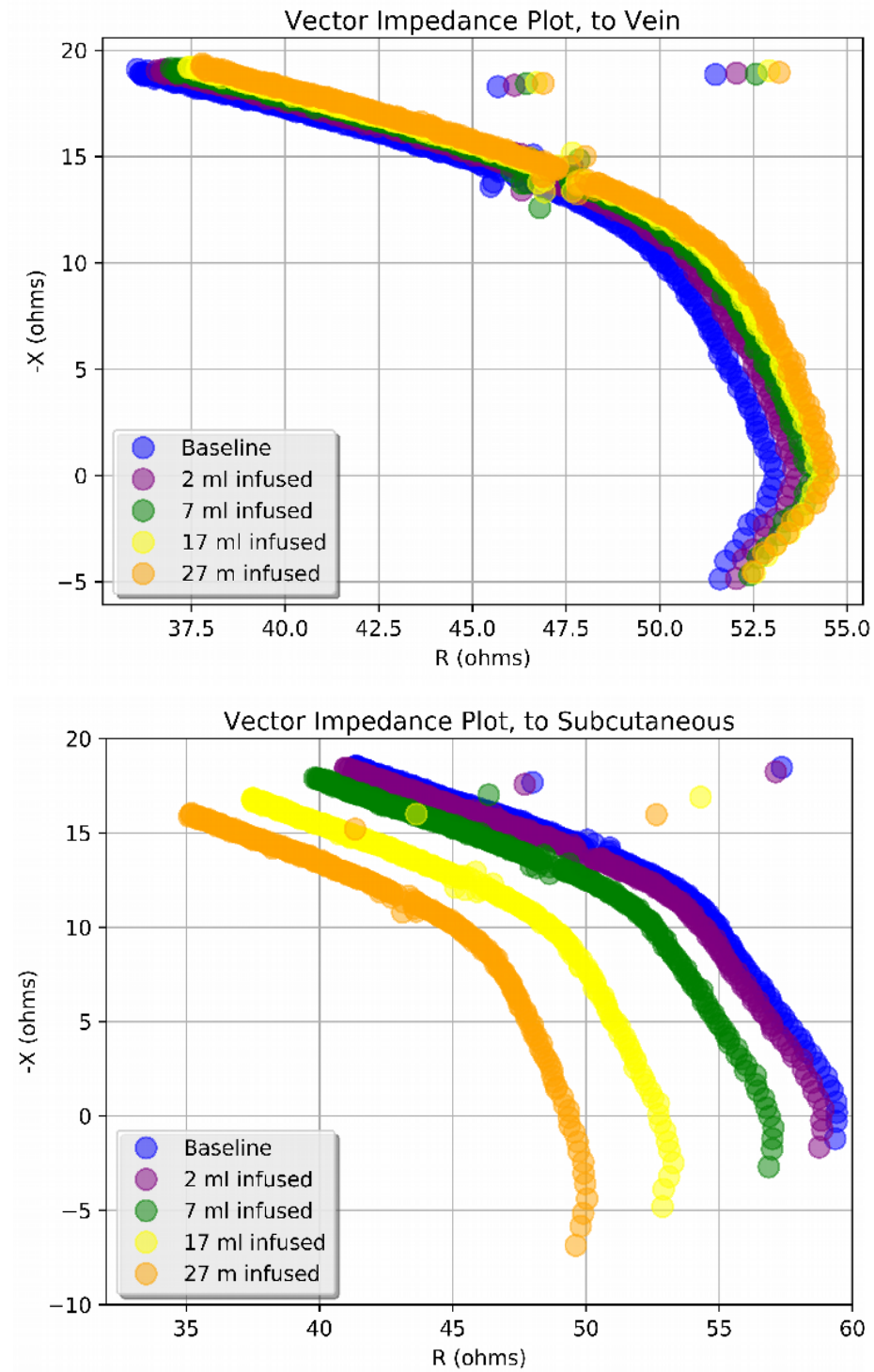


Figure 21. Localized Bioimpedance Measurement of the IV site during (top) normal drug delivery to the blood stream and (bottom) to the surrounding tissue simulating an infiltration.

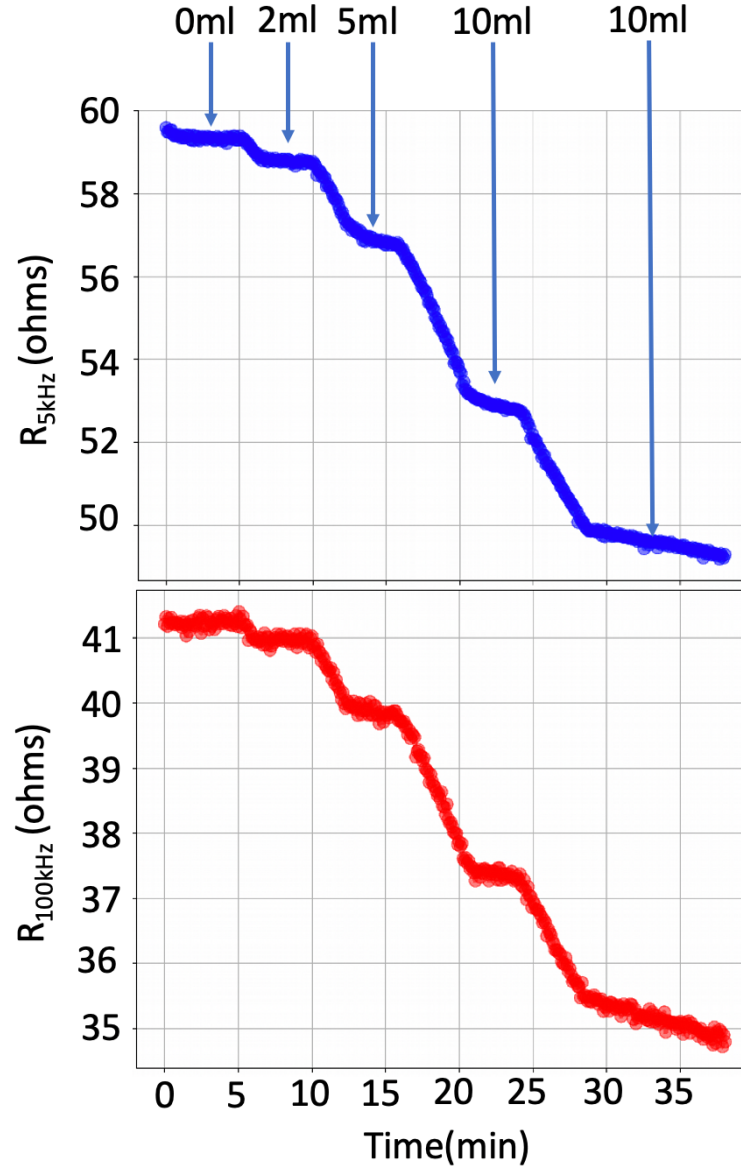


Figure 22. Localized Bioimpedance Measurement at 5 and 100 kHz of an IV site while infusing 2, 7, 17, and 27 mL of fluid.

Moreover, as illustrated earlier in Chapters 3 and 4, low frequency currents depend primarily on extracellular fluid for path due to their inability to penetrate cell walls, which is also shown here in Figure 22. After injecting a total of 27 mL of saline into the surrounding tissue, there is 10 Ω decrease in the 5 kHz bioimpedance measurement compared to 6.5 Ω drop in the 100 kHz bioimpedance measurement.

5.3 Human Subject Study at Children’s Healthcare of Atlanta

In Section 5.2, a controlled experiment was performed to validate the system’s ability to detect IV infiltration in a controlled setting is presented. In this section, we describe the use of our system in a human subject study in a clinical setting, where we develop a novel algorithm to remove the variability of the data due to subject movement.

5.3.1 Study Protocol

Approval from the Institutional Review Boards of Emory University, Children’s Healthcare of Atlanta (CHOA), and Georgia Tech was obtained, and all participants’ families provided written consent and patient assent when appropriate prior to starting any study procedures. A total of 9 pediatric patients at CHOA in the Cardiac Intensive Care Unit (CICU) participated in the study, with demographics as follows, mean (standard deviation): 9 years (7 years), 30 kg (24 kg), and 2 males. Participants receiving continuous IV therapy for at least 7 hours were recruited, and the system was placed around the IV catheter insertion site; two electrodes for the BIS were proximal and two electrodes were distal to the catheter. The electrodes were always placed such that the current stimulation electrodes were on the outside (further from the insertion site) of voltage sensing electrodes. Each temperature sensor was co-located with an IMU, and one such sensor pair was placed proximally while the second pair was placed distally to the insertion site. Recordings were obtained for a total of 6-8 hours for each patient, with the bedside nurse checking the site every hour to ensure that no infiltration had occurred, and filling out a case report form (CRF) for each participant accordingly. As none of the patients in this study had IV infiltration events, the expected result based on our prior pre-clinical studies

was that the BIS measurements should remain stable and minimally variable throughout the 6-hour recording period.

5.3.2 Baseline reset algorithm

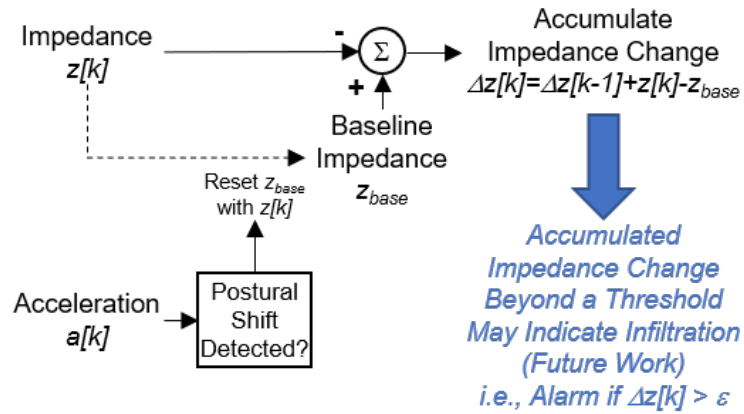


Figure 23. Block diagram of signal processing approach to removing postural shift related artifacts from impedance measurements that will ultimately provide detection of IV infiltration

The IMU data is first digitally filtered (Savitzky-Golay filter) to reduce out-of-band noise. Then, periods of elevated motion are detected from the acceleration signals of the IMU by setting an adaptive threshold of 0.2 g ($\sim 2 \text{ ms}^{-2}$). At each such period of elevated motion, the BIS data baseline is reset such that only relative changes in the impedance are retained. From Figure 23, when a change in posture is detected in the 3-axis accelerometer data from both IMUs, the bioimpedance data at this new position is set to be the baseline. If the posture is the same for the next measurement, then the change in bioimpedance between this measurement and the baseline is added to the corrected bioimpedance array; else the baseline is set to this bioimpedance measurement. This way, changes due to movement are disregarded, reducing the variability in the signal due to movement.

5.3.3 Results

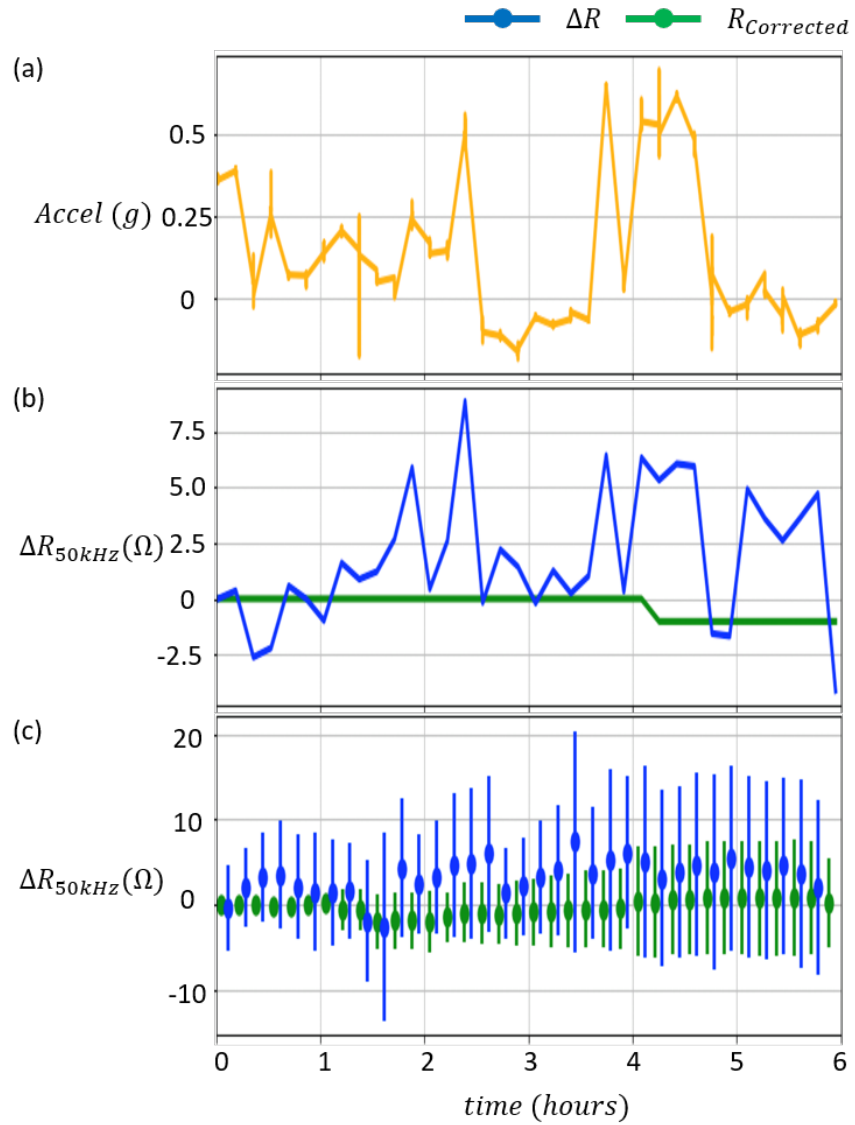


Figure 24. (a) Z-axis acceleration data from the IV site of a subject receiving IV treatment and (b) the respective raw 50 kHz resistance measured (blue) showing correlation between both signals, and the corrected signal in green. (c) The compiled mean and standard deviation of the raw 50 kHz resistance from all subjects shown in blue and the corrected signal in green showing a reduction in the variation in the signal over time.

5.3.3.1 Example Recordings from One Subject

Example recordings of the z-axis (perpendicular to the body) acceleration and 50 kHz resistance from the IV site of one subject is presented in Figure 24 (a) and (b), showing a correlation between them. This is due to the sensitivity of bioimpedance to changes in the tissue structure and content which is affected by changes in posture and movement. In the presented case, there is drop in the bioimpedance signal of 5 Ω in 10 minutes which can be confused for an infiltration possibly raising a false alarm. However, when applying our baseline resetting algorithm, we successfully removed these changes in bioimpedance due to patient movement as shown in green in Figure 24 (b).

5.3.3.2 Signal Quality

For each subject, the bioimpedance spectroscopy data of their IV site is inspected by checking the resistance vs reactance curve at various data points to make sure it follows a Fricke-Morse impedance curve. Then, the longitudinal bioimpedance data at 5, 50 and 100 kHz is checked to make sure no abrupt changes in the impedance take place due to electrodes detaching from the skin.

5.3.3.3 Recordings from All Subjects

Figure 24 (c) shows the mean and standard deviation of the raw (blue) and corrected (green) 50 kHz resistance measurements from the IV site of 9 patients. After applying our baseline correction algorithm, the variability in BIS data was reduced by an average of 64% and up to 98% in some cases maintaining a variation in the signal to less than 10 Ω over 6 hours. The algorithm was also tested on other bioimpedance measurements between 5 kHz and 100 kHz where it yielded similar results. Using the presented algorithm can increase the accuracy of early detection of an IV infiltration by ensuring that changes in

the bioimpedance due to an increase in static fluid are utilized for detection rather than false alarms due to motion / postural shifts

5.4 Conclusion

In this chapter, an extensive validation of the systems presented in Chapter 2 was performed in the context of IV infiltration detection. A porcine model was used to test the system's ability in differentiating between normal drug delivery to the blood stream and an infiltration. Moreover, the work in this chapter demonstrated, for the first time to the best of our knowledge, successful measurement of local physiological parameters around an IV catheter insertion site with a wearable device. The unique combination of high-resolution BIS data together with motion and skin temperature allowed for a novel correction algorithm to be employed for resetting the BIS baseline in the presence of noise and increasing the robustness of the approach in clinical settings. Furthermore, the approach allowed for high quality data to be obtained from pediatric participants—the very patient group that would benefit the most from this technology. While the results thus far are early, and no infiltration events have occurred in the study population to date, the quality of the signals obtained and the ability to reduce motion-related variability in BIS measurements were important results setting the foundation for future efforts. In future work, we plan to continue collecting data for the study, and if any infiltration events occur, we will quantify the accuracy, sensitivity, and specificity with which they can be detected. Following successful demonstration that such events can be accurately detected with our technology, we plan to conduct a randomized clinical trial where caregivers use our technology to improve their ability to monitor IV catheter insertion sites, with the ultimate objective of reducing the frequency and severity of IV infiltration events that occur.

CHAPTER 6. DYNAMIC SURFACE ELECTRICAL IMPEDANCE TOMOGRAPHY FOR UNIFORM STATIC FLUID QUANTIFICATION

6.1 Introduction

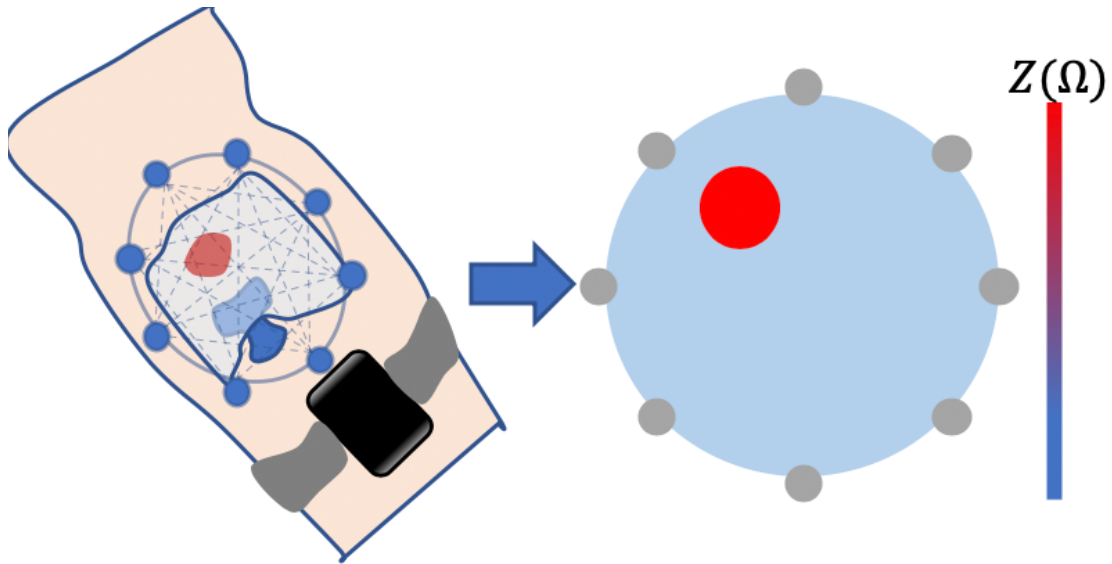


Figure 25. Surface Electrical Impedance Tomography to generate the conductivity map of the IV site showing the location of impedance changes which can be utilized to alert the medical staff if the location correlates with the IV catheter location.

Although bioimpedance is sensitive to changes in the tissue's static fluid content, its use in early detection of IV infiltration is dependent on the bioimpedance acquisition system measurement accuracy, resolution and most importantly the location of the fluid relative to the location of the measurement electrodes. Specifically, changes in static fluid volume directly in the path of the current and closer to the electrodes will be detected at a better resolution than fluids further away due to their higher impact on the current flux. This limits the use of BIA in IV infiltration detection to controlled settings where the

location of the electrodes relative to the location of the infiltrate is controlled. Moreover, to avoid exceeding the impedance threshold of the bioimpedance acquisition system current source, using larger gel electrodes is preferred due to their lower skin-electrode interface impedance. This restricts the application of bioimpedance to body areas where placing four electrodes proximally and distally to the IV site is possible, which is particularly limiting in pediatric patients where there is limited space around the IV site. Ideally, for early detection of IV infiltration in an uncontrolled wearable setting, a wearable system that is easy to place, sensitive to small changes in static fluid volumes and can locate the fluid's relative location without needing accurate system placement is desired. Such a system would allow medical professionals to make better decisions about the status of the IV treatment site.

Another major limitation of BIA is its inability to identify the location of changes in the tissue's bioimpedance, possibly confusing a change somewhere in the tissue away from the catheter as an infiltration. To mitigate that limitation, a potential solution is to use electrical impedance tomography (EIT), which is a non-invasive method that uses the tissue's segmental bioimpedance to generate a tomographic reconstruction of the tissue's conductivity distribution as shown in Figure 25 [6]. Essentially, EIT dissects the tissue impedance into areas highlighting exactly where the impedance is changing, potentially providing medical professionals a better understanding of the amount of static fluid at the IV catheter site. EIT is measured by placing a set of surface electrodes around the tissue of interest, where segments of the tissue's impedance are measured and then used by a reconstruction algorithm to generate the conductivity map of that tissue. Similar to BIA, two electrodes are used to inject and collect the tissue's excitation current, and two voltage

electrodes are used to measure the voltage drop over a certain area due to the injected current. Traditionally, EIT has been used in cross-sectional reconstruction of the tissue such as the brain, lungs and wrist, and involves using a bench top system capable of performing the impedance measurements and running the intense computations needed for the reconstruction[6].

In this chapter, a wearable system capable of accurately measuring the tissue's segmental bioimpedance and reconstructing its resistivity distribution is presented. The bioimpedance acquisition system presented in Chapter 2 is adjusted and re-calibrated using the technique in Chapter 2, and validated for accuracy, resolution and power consumption. Next, an algorithm that enables the reconstruction of the tissue's conductivity using minimal computations, and is thus amenable to a wearable setting as shown in Figure 25 is presented. The algorithm leverages the segmental impedance data from the bioimpedance acquisition system in the phantom model and animal tissue experiments (simulating IV infiltration) to validate its sensitivity and ability to detect and locate small changes in the tissue's static fluid volume. Together, the system and algorithm will assist in enabling the early detection of IV infiltration in an uncontrolled setting in future work, allowing caregivers to attend to the patient's IV site in time to avoid irreversible damage to the surrounding tissue.

6.2 Hardware Design

A wearable, embedded systems-based prototype for EIT measurement is developed. The core impedance measurement operation for our system is achieved using the AD5940 (Analog Devices, Cambridge, MA) integrated circuit (IC). The system

presented in Chapter 2 is adjusted to multiplex the current and voltage signals to measure the segmental bioimpedance of the tissue using four ADG729 (Analog Devices, MA).

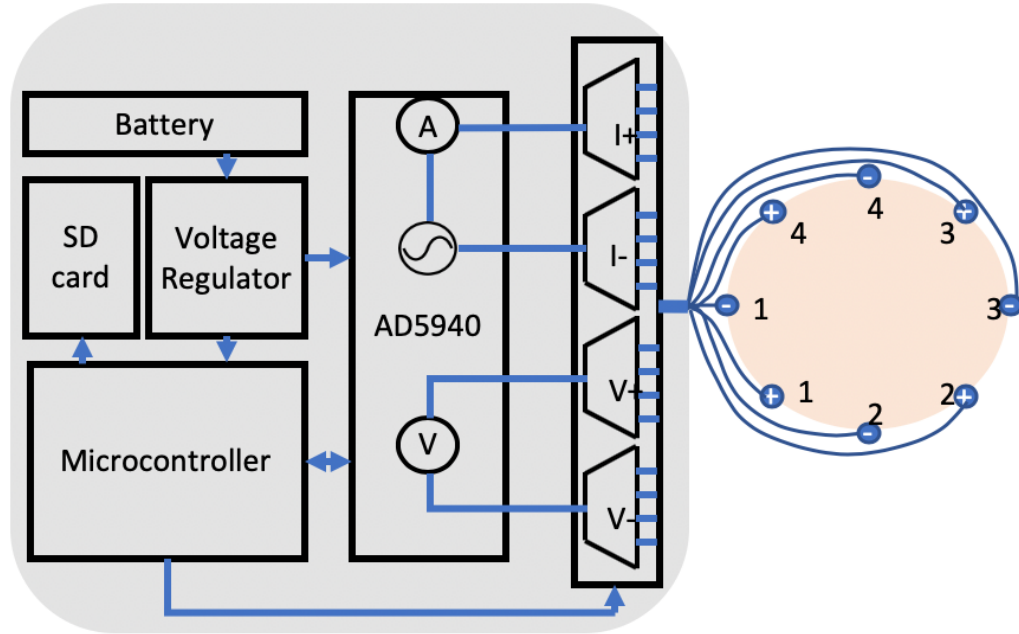


Figure 26. Electrical impedance tomography system (left) block diagram utilizing the AD5940 electro-chemical AFE to measure the segmental bioimpedance and four ADG729 analog multiplexers to specify the excitation and measurement electrodes.

Typically, to perform 8-electrode EIT, four 8x1 multiplexers connect each of the bioimpedance measurement system terminals (I+, I-, V+ and V-) to all eight electrode; however, this decreases signal-to-noise ratio (SNR) as it provides more possible signal paths thus increasing the measurement error through cross talk between the multiplexer channels. Since the AD5940 modulates the measured signal and provides its real and imaginary components rather than raw ADC measurements, we are able to distribute our eight electrodes as shown in Figure 26, by pairing the positive and negative (current and voltage) terminals separately and calculating the absolute value of the signal's real and

imaginary components. This allows us to reduce the hardware complexity and hence the measurement error of the system by limiting the sources of noise in the signal path.

6.2.1 EIT System Calibration

In the literature, the effect of the analog multiplexers used for EIT on the current and voltage signals is rarely accounted for [89]. Analog multiplexers add resistive and capacitive components (parasitic) in the signal path, hence voiding the use of the calibration coefficients retrieved without the multiplexers. Using the system in Chapter 2, we measured the calibration impedances with and without the analog multiplexers, and noticed a substantial difference in the measured raw real and imaginary values. We also tested the inter-channel variability (i.e. different channel combinations) and we noticed a small difference; hence we calibrated our system using the eight 2R1C impedances measured through the analog multiplexer channels to reduce the measurement error similar to Chapter 2.

6.3 Electrical Impedance Tomography Reconstruction Algorithm

In the literature there are numerous ways to perform EIT, but they mainly differ in two ways: (1) The electrode configuration and measurement sequence (i.e. which electrodes inject and collect the current, and measure the voltage difference), and (2) the algorithm used to perform the tomographic reconstruction of the tissue's conductivity distribution [90]. A common data collection scheme is the neighboring/adjacent method where the current is injected and collected by two adjacent electrodes and the voltage difference is measured between the remaining adjacent electrodes. This is then repeated by injecting and collecting the current by the next adjacent electrodes and the voltage

difference is measured by the remaining adjacent electrodes and so on until the current is injected and collected by all adjacent electrodes. For example, from Figure 26, the current is first injected and collected by electrodes 1- and 1+ and the voltage drop is measured between the following electrodes: 2- to 2+, 2+ to 3-, 3- to 3+, 3+ to 4- and 4- to 4+. Then the current is injected and collected by electrodes 1+ and 2-, and the voltage drop is measured by the remaining five electrodes and so on till eight different adjacent current electrodes are used to inject and collect the current; totaling in 40 or $n*(n-3)$ bioimpedance measurements where n is the number of electrodes ($n=8$, in the presented system). Using our system, we are able to collect all 40 measurements at any frequency in 464ms.

After measuring the tissue's segmental bioimpedance measurements using the presented system, a reconstruction algorithm uses this data to generate a conductivity distribution map of the measured tissue. There are hundreds of reconstruction algorithms, and as noted by Adler et al. they are usually proprietary, but they fall into two categories: iterative and linear algorithms [90]. Iterative algorithms use non-linear least squares to estimate the conductivity map from the measured impedances given a boundary problem [91]. Although accurate, they require substantial computations and electromagnetics knowledge to setup the problem boundaries. However, linear algorithms simplify the reconstruction by approximating the projections in a linear fashion similar to Computed Tomography (CT) scans, and have shown great accuracy in dynamic EIT where changes in a single area are to be detected [89, 91]. Building both algorithms requires finite element modeling (FEM) tools that are expensive, or EIT-specific tools such as EIDORS that require MATLAB and are limited to certain configurations [90]. In this section, we present a method to perform tomographic reconstruction of the tissue's conductivity distribution

using a custom linear back projection algorithm, where we employ different ways to project impedance measurements utilizing Python's cv2 (OpenCV) library to manipulate and draw objects on an image matrix.

Since this system will be used to track longitudinal changes in the static fluid content around the IV catheter, using dynamic EIT and linear back projection is possible. These methods are accurate in detecting changes at a single area of the tissue and can be readily implemented. Dynamic EIT uses the difference in the impedance measurements from a baseline to generate the dynamic changes in the conductivity distribution; in the case of IV infiltration detection, the baseline would be the segmental bioimpedances measured at the beginning of the IV therapy. The normalized impedance measurements are then projected onto a straight line starting at the center between the current electrodes to the center between the respective voltage electrodes. Our algorithm consists of two parts: first, generating the reconstruction matrix which estimates the projections for all 40 impedance measurements, and, second, using this matrix to generate the conductivity distribution. Generating the projections matrix is only done once for any electrode configuration (i.e. the location of electrodes relative to each other) and is then used by simply multiplying the matrix with the normalized impedance measurements vector.

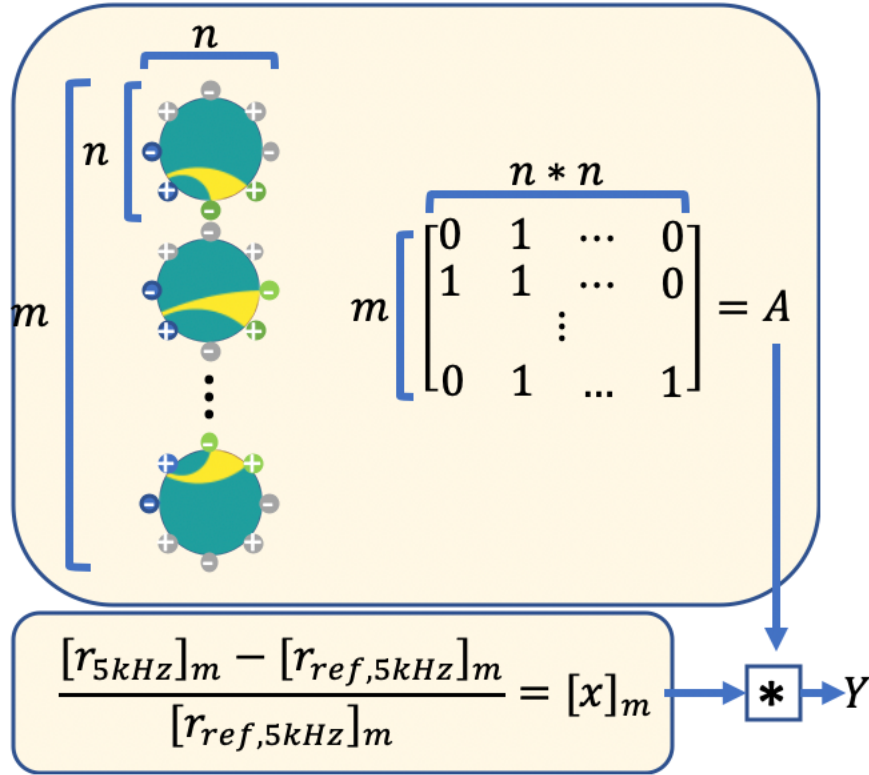


Figure 27. Dynamic Electrical Impedance Tomography Reconstruction Algorithm. Neighboring Method is used, where two adjacent electrodes are used to excite the tissue, and the voltage is measured between the remaining adjacent voltage electrodes for a total of 40 measurements for an eight-electrode system. For each measurement, a mask is created for its respective equipotential projection. All 40 masks are used to create the projection matrix which can be then used by simply multiplying it with the normalized impedance measurements vector, reducing the computational power needed for reconstruction to a single matrix multiplication. The result of the multiplication is the reconstructed image showing a scan of the underlying tissue impedance distribution.

Specifically, we start with a zero matrix (A) of dimensions 40x100x100 pixels which would serve as the base matrix for the impedance projections, then we define the relative index for the location of our electrodes in that matrix; in the presented case we used eight electrodes equally distributed around the circumference of a circle with 50-pixel radius. For our first impedance measurement with electrodes 1- and 1+ as current electrodes and electrodes 2- and 2+ as voltage electrodes, we approximated the area of the

measured bioimpedance using equipotential lines as shown in Figure 27 rather than the straight line projection shown in Figure 28b, which should provide a better estimate of the measured area. We approximate the equipotential lines by drawing two circles with their origins on the straight line passing through the current electrodes, and their circumference passing through point (p) on the straight line between the current electrodes and the respective voltage electrode. First, the gradient (m) and intercept (c) of the straight line resembling the current path between the current electrodes (e) located at row (y_e) and column (x_e) are calculated using the following equation:

$$m = \frac{y_{1+} - y_{1-}}{x_{1+} - x_{1-}} \quad (21)$$

$$c = y_{1-} - mx_{1-} \quad (22)$$

For each voltage electrode, the respective point (p) on the straight line between the current electrodes is calculated using the relative distance between the voltage electrodes and the current electrodes. In our case, since all electrodes were equally distributed around a circle, their respective points (p) are also distributed equally on the line between the current electrodes. Next, the origin (y_o, x_o) of the circle whose circumference approximates the equipotential line passing through point (p) and the voltage electrode (e) is calculated using the following equation:

$$x_o = \frac{x_p^2 - x_e^2 + y_p^2 - y_e^2 - 2c(y_p - y_e)}{2(x_p - x_e + m(y_p - y_e))} \quad (23)$$

$$y_o = mx_o + c \quad (24)$$

After calculating the location and the radius of the circle used to estimate the equipotential path between a specific voltage electrode and its respective point (p) on the line between the current electrodes, a circle is drawn using `cv2.circle` function by filling the pixels inside it with ones. To estimate the equivalent projection for the impedance measured between two voltage electrodes, the absolute difference between their respective equipotential circles is taken. This is then repeated for all 40 impedance measurements, as shown in Figure 27, to generate a $40 \times 100 \times 100$ matrix that contains the 40 projections for the impedance measurements. Once the projections matrix (A) is created, it is simply used by multiplying it with the vector (x) containing the 40 normalized segmental impedance measurements, to create a 100×100 pixel (Y) matrix representing the resistivity map of the medium measured. The matrix Y is then convolved with a Gaussian filter with dimensions 29×29 to smooth the image.

6.4 Experimental Design and Results

To validate the system and algorithm's ability to locate and quantify changes in a tissue's static fluid content, we tested its spatial accuracy and sensitivity to changes in fluid volume. In this section we present the performed experiments and results to confirm the sensitivity of our algorithm to object movement and changes in static fluid volume.

6.4.1 Phantom Model Experiments and Results

To quantify the system's spatial accuracy, we designed our experiment to have a uniform conductive medium where we place a non-conductive object at various areas of that medium. Specifically, a cylindrical container with a 23 cm diameter is filled with a half cup of saltwater which will act as the uniform conductive medium for the current to

flow, then the eight system terminals are distributed in a circular fashion, similar to the placement used in the reconstruction matrix, on the side walls of the cylinder submerged in the saltwater. The baseline measurements for the dynamic EIT reconstruction are taken with the cylinder's base covered in saltwater, then a non-conductive object with a 6.4 cm radius is moved diagonally as shown in Figure 28a. At five different positions, segmental impedance data were collected by the presented system and used to create the respective dynamic resistivity distribution of the conductive medium with a non-conductive object. Additionally, we aimed to compare our approximated equipotential impedance projections to others in the literature such as the work done by Zhang et al. where they projected the impedance measurements on a straight-line similar to CT scans from the center between current electrodes and the center between the voltage electrodes as shown in Figure 28b. We also approximated the projections to a triangle with its indices at the point (p) at the center between the current electrodes, and the two voltage electrodes as shown in Figure 28c.

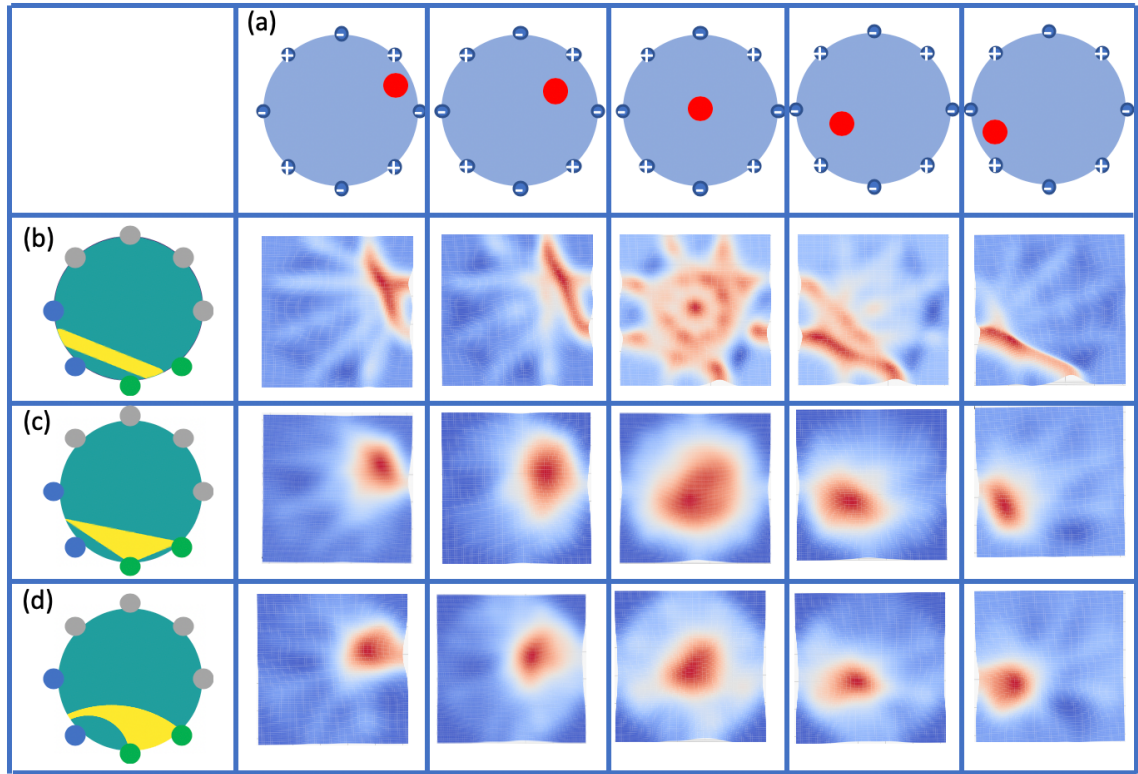


Figure 28. Phantom Model Experiment Results. (a) The eight measurement electrodes are placed around a hollow cylinder filled with saltwater. A non-conductive plastic circular object is moved diagonally to induce changes in the path of the impedance measurements close to it. Results from using (b) single line, (c) triangle and (d) area between contour lines as projections were used for comparison. Using contour lines provided the best results especially when the object is placed close to the center. This is due to its similarity to the actual equipotential paths.

When moving the object around the medium diagonally and using a straight line to project the impedance measurements as in Figure 28b, we were able to locate the objects accurately closer to the electrodes, but not around the center of the medium. However, when using a triangle to approximate the impedance projections, the error in locating the object around the center of the medium was reduced but it was still relatively large. Finally, when using our approximated equipotential projections, we were able to accurately locate the non-conductive object especially closer to the center of the medium which validates our method's ability to detect and locate the area where changes in conductivity occur.

6.4.2 Animal Tissue Experiment and Results

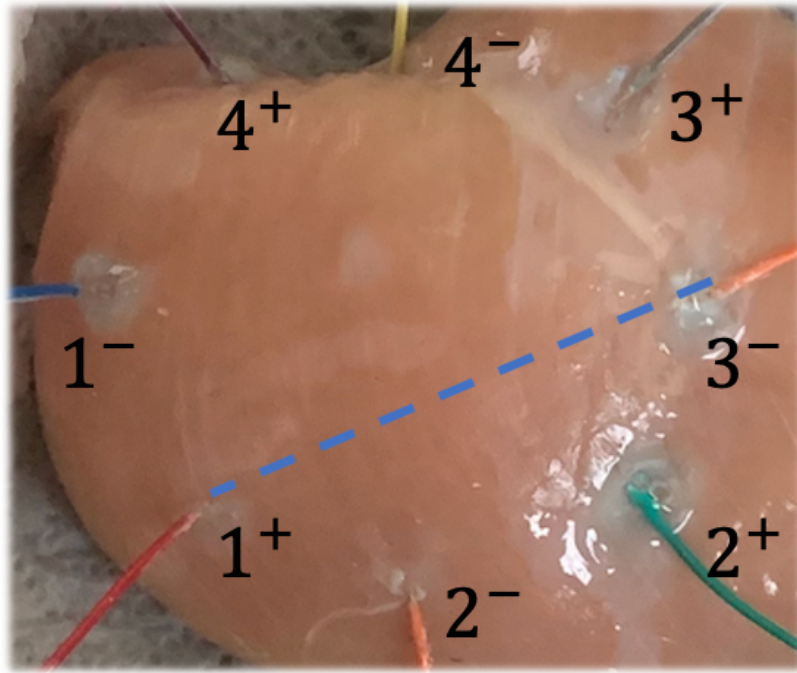


Figure 29. Animal Tissue Experiment. Eight electrodes were placed on a chicken breast in a circular fashion similar to our electrode package. The impedance measurement Z_{Across} is shown using the dotted line. Figure 30 present the experiments and results.

To quantify the system's sensitivity to changes in a tissue's static fluid volume, we used an animal tissue (chicken breast) to simulate an IV site by placing the eight system terminals in a circular fashion as shown in Figure 29. In this experiment, we aimed to study the effect of increasing the tissue's internal temperature and static fluid volume on the depth of the dynamic EIT reconstruction and compare it to traditional bioimpedance measured across the tissue between electrodes 1+ and 3-. Tissue temperature is one of the metrics used to manually check for an infiltrate and has an inverse relationship on the tissue's bioimpedance measurements (i.e. a decrease in the tissue temperature would increase its bioimpedance and vice-versa). Therefore, being able to differentiate if the

change in the impedance is due to temperature or static fluid is important for enabling the system's early detection of IV infiltration, especially in a wearable setting where the tissue is prone to temperature changes through the day. Our experimental protocol was designed accordingly by collecting the data from the chicken breast after its removal from the refrigerator at 2 degrees Celsius and leaving it to rest to room temperature (23 C).

6.4.2.1 Animal Tissue Experiment Results

While the tissue's internal temperature is rising, segmental impedance of the chicken breast along with the impedance between electrodes 1+ and 3- is measured every five minutes. For both measurements, the baseline/reference chosen to compare against was the prior measurement (5 minutes earlier). Figure 30a shows the effect of the rise in the tissue's internal temperature on the normalized impedance measured between electrodes 1+ and 3- and the dynamic EIT reconstruction. Comparing the percentage change in the impedance across the tissue to the percentage change at the lowest point in the reconstruction, we noticed a similar percentage change due to temperature. Additionally, with dynamic EIT, the impedance of the whole medium was changing at a similar rate rather than only a specific area.

Next, we simulated the effect of an IV infiltration by injecting 1.5 mL of saline solution into five different areas of the tissue. Again, after each infusion, the dynamic EIT is reconstructed using the prior measurement as a baseline and the bioimpedance measured across the tissue is also compared to the prior measurement. When using the bioimpedance measured across the tissue between electrodes 1+ and 3- we noticed a larger drop in the percentage change in bioimpedance when the liquid is infused closer to the electrodes.

Specifically, in Figure 30.b.i and iii when the fluid is injected close to electrodes 1- and 3- , the percentage drop in the measured bioimpedance due to the infused fluid was 5% and 6% respectively, compared to 4%, 3% and 2% when the fluid is injected away from the measurement electrodes. Moreover, the percentage change in the impedance measured across due to infusing 1.5ml of saline was very similar to the percentage changes in the bioimpedance due to an increase in the tissue temperature, rendering the use of traditional impedance measurements ineffective with such small changes in static fluid volumes. Alternatively, when using dynamic EIT reconstructions, we are able to detect the location of the infused fluid as shown in Figure 30b as well as easily differentiating between the change due to fluid and temperature. Comparing the depth in the tomographic reconstruction of the tissue, we observed a similar change for four of the five infusions (11% reduction in resistance at the relative fluid location), with the outlier showing a lower percentage change at the peak but a bigger area, possibly due to the fluid distributing over a larger area.

Phenom		ΔZ_{Across}	$\Delta Reconstructed\ Image$		
(a)	Chicken Breast Resting to Room Temperature	+5 min	-52 Ω ~ 7%		\updownarrow -2.5 Ω ~ 6%
		+5 min	-38 Ω ~ 5%		\updownarrow -1.6 Ω ~ 4.5%
		+5 min	-24 Ω ~ 4%		\updownarrow -1.2 Ω ~ 3.5%
		+5 min	-22 Ω ~ 3%		\updownarrow -1.0 Ω ~ 2.5%
		+5 min	-19 Ω ~ 3%		\updownarrow -0.8 Ω ~ 2.5%
(b)	Injecting 1.5 ml of Saline	(i)	-31 Ω ~ 5%		\updownarrow -5 Ω ~ 12%
		(ii)	-19 Ω ~ 4%		\updownarrow -4 Ω ~ 11%
		(iii)	-32 Ω ~ 6%		\updownarrow -4 Ω ~ 12%
		(iv)	-16 Ω ~ 3%		\updownarrow -2.5 Ω ~ 8%
		(v)	-5 Ω ~ 2%		\updownarrow -1.8 Ω ~ 11%

Figure 30. Animal Tissue Experiments and Results. (a) The effect of increase in the internal temperature of the chicken breast on the impedance across the tissue and the reconstructed image. (b) The effect of injecting 1.5 mL of saline at different sides of the chicken breast on the impedance measured across the tissue and the reconstructed. Note the substantial difference in the drop of the impedance measured across when the saline is injected close

to the electrodes (i and iii) versus when further from it (ii, iv and v) showing the effect of electrode placement on sensitivity to changes static fluid volume.

6.5 Implication on IV Infiltration Detection

For early detection of IV infiltration in a wearable uncontrolled setting, a non-invasive system capable of detecting and locating small changes in the static fluid content around the catheter insertion site is needed. In this paper, we presented a wearable system capable of performing dynamic EIT on the surface of an IV site; this system can potentially allow medical professionals to track the changes in static fluid volume at the IV catheter insertion site, enabling the early detection of IV infiltration. Our system and algorithms will help overcome some of the limitations that traditional bioimpedance has by (1) providing a uniform detection resolution to fluid across the scanned area of the tissue instead of having higher resolution closer to the electrodes, and (2) differentiating between changes due to fluid and temperature. Moreover, rather than having to accurately place four electrodes distally and proximally to the IV site, the ability to place the electrodes in a circular ring may provide easier and more consistent placement around the IV site. The system is thus well positioned for future evaluation in human subjects studies for evaluating its effectiveness in detecting IV infiltration.

6.6 Conclusion

In this chapter a simple and easy-to-implement wearable system capable of performing dynamic electrical impedance tomography system using commercially available of the shelf ICs is presented. Prior work presented in the literature uses custom built ASIC, and complicated reconstruction algorithms making them undesirable for wearable form factors. The work presented reduces hardware and computational

complexity, without sacrificing the accuracy and resolution of the reconstructed conductivity distribution. Both the system and algorithms were validated for their spatial accuracy using a phantom model, and static fluid detection resolution using animal tissue model. Future work will include incorporating the tissue kinematics and the algorithm presented in Chapter 5 to reduce motion artifacts by updating the dynamic changes in the segmental bioimpedance measurements contextualized by the IMU.

CHAPTER 7. CONCLUSION AND FUTURE WORK

7.1 Conclusion

Nowadays, with rising healthcare costs, telehealth offers a competitive alternative to traditional clinical visits, as it saves the patients travel time and costs especially in rural areas where hospitals can be tens to hundreds of miles away. Telehealth also reduces in-hospital traffic enabling physicians to better optimize their time and effort. Moreover, during this current pandemic, telehealth has become a necessity for many patient visits to avoid potential contact with asymptomatic or pre-symptomatic carriers of COVID-19. However, telehealth has been limited in its scope to simple consultations due to the lack of physical contact with the patient and minimal diagnostic tools available. At-home health monitoring offers a promising solution by providing clinically relevant metrics that would require a clinical visit to obtain. In this dissertation, we present multiple wearable technologies capable of providing clinically relevant diagnostic metrics that allow at-home health monitoring assisting the medical professionals in making better remote decisions about the wearer's health and safety.

A “wearable” medical system is, by definition, non-invasive, but it should also be minimally obtrusive in how it affects the wearer's daily routine. For example, a device can be small and easy to place, but might require the wearer to perform a specific exercise, or reduce their activity during data collection, disrupting their daily routine. Moreover, the algorithms developed to provide clinically relevant metrics from the measured signals using this device need to be within the system's computational abilities to avoid intense data transmission to the cloud and the costs that come with it. Therefore, in this

dissertation, novel, simple and accurate methods and algorithms are presented that utilize the wearer's normal activity to provide clinically relevant metrics about their tissue's static fluid content.

In this dissertation, key scientific and engineering gaps were addressed towards facilitating wearable technologies for longitudinal at-home monitoring of joint and tissue health. Specifically, we devised methods to overcome the limitations of using bioimpedance in an uncontrolled setting through pairing it with posture data to develop various algorithms for the purpose of quantifying changes in the tissue's static fluid content. First, two custom-built miniaturized bioimpedance acquisition systems with high sensitivity to localized changes in a tissue's bioimpedance, posture and temperature are presented. Both systems provide a state-of-the art bioimpedance sensing abilities that would require bulky benchtop equipment to obtain. Designing the systems with accuracy and power consumption in mind, a minimalistic design approach was applied by moving the hardware complexity to software through a novel calibration technique. Furthermore, one of the presented systems overcomes the need to use gel Ag/AgCl electrodes, making it possible to embed the device into an IV wound dressing or an ankle sock.

Using fundamentals of bioimpedance regarding the frequency dependency of the current path within the tissue, a variety of animal model, cadaver model and human subject studies were performed to understand the effect of movement and varying static fluid content on low and high bioimpedance measurements of the tissue. First, we tested this method on ankle joints for being one of the most injured parts of the body where quantifying tissue integrity and swelling are essential to understand the health of the joint and subsequently the chances of injury. Acquiring such clinical metrics would typically

require medical imaging such as MRI and X-ray which are expensive, obtrusive and most importantly do not provide the user with such information when they need it the most which is *during* activity. Our technology overcomes many of the limitations of previous work for joint health monitoring, such as the need for a baseline for normalization which is usually provided by measuring the contralateral joint, and requiring the patient to limit their movement during data collection. This is achieved by simply comparing the changes in the joint's localized bioimpedance at low and high frequencies during a step and during multiple steps.

However, not all body tissue has cyclical repetitive movement and bony structures as joints do. For body tissue with random postural shift and complex composition, an algorithm that removes the effect of these movements on the longitudinal change in the tissue's bioimpedance is developed. This allows for longitudinal tracking of the changes in the tissue's bioimpedance due to factors other than movement which correlates to the static fluid content of the tissue. Furthermore, for applications that require locating small changes in static fluid content in the tissue, a wearable dynamic electrical impedance tomography system is developed. This is achieved by a simple and accurate reconstruction algorithm that can generate the tissue's conductivity distribution by a matrix multiplication instead of performing computationally intensive non-linear squares fitting.

7.2 Future Work

7.2.1 Hardware Directions

While the devices presented in this work were miniaturized enough to be worn for a long period of time, placing them required some knowledge about bioimpedance analysis

and how electrodes should be aligned. This is mainly due to the AD5933-based system requiring Ag/AgCl electrodes to interface with the body. In contrast, the AD5940-based design system is capable of sustaining smaller electrodes with higher skin-electrode interface impedance due to its novel measurement technique. Recently, we have collaborated with Aline Eid from ATHENA lab at Georgia Tech to use their flexible screen-printed electrodes with the AD5940-based system. It was found that the AD5940-based system is capable of performing accurate bioimpedance measurements with dry 0.5 cm radius circular silver patches printed on flexible materials. Furthermore, when developing the algorithms presented in Chapters 3 and 4, one of the primary limitations they were designed to overcome is the need for accurate electrode placement on subjects for longitudinal assessment. This feature along with the AD5940-based design makes it possible to embed the whole system into an ankle support or a sock as exact electrode position and interface impedance are not a limiting factor anymore. Moreover, for IV infiltration detection, these electrodes can be aligned in a circular fashion surrounding the IV site integrating seamlessly with the IV securement.

7.2.2 Clinical Directions

While the simulation model and the study performed in Chapter 4 shows the presented method's ability to detect and quantify changes in ankle swelling and tissue integrity, the algorithms were never calibrated to provide exact swelling and tissue damage volume. This can be done through feedback by clinicians in a study where subjects would wear the system for a specific period of time performing activities that are detrimental to the ankle joint. This feedback would help us better calibrate our system outputs to specify the swelling and tissue damage volume. Specifically, tracking changes in static

fluid/swelling and tissue integrity longitudinally and correlating these parameters to the scores presented in chapter 4 to calibrate them. For IV Infiltration detection, the presented system and algorithms will be further validated through collecting more data from IV site at Children's Healthcare of Atlanta. With more data, the chances of collecting data from a site on the onset of an infiltration increases, and therefore allowing us to further develop our algorithms to detect, as early as possible, an IV infiltration.

REFERENCES

- [1] S. Cho and J. E. Atwood, "Peripheral edema," *The American journal of medicine*, vol. 113, no. 7, pp. 580-586, 2002.
- [2] J. Navas and M. Martinez-Maldonado, "Pathophysiology of edema in congestive heart failure," *Heart disease and stroke: a journal for primary care physicians*, vol. 2, no. 4, pp. 325-329, 1993.
- [3] L. Nescolarde, J. Yanguas, H. Lukaski, G. Rodas, and J. Rosell-Ferrer, "Localized BIA identifies structural and pathophysiological changes in soft tissue after post-traumatic injuries in soccer players," in *2014 36th Annual International Conference of the IEEE Engineering in Medicine and Biology Society*, 2014: IEEE, pp. 3743-3746.
- [4] O. Inan *et al.*, "Digitizing clinical trials," *NPJ digital medicine*, vol. 3, no. 1, pp. 1-7, 2020.
- [5] A. Coravos, S. Khozin, and K. D. Mandl, "Developing and adopting safe and effective digital biomarkers to improve patient outcomes," *NPJ digital medicine*, vol. 2, no. 1, pp. 1-5, 2019.
- [6] T. K. Bera, "Bioelectrical impedance methods for noninvasive health monitoring: a review," *Journal of medical engineering*, vol. 2014, 2014.
- [7] J. Nyboer, M. M. Kreider, and L. Hannapel, "Electrical impedance plethysmography: A physical and physiologic approach to peripheral vascular study," *Circulation*, vol. 2, no. 6, pp. 811-821, 1950.
- [8] A. F. Pacela, "Impedance pneumography—A survey of instrumentation techniques," *Medical and biological engineering*, vol. 4, no. 1, pp. 1-15, 1966.
- [9] B. Thomas, L. Ward, and B. Cornish, "Bioimpedance spectrometry in the determination of body water compartments: accuracy and clinical significance," *Applied radiation and isotopes*, vol. 49, no. 5-6, pp. 447-455, 1998.
- [10] H. Lukaski, "Evolution of bioimpedance: a circuitous journey from estimation of physiological function to assessment of body composition and a return to clinical research," *European journal of clinical nutrition*, vol. 67, no. S1, p. S2, 2013.
- [11] M. S. Mialich, J. F. Sicchieri, and A. A. J. Junior, "Analysis of body composition: a critical review of the use of bioelectrical impedance analysis," *Int J Clin Nutr*, vol. 2, no. 1, pp. 1-10, 2014.

- [12] U. G. Kyle *et al.*, "Bioelectrical impedance analysis—part I: review of principles and methods," *Clinical nutrition*, vol. 23, no. 5, pp. 1226-1243, 2004.
- [13] E. C. Hoffer, C. K. Meador, and D. C. Simpson, "Correlation of whole-body impedance with total body water volume," *Journal of applied physiology*, vol. 27, no. 4, pp. 531-534, 1969.
- [14] U. G. Kyle *et al.*, "Bioelectrical impedance analysis—part II: utilization in clinical practice," *Clinical nutrition*, vol. 23, no. 6, pp. 1430-1453, 2004.
- [15] S. Khalil, M. Mohktar, and F. Ibrahim, "The theory and fundamentals of bioimpedance analysis in clinical status monitoring and diagnosis of diseases," *Sensors*, vol. 14, no. 6, pp. 10895-10928, 2014.
- [16] M. G. O. Rikkert, P. Deurenberg, R. W. Jansen, M. A. van't Hof, and W. H. Hoefnagels, "Validation of multi-frequency bioelectrical impedance analysis in detecting changes in fluid balance of geriatric patients," *Journal of the American Geriatrics Society*, vol. 45, no. 11, pp. 1345-1351, 1997.
- [17] B. Cornish, I. Bunce, L. Ward, L. Jones, and B. Thomas, "Bioelectrical impedance for monitoring the efficacy of lymphoedema treatment programmes," *Breast cancer research and treatment*, vol. 38, no. 2, pp. 169-176, 1996.
- [18] P. Aberg, I. Nicander, J. Hansson, P. Geladi, U. Holmgren, and S. Ollmar, "Skin cancer identification using multifrequency electrical impedance—a potential screening tool," *IEEE transactions on biomedical engineering*, vol. 51, no. 12, pp. 2097-2102, 2004.
- [19] F. Gollan and R. Namon, "Continuous impedance monitoring of cerebral blood flow during extracorporeal circulation," in *Circulation*, 1964, vol. 30, no. 4 S 3: LIPPINCOTT WILLIAMS & WILKINS 227 EAST WASHINGTON SQ, PHILADELPHIA, PA 19106, pp. 86-&.
- [20] C. Pichard *et al.*, "Body composition by X-ray absorptiometry and bioelectrical impedance in chronic respiratory insufficiency patients," *Nutrition*, vol. 13, no. 11-12, pp. 952-958, 1997.
- [21] N. Chauveau, L. Hamzaoui, P. Rochaix, B. Rigaud, J. Voigt, and J. Morucci, "Ex vivo discrimination between normal and pathological tissues in human breast surgical biopsies using bioimpedance spectroscopy," *Annals of the New York Academy of Sciences*, vol. 873, no. 1, pp. 42-50, 1999.
- [22] B. H. Brown, P. Milnes, S. Abdul, and J. A. Tidy, "Detection of cervical intraepithelial neoplasia using impedance spectroscopy: a prospective study," *BJOG: An International Journal of Obstetrics & Gynaecology*, vol. 112, no. 6, pp. 802-806, 2005.

- [23] M. Thomasset, "Bioelectric properties of tissue. Impedance measurement in clinical medicine. Significance of curves obtained," *Lyon medical*, vol. 94, p. 107, 1962.
- [24] L. Nescolarde, J. Yanguas, H. Lukaski, X. Alomar, J. Rosell-Ferrer, and G. Rodas, "Localized bioimpedance to assess muscle injury," *Physiological measurement*, vol. 34, no. 2, p. 237, 2013.
- [25] S. Hersek *et al.*, "Wearable vector electrical bioimpedance system to assess knee joint health," *IEEE Transactions on Biomedical Engineering*, vol. 64, no. 10, pp. 2353-2360, 2017.
- [26] S. Hersek, H. Töreyin, and O. T. Inan, "A robust system for longitudinal knee joint edema and blood flow assessment based on vector bioimpedance measurements," *IEEE transactions on biomedical circuits and systems*, vol. 10, no. 3, pp. 545-555, 2016.
- [27] O. G. Martinsen and S. Grimnes, *Bioimpedance and bioelectricity basics*. Academic press, 2011.
- [28] H. Fricke and S. Morse, "The electric resistance and capacity of blood for frequencies between 800 and 4½ million cycles," *The Journal of general physiology*, vol. 9, no. 2, p. 153, 1925.
- [29] L. Ward, "Inter-instrument comparison of bioimpedance spectroscopic analysers," *Open Med Dev J*, vol. 1, pp. 3-10, 2009.
- [30] M. Y. Jaffrin and H. Morel, "Body fluid volumes measurements by impedance: A review of bioimpedance spectroscopy (BIS) and bioimpedance analysis (BIA) methods," *Medical engineering & physics*, vol. 30, no. 10, pp. 1257-1269, 2008.
- [31] X. Fan, Q. Zhou, Z. Liu, and F. Xie, "New derivation method and simulation of skin effect in biological tissue," *Bio-medical materials and engineering*, vol. 26, no. s1, pp. S429-S437, 2015.
- [32] J. Simpson *et al.*, "Body water compartment measurements: a comparison of bioelectrical impedance analysis with tritium and sodium bromide dilution techniques," *Clinical Nutrition*, vol. 20, no. 4, pp. 339-343, 2001.
- [33] D. Ayllon, F. Seoane, and R. Gil-Pita, "Cole equation and parameter estimation from electrical bioimpedance spectroscopy measurements-a comparative study," in *2009 Annual International Conference of the IEEE Engineering in Medicine and Biology Society*, 2009: IEEE, pp. 3779-3782.
- [34] J. J. Ackmann and M. A. Seitz, "Methods of complex impedance measurements in biologic tissue," *Critical reviews in biomedical engineering*, vol. 11, no. 4, pp. 281-311, 1984.

- [35] N. Li, H. Xu, W. Wang, Z. Zhou, G. Qiao, and D. D. Li, "A high-speed bioelectrical impedance spectroscopy system based on the digital auto-balancing bridge method," *Measurement Science and Technology*, vol. 24, no. 6, p. 065701, 2013.
- [36] D. Tsunami, J. McNames, A. Colbert, S. Pearson, and R. Hammerschlag, "Variable frequency bioimpedance instrumentation," in *Engineering in Medicine and Biology Society, 2004. IEMBS'04. 26th Annual International Conference of the IEEE*, 2004, vol. 1: IEEE, pp. 2386-2389.
- [37] Y. Yang, J. Wang, G. Yu, F. Niu, and P. He, "Design and preliminary evaluation of a portable device for the measurement of bioimpedance spectroscopy," *Physiological Measurement*, vol. 27, no. 12, p. 1293, 2006.
- [38] *Medical electrical equipment -- Part 1-11: General requirements for basic safety and essential performance -- Collateral standard: Requirements for medical electrical equipment and medical electrical systems used in the home healthcare environment*, IEC, 2015-01 2015.
- [39] P. Bogónez-Franco, L. Nescolarde, C. Gálvez-Montón, R. Bragós, and J. Rosell-Ferrer, "An implantable bioimpedance monitor using 2.45 GHz band for telemetry," *Physiological measurement*, vol. 34, no. 1, p. 1, 2012.
- [40] L. Breniuc, V. David, and C.-G. Haba, "Wearable impedance analyzer based on AD5933," in *Electrical and Power Engineering (EPE), 2014 International Conference and Exposition on*, 2014: IEEE, pp. 585-590.
- [41] C. Margo, J. Katrib, M. Nadi, and A. Rouane, "A four-electrode low frequency impedance spectroscopy measurement system using the AD5933 measurement chip," *Physiological measurement*, vol. 34, no. 4, p. 391, 2013.
- [42] F. Seoane, J. Ferreira, J. J. Sánchez, and R. Bragós, "An analog front-end enables electrical impedance spectroscopy system on-chip for biomedical applications," *Physiological measurement*, vol. 29, no. 6, p. S267, 2008.
- [43] A. A. Thulasi, D. Bhatia, P. T. Balsara, and S. Prasad, "Portable impedance measurement device for sweat based glucose detection," in *Wearable and Implantable Body Sensor Networks (BSN), 2017 IEEE 14th International Conference on*, 2017: IEEE, pp. 63-66.
- [44] A. Hafid, S. Benouar, M. Kadir-Talha, F. Abtahi, M. Attari, and F. Seoane, "Full impedance cardiography measurement device using Raspberry PI3 and system-on-chip biomedical instrumentation solutions," *IEEE journal of biomedical and health informatics*, vol. 22, no. 6, pp. 1883-1894, 2018.
- [45] P. Bogónez-Franco, A. Bayés-Genís, J. Rosell, and R. Bragós, "Performance of an implantable impedance spectroscopy monitor using ZigBee," in *Journal of Physics: Conference Series*, 2010, vol. 224, no. 1: IOP Publishing, p. 012163.

- [46] S. Mabrouk *et al.*, "Robust Longitudinal Ankle Edema Assessment Using Wearable Bioimpedance Spectroscopy," *IEEE Transactions on Biomedical Engineering*, 2019.
- [47] D. T.-P. Fong, Y. Hong, L.-K. Chan, P. S.-H. Yung, and K.-M. Chan, "A systematic review on ankle injury and ankle sprain in sports," *Sports medicine*, vol. 37, no. 1, pp. 73-94, 2007.
- [48] E. Kemler, I. van de Port, F. Backx, and C. N. van Dijk, "A systematic review on the treatment of acute ankle sprain," *Sports medicine*, vol. 41, no. 3, pp. 185-197, 2011.
- [49] M. Yeung, K.-M. Chan, C. So, and W. Yuan, "An epidemiological survey on ankle sprain," *British journal of sports medicine*, vol. 28, no. 2, pp. 112-116, 1994.
- [50] A. Anandacoomarasamy and L. Barnsley, "Long term outcomes of inversion ankle injuries," *British journal of sports medicine*, vol. 39, no. 3, pp. e14-e14, 2005.
- [51] R. M. van Rijn, A. G. Van Os, R. M. Bernsen, P. A. Luijsterburg, B. W. Koes, and S. M. Bierma-Zeinstra, "What is the clinical course of acute ankle sprains? A systematic literature review," *The American journal of medicine*, vol. 121, no. 4, pp. 324-331. e7, 2008.
- [52] S. Shah, A. C. Thomas, J. M. Noone, C. M. Blanchette, and E. A. Wikstrom, "Incidence and cost of ankle sprains in United States emergency departments," *Sports health*, vol. 8, no. 6, pp. 547-552, 2016.
- [53] B. R. Waterman, B. D. Owens, S. Davey, M. A. Zacchilli, and P. J. Belmont Jr, "The epidemiology of ankle sprains in the United States," *JBJS*, vol. 92, no. 13, pp. 2279-2284, 2010.
- [54] L. Chinn and J. Hertel, "Rehabilitation of Ankle and Foot Injuries in Athletes," *Clinics in sports medicine*, vol. 29, no. 1, pp. 157-167, 2010, doi: 10.1016/j.csm.2009.09.006.
- [55] P. C. de César, E. M. Ávila, and M. R. de Abreu, "Comparison of magnetic resonance imaging to physical examination for syndesmotic injury after lateral ankle sprain," *Foot & ankle international*, vol. 32, no. 12, pp. 1110-1114, 2011.
- [56] C. Van Dijk, L. Lim, P. Bossuyt, and R. Marti, "Physical examination is sufficient for the diagnosis of sprained ankles," *The Journal of bone and joint surgery. British volume*, vol. 78, no. 6, pp. 958-962, 1996.
- [57] M. Attia and M. F. Taher, "A wearable device for monitoring and prevention of repetitive ankle sprain," in *Engineering in Medicine and Biology Society (EMBC), 2015 37th Annual International Conference of the IEEE*, 2015: IEEE, pp. 4667-4670.

- [58] L. Nescolarde, J. Yanguas, H. Lukaski, X. Alomar, J. Rosell-Ferrer, and G. Rodas, "Effects of muscle injury severity on localized bioimpedance measurements," *Physiological Measurement*, vol. 36, no. 1, p. 27, 2015. [Online]. Available: <http://stacks.iop.org/0967-3334/36/i=1/a=27>.
- [59] S. Hersek *et al.*, "Wearable Vector Electrical Bioimpedance System to Assess Knee Joint Health," *IEEE Transactions on Biomedical Engineering*, vol. 64, no. 10, pp. 2353-2360, 2017, doi: 10.1109/TBME.2016.2641958.
- [60] B. Sanchez, J. Li, T. Geisbush, R. B. Bardia, and S. B. Rutkove, "Impedance alterations in healthy and diseased mice during electrically induced muscle contraction," *IEEE Transactions on Biomedical Engineering*, vol. 63, no. 8, pp. 1602-1612, 2016.
- [61] B. Fu and T. J. Freeborn, "Biceps tissue bioimpedance changes from isotonic exercise-induced fatigue at different intensities," *Biomedical Physics & Engineering Express*, vol. 4, no. 2, p. 025037, 2018.
- [62] M. Schweitzer, M. Van Leersum, S. Ehrlich, and K. Wapner, "Fluid in normal and abnormal ankle joints: amount and distribution as seen on MR images," *AJR. American journal of roentgenology*, vol. 162, no. 1, pp. 111-114, 1994.
- [63] I. O. Man and M. C. Morrissey, "Relationship between ankle-foot swelling and self-assessed function after ankle sprain," *Medicine and science in sports and exercise*, vol. 37, no. 3, pp. 360-363, 2005.
- [64] I. O. Man, M. C. Morrissey, and J. K. Cywinski, "Effect of neuromuscular electrical stimulation on ankle swelling in the early period after ankle sprain," *Physical therapy*, vol. 87, no. 1, pp. 53-65, 2007.
- [65] W. S. Quillen and L. H. Rouillier, "Initial management of acute ankle sprains with rapid pulsed pneumatic compression and cold," *Journal of Orthopaedic & Sports Physical Therapy*, vol. 4, no. 1, pp. 39-43, 1982.
- [66] B. Sanchez *et al.*, "Non-invasive assessment of muscle injury in healthy and dystrophic animals with electrical impedance myography," *Muscle & nerve*, vol. 56, no. 6, pp. E85-E94, 2017.
- [67] J. Nagy, C. J. DiDonato, S. Rutkove, and B. Sanchez, "Permittivity of ex vivo healthy and diseased murine skeletal muscle from 10 kHz to 1 MHz," *Scientific data*, vol. 6, no. 1, pp. 1-11, 2019.
- [68] R. Dodde, J. Bull, and A. Shih, "Bioimpedance of soft tissue under compression," *Physiological measurement*, vol. 33, no. 6, p. 1095, 2012.
- [69] R. J. King, J. A. Clamp, J. W. Hutchinson, and C. G. Moran, "Bioelectrical impedance: a new method for measuring post-traumatic swelling," *Journal of orthopaedic trauma*, vol. 21, no. 7, pp. 462-468, 2007.

- [70] G. A. Pop, L. L. Bisschops, B. Iliev, P. C. Struijk, J. G. van der Hoeven, and C. W. Hoedemaekers, "On-line blood viscosity monitoring in vivo with a central venous catheter, using electrical impedance technique," *Biosensors and bioelectronics*, vol. 41, pp. 595-601, 2013.
- [71] C. Gabriel, S. Gabriel, and y. E. Corthout, "The dielectric properties of biological tissues: I. Literature survey," *Physics in medicine & biology*, vol. 41, no. 11, p. 2231, 1996.
- [72] R. Abdelbaset, M. El Dosoky, and M. T. El-Wakad, "The effect of heart pulsatile on the measurement of artery bioimpedance," *Journal of Electrical Bioimpedance*, vol. 8, no. 1, pp. 101-106, 2019.
- [73] T. Freeborn and B. Fu, "Fatigue-induced cole electrical impedance model changes of biceps tissue bioimpedance," *Fractal and Fractional*, vol. 2, no. 4, p. 27, 2018.
- [74] T. A. Järvinen, M. Järvinen, and H. Kalimo, "Regeneration of injured skeletal muscle after the injury," *Muscles, ligaments and tendons journal*, vol. 3, no. 4, p. 337, 2013.
- [75] D. Lakens, "Calculating and reporting effect sizes to facilitate cumulative science: a practical primer for t-tests and ANOVAs," *Frontiers in psychology*, vol. 4, p. 863, 2013.
- [76] B. K. Buchanan and D. Kushner, "Plantar fasciitis," in *StatPearls [Internet]*: StatPearls Publishing, 2019.
- [77] C. Waitt, P. Waitt, and M. Pirmohamed, "Intravenous therapy," *Postgraduate Medical Journal*, vol. 80, no. 939, pp. 1-6, 2004, doi: 10.1136/pmj.2003.010421.
- [78] B. Odom, L. Lowe, and C. Yates, "Peripheral Infiltration and Extravasation Injury Methodology: A Retrospective Study," *Journal of infusion nursing: the official publication of the Infusion Nurses Society*, vol. 41, no. 4, p. 247, 2018.
- [79] R. E. Helm, J. D. Klausner, J. D. Klemperer, L. M. Flint, and E. Huang, "Accepted but unacceptable: peripheral IV catheter failure," *Journal of Infusion Nursing*, vol. 38, no. 3, pp. 189-203, 2015.
- [80] L. C. Hadaway, "IV infiltration: not just a peripheral problem," *Nursing2019*, vol. 32, no. 8, pp. 36-43, 2002.
- [81] P. E. Fox and N. Rutter, "The childhood scars of newborn intensive care," *Early human development*, vol. 51, no. 2, pp. 171-177, 1998.
- [82] R. J. Kumar, S. P. Pegg, and R. M. Kimble, "Management of extravasation injuries," *ANZ journal of surgery*, vol. 71, no. 5, pp. 285-289, 2001.

- [83] T. W. Major and T. K. Huey, "Decreasing IV Infiltrates in the Pediatric Patient-System-Based Improvement Project," *Pediatric nursing*, vol. 42, no. 1, p. 14, 2016.
- [84] S. M. Park, I. S. Jeong, K. L. Kim, K. J. Park, M. J. Jung, and S. S. Jun, "The effect of intravenous infiltration management program for hospitalized children," *Journal of pediatric nursing*, vol. 31, no. 2, pp. 172-178, 2016.
- [85] D. Doellman and S. Rineair, "The Use of Optical Detection for Continuous Monitoring of Pediatric IV Sites," *Journal of the Association for Vascular Access*, vol. 24, no. 2, pp. 44-47, 2019, doi: 10.2309/j.java.2019.002.003.
- [86] A. O. Bicen, L. L. West, L. Cesar, and O. T. Inan, "Toward non-invasive and automatic intravenous infiltration detection: evaluation of bioimpedance and skin strain in a pig model," *IEEE Journal of Translational Engineering in Health and Medicine*, vol. 6, pp. 1-7, 2018.
- [87] J. A. Jambulingam, R. McCrory, L. West, and O. T. Inan, "Non-invasive, multi-modal sensing of skin stretch and bioimpedance for detecting infiltration during intravenous therapy," in *2016 38th Annual International Conference of the IEEE Engineering in Medicine and Biology Society (EMBC)*, 2016: IEEE, pp. 4755-4758.
- [88] J. Kim, B. Shin, and G. Jeon, "Early Detection of Intravenous Infiltration Using Multi-frequency Bioelectrical Impedance Measurement System: Pilot Study," *Journal of Information and Communication Convergence Engineering*, vol. 15, no. 2, pp. 123-130, 2017.
- [89] Y. Zhang and C. Harrison, "Tomo: Wearable, low-cost electrical impedance tomography for hand gesture recognition," in *Proceedings of the 28th Annual ACM Symposium on User Interface Software & Technology*, 2015, pp. 167-173.
- [90] A. Adler *et al.*, "GREIT: a unified approach to 2D linear EIT reconstruction of lung images," *Physiological measurement*, vol. 30, no. 6, p. S35, 2009.
- [91] W. R. Lionheart, "EIT reconstruction algorithms: pitfalls, challenges and recent developments," *Physiological measurement*, vol. 25, no. 1, p. 125, 2004.